OFF-LINE PRODUCTION OF SINGLY-CHARGED, TRANSITION-METAL BEAMS AND SUBSEQUENT COLLINEAR LASER SPECTROSCOPY OF NEUTRAL, STABLE ^{55}Mn AND ^{56}Fe

By

Andrew Mark Klose

A DISSERTATION

Submitted to
Michigan State University
in partial fulfillment of the requirements
for the degree of

Chemistry - Doctor of Philosophy

2013

ABSTRACT

OFF-LINE PRODUCTION OF SINGLY-CHARGED, TRANSITION-METAL BEAMS AND SUBSEQUENT COLLINEAR LASER SPECTROSCOPY OF NEUTRAL, STABLE ^{55}Mn AND ^{56}Fe

By

Andrew Mark Klose

Collinear laser spectroscopy was performed on stable isotopes of neutral ^{56}Fe and ^{55}Mn in both the ground and excited electronic states. The experiments served as the groundwork for the planned study on the nuclear electromagnetic moments and charge radii of beta unstable Mn and Fe isotopes via laser probing methods at the National Superconducting Cyclotron Laboratory. Ion beams were generated in one of two sources; a commercial plasma ion source, which was used to generate ion beams from metallic and ionic salt charges, and an electron ionization source that produced ion beams from molecular fragmentation of sublimated organometallic compounds. The ions were accelerated to an energy of 15 keV and co-propagated with single-mode continuous-wave laser light. The ion beam was neutralized via charge-exchange reactions with a Na vapor. Multiple atomic levels in the outgoing atomic beam were populated in the charge-exchange reactions. One transition in neutral ^{56}Fe and two transitions in neutral ^{55}Mn were separately investigated via laser probing. The Fe transition was the $3d^6 4s^2\ ^5\mathrm{D}_4 \leftrightarrow 3d^6 4s4p\ ^5\mathrm{F}_5$ transition at 372 nm. The transitions investigated in Mn I were the $3d^5 4s^2\ ^6\mathrm{S}_{5/2} \leftrightarrow 3d^5 4s4p\ ^6\mathrm{P}_{7/2}$ transition from the Mn I ground state at 403 nm, and the $3d^5 4s4p\ ^8\mathrm{P}^{\mathrm{o}}_{9/2} \leftrightarrow 3d^5 4s4d\ ^8\mathrm{D}_{11/2}$ transition at 357 nm. The $^8\mathrm{P}^{\mathrm{o}}_{9/2}$ state is a long-lived metastable state that was semi-resonantly populated in the charge-exchange process. Hyperfine spectra for the transitions were recorded by measuring laser-induced fluorescence from the atoms as a function of effective laser frequency. The frequency

of the single resonance peak observed in the ^{56}Fe spectrum agreed with the accepted value. The hyperfine spectra obtained from the two transitions in ^{55}Mn I were each analyzed by simultaneously fitting all observed peaks for each transition, and the A and B hyperfine coupling constants were deduced. The respective A and B constants were determined to be -72.2(2) MHz and 2(1) MHz for the $3d^5 4s^2\ ^6\mathrm{S}_{5/2}$ ground state, and 428.9(1) MHz and 60(1) MHz for the $3d^5 4s4p\ ^6\mathrm{P}_{7/2}$ state, and were found to agree with the literature values. For the $3d^5 4s4p\ ^8\mathrm{P}^{\mathrm{o}}_{9/2}$ and $3d^5 4s4d\ ^8\mathrm{D}_{11/2}$ levels, the constants were determined to be A = 455.3(4) MHz and B = 71(6) MHz, and A = 409.4(8) MHz and B = -52(7) MHz, respectively, an order of magnitude more precise than the previously reported values, where available.

ACKNOWLEDGMENTS

First, I would thank my advisor, Paul Mantica, for his guidance and encouragement during my time as a graduate student. In addition, I need to thank Kei Minamisono, who helped me in more ways than I know. Thank you both for helping me develop the skills necessary to become a successful scientist and person. I would also like to recognize other members of the BECOLA group, namely Sophia and Anthony, who helped with this project. In addition, I would like to recognize Dave Morrissey, Georg Bollen, and Sean Liddick for serving on my guidance committee, and acknowledge funding support from the National Science Foundation Graduate Research Fellowship Program.

It was very enjoyable to be a part of the nuclear chemistry group at the NSCL. The weekly lunches, frequent dinners, and getaways to Paul's cottage were fantastic. The dynamic of the group was great, making coming to the lab something I looked forward to. Outside of the nuclear chemists, I need to thank other graduate students at the NSCL and in the chemistry department. The many nights at Crunchy's, countless softball games, and other activities were memorable and I will miss you all.

Last, but certainly not least, I would like to thank my wife and family. Mom and dad, thank you for your unending support and encouragement in my education. Kristen, thank you for your unconditional love, being my best friend, and putting up with me over the past four years. I cannot wait to start the next chapter of our journey together.

TABLE OF CONTENTS

LIST OF TABLES

LIST OF FIGURES

Chapter 1

Introduction

The hyperfine interaction, which perturbs the atomic structure due to interaction of atomic electrons with the nuclear spin, provides a means to study the nuclear electric quadrupole and magnetic dipole moments from atomic spectroscopy observables. The hyperfine interaction perturbation is small, typically < 1 part in 10^6, so that a high-precision measurement using, for example, laser spectroscopy is necessary to resolve the hyperfine interaction contribution to atomic levels.

The National Superconducting Cyclotron Laboratory (NSCL) at Michigan State University is developing a precision laser spectroscopy facility to measure hyperfine spectra (HFS) of rare isotope beams. The NSCL offers unique access to a wide range of short-lived isotopes as will be presented in Section 1.2. Laser spectroscopy measurements of rare isotopes "on-line" generally requires a stable isotope generated "off-line" for reference measurements. The focus of this work was to establish methods for reliable HFS measurements in stable isotopes, in particular for elements that usually prove difficult to produce in a cost-effective way in off-line environments.

In this chapter, the hyperfine interaction is introduced, and the application of precision laser spectroscopy methods to deduce nuclear properties of rare isotopes is given.

1.1 Atomic structure

The attractive Coulomb interaction of an atomic electron with the proton in the hydrogen atom leads to stationary quantum mechanical states. The Hamiltonian, including the electron kinetic energy and Coulomb interaction, of the hydrogen system is given as [4]

$$\mathcal{H}_{Cou} = \frac{-\hbar^2}{2m_e}\nabla^2 - \frac{e^2}{4\pi\epsilon_0 r}. \tag{1.1}$$

Here, e is the elementary charge, m_e is the electron mass, ϵ_0 is the permittivity of free space, and r is the distance between the electron and the nucleus. The stationary states of the hydrogen atom are defined by the principle quantum number, n, the orbital angular momentum quantum number, l, and the projection of l on an external quantization axis, m_l. In addition to the Coulomb interaction, the finite spin of the electron, s, interacts with the magnetic field created by the orbital motion of the electron, leading to a spin-orbit term in the Hamiltonian, $\mathcal{H}_{SO}$. In the framework of the LS-coupling scheme, the orbital angular momentum and spin couple to a total angular momentum, j, which spans $|l-s| < j < |l+s|$, leading to the so-called fine structure of the atomic system.

The Hamiltonian of many-electron atoms is more complicated, since the repulsive electron-electron interactions must be considered in addition to the kinetic energy, Coulomb and spin-orbit terms. The Hamiltonian for a Z-electron, Z-proton system can be expressed as:

$$\mathcal{H} = \sum_{i=1}^{Z}\left(\frac{-\hbar^2}{2m_e}\nabla_i^2 - \frac{Ze^2}{4\pi\epsilon_0 r_i}\right) + \sum_{i<k}^{Z}\left(\frac{e^2}{4\pi\epsilon_0|\mathbf{r_k}-\mathbf{r_i}|}\right) + \mathcal{H}_{SO}. \tag{1.2}$$

While not solved exactly, the energy eigenvalues of many-electron systems are well described by the quantum numbers n, L, S, and J, where the capital letters indicate the summed

momenta over all electrons (i.e. $J = \sum_{i=1}^{Z} j$). The total angular momentum J may be computed from LS-coupling of the total orbital angular momentum, L, and total spin, S. For given values of L and S, J can take values from $|L - S|$ to $|L + S|$.

1.1.1 Hyperfine structure

The interaction of nuclear electromagnetic moments with atomic electrons leads to small shifts (called splittings) in the atomic energy eigenvalues, called the hyperfine interaction. The degeneracy of the fine structure levels, J, is broken by the interaction, leading to the appearance of hyperfine levels, F, where $F = |J - I_N|$ to $F = |J + I_N|$ and I_N is the nuclear spin. The magnitude of the hyperfine interaction can be expressed via a multipole expansion [5, 6, 7] of the nuclear electromagnetic moments and it has been found that the electrostatic quadrupole and magnetic dipole interactions dominate [7].

1.1.2 Hyperfine electrostatic multipole expansion

The energy from the electrostatic interaction of the atomic electrons with the nucleus [6] is given as

$$E_{\text{elec}} = \sum_{n}^{Z} q_n V_{\text{elec}}(x_n, y_n, z_n), \tag{1.3}$$

where $V_{\text{elec}}(x_n, y_n, z_n)$ is the electric potential produced by the atomic electrons at the point $r_n = (x_n, y_n, z_n)$ of the nucleus with a charge q_n. The electric potential can be expanded in

a Taylor series about the origin and substituted into Eqn 1.3:

$$
\begin{aligned}
E_{\text{elec}} = & V_{0,\text{elec}} \sum_{n}^{Z} q_n \\
& + \left(\frac{\partial V}{\partial x}\right)_0 \sum_{n}^{Z} (q_n x_n) + \left(\frac{\partial V}{\partial y}\right)_0 \sum_{n}^{Z} (q_n y_n) + \left(\frac{\partial V}{\partial z}\right)_0 \sum_{n}^{Z} (q_n z_n) \\
& + \frac{1}{2}\left(\frac{\partial^2 V}{\partial x^2}\right)_0 \sum_{n}^{Z} \left(q_n x_n^2\right) + \frac{1}{2}\left(\frac{\partial^2 V}{\partial y^2}\right)_0 \sum_{n}^{Z} \left(q_n y_n^2\right) + \frac{1}{2}\left(\frac{\partial^2 V}{\partial z^2}\right)_0 \sum_{n}^{Z} \left(q_n z_n^2\right) \\
& + \left(\frac{\partial^2 V}{\partial xy}\right)_0 \sum_{n}^{Z} (q_n x_n y_n) + \left(\frac{\partial^2 V}{\partial xz}\right)_0 \sum_{n}^{Z} (q_n x_n z_n) + \left(\frac{\partial^2 V}{\partial yz}\right)_0 \sum_{n}^{Z} (q_n y_n z_n) \\
& + \dots
\end{aligned}
\tag{1.4}
$$

Here, $\left(\frac{\partial V}{\partial i}\right)_0$ is the partial derivative of V with respect to coordinate i at the nucleus.

The quantity:

$$\sum_{n}^{Z} q_n, \tag{1.5}$$

is the zeroth-order term of the multipole expansion and is called the electric monopole moment, which is a spherical distribution of charge with no angular dependence and is equal to Ze. The three terms:

$$\sum_{n}^{Z} (q_n x_n), \sum_{n}^{Z} (q_n y_n), \text{and} \sum_{n}^{Z} (q_n z_n) \tag{1.6}$$

give the electric dipole moment, while the following six terms:

$$
\begin{gathered}
\sum_{n}^{Z} \left(q_n x_n^2\right), \sum_{n}^{Z} \left(q_n y_n^2\right), \sum_{n}^{Z} \left(q_n z_n^2\right), \\
\sum_{n}^{Z} (q_n x_n y_n), \sum_{n}^{Z} (q_n x_n z_n), \text{and} \sum_{n}^{Z} (q_n y_n z_n)
\end{gathered}
\tag{1.7}
$$

represent the overall electric quadrupole moment. Higher-order moments do not contribute significantly to the hyperfine interaction [7], and are not considered here.

Spherical symmetry of the nucleus implies that electric moments have parity of $(-1)^L$, evidenced by the behavior of the nuclear wavefunction when (x_n, y_n, z_n) is inverted to $(-x_n, -y_n, -z_n)$. The L value is the order of the moment, where $L = 0$ for the monopole, $L = 1$ for the dipole, $L = 2$ for the quadrupole, and so on. The even L requirement for the Hamiltonian is manifested by a vanishing electric dipole moment as the moment has odd parity.

Nuclei that have an axially-symmetric charge distribution do, however, have an electric quadrupole moment through the terms $\sum_n^Z \left(q_n x_n^2\right), \sum_n^Z \left(q_n y_n^2\right)$ and $\sum_n^Z \left(q_n z_n^2\right)$ in Eqn 1.4. The atomic transition energy shift due to the electric quadrupole interaction is given as:

$$\Delta E_Q = \frac{1}{2}\left(\frac{\partial^2 V}{\partial x^2}\right)_0 \sum_n^Z \left(q_n x_n^2\right) + \frac{1}{2}\left(\frac{\partial^2 V}{\partial y^2}\right)_0 \sum_n^Z \left(q_n y_n^2\right) + \frac{1}{2}\left(\frac{\partial^2 V}{\partial z^2}\right)_0 \sum_n^Z \left(q_n z_n^2\right). \quad (1.8)$$

Note that Laplace's theorem gives that:

$$\left(\frac{\partial^2 V}{\partial x^2}\right)_0 + \left(\frac{\partial^2 V}{\partial y^2}\right)_0 + \left(\frac{\partial^2 V}{\partial z^2}\right)_0 = 0, \quad (1.9)$$

and an axial-symmetric nature of the charge distribution implies that:

$$\sum_n^Z \left(q_n x_n^2\right) = \sum_n^Z \left(q_n y_n^2\right). \quad (1.10)$$

Substitution of Eqns 1.9 and 1.10 into Eqn 1.8 gives

$$\begin{aligned}\Delta E_Q =& \frac{1}{2}\left(\sum_n^Z \left(q_n z_n^2\right) - \sum_n^Z \left(q_n x_n^2\right)\right)\left(\frac{\partial^2 V}{\partial z^2}\right)_0 \\ =& \frac{1}{4} Q_s \left(\frac{\partial^2 V}{\partial z^2}\right)_0,\end{aligned} \tag{1.11}$$

where Q_s is called the spectroscopic quadrupole moment of the nucleus:

$$Q_s = \sum_n^Z \left(q_n \left(3z_n^2 - r_n^2\right)\right), \tag{1.12}$$

and $\left(\frac{\partial^2 V}{\partial z^2}\right)_0$ is the electric field gradient (EFG), where the average value of the EFG is defined as

$$\left\langle \left(\frac{\partial^2 V}{\partial z^2}\right)_0 \right\rangle = \langle V_{zz} \rangle. \tag{1.13}$$

The spectroscopic quadrupole moment of the nucleus is the projection of the intrinsic quadrupole moment, Q_0, onto the laboratory axis [8, 9]. For well-deformed nuclei

$$Q_0 = Q_s \frac{(I_N + 1)(2I_N + 3)}{3\Omega^2 - I_N(I_N + 1)}, \tag{1.14}$$

where Ω is the projection of the nuclear spin along the intrinsic axis.

Replacing the sum over all nuclear charges in Eqn 1.12 by the integral of the continuous nuclear charge over the nuclear volume yields

$$Q_s = \int \rho(r) \left(3z_n^2 - r_n^2\right) d\kappa, \tag{1.15}$$

where $\rho(r)$ is the nuclear charge density. Incorporating the wavefunction of the nuclear charge distribution into the classical picture presented in Eqns 1.3-1.15 leads to the quantum mechanical representation of the perturbation of the fine structure level due to the electric quadrupole hyperfine interaction:

$$\Delta E_Q = B\frac{3}{4}\frac{C(C+1) - I_N(I_N+1)J(J+1)}{2I_N(2I_N-1)J(2J-1)}, \tag{1.16}$$

where

$$C = F(F+1) - I_N(I_N+1) - J(J+1), \tag{1.17}$$

and B is the electric quadrupole hyperfine coupling constant [6] given as,

$$B = eQ_s\langle V_{zz}\rangle. \tag{1.18}$$

1.1.3 Hyperfine magnetic multipole expansion

The general interaction of the nuclear magnetic multipoles with the atomic electrons can be expressed in terms of the nuclear vector potential [5]

$$V_{\text{mag}} = -\int \mathbf{A}\cdot\mathbf{J_e}(\mathbf{r})d\kappa, \tag{1.19}$$

where $\mathbf{A}$ is the vector potential and $\mathbf{J_e}(\mathbf{r})$ is the current density of the atomic electrons over the volume $d\kappa$. The potential vector can be expressed as

$$\mathbf{A}(\mathbf{r_n}) = \frac{\mu_0}{4\pi}\int \frac{\mathbf{J}(\mathbf{r_n})}{|\mathbf{r_n} - \mathbf{r'_n}|}d\alpha, \tag{1.20}$$

where $\mathbf{J}(\mathbf{r_n})$ is the nuclear current density over the volume $d\alpha$. For line and surface currents, $\mathbf{J}(\mathbf{r_n})d\alpha = \boldsymbol{i}d\mathbf{r'_n}$. A diagram defining the variables is presented in Figure 1.1.

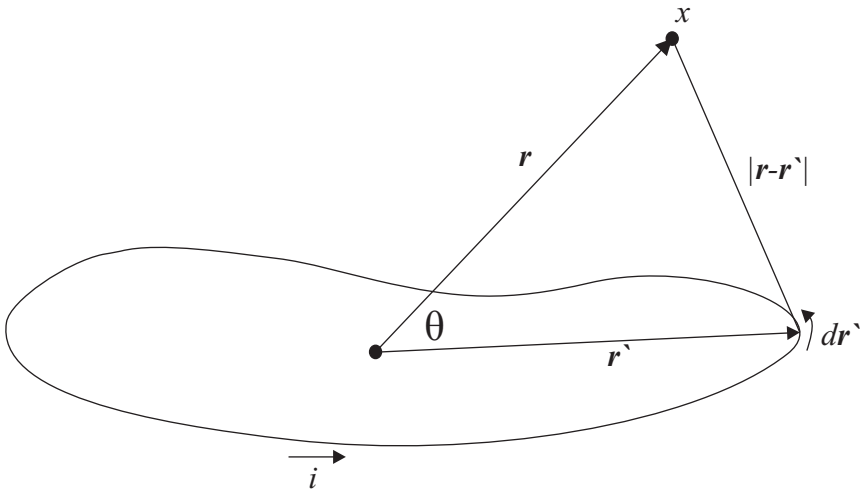

Figure 1.1: Geometric variable definition of magnetic vector multipole expansion for a current i observed at a distant point, x.

The vector potential can be written with the multipole expansion

$$\frac{1}{|\mathbf{r_n} - \mathbf{r'_n}|} = \sum_{L=0}^{\infty} \left(\frac{r_n^{L+1}{}^{L}}{r_n'^{L}} P_L(\cos\theta) \right), \tag{1.21}$$

where $P_L(\cos\theta)$ denotes the Legendre polynomial of order L. The expansion can be substituted for the potential in the expression of $\mathbf{A}(\mathbf{r_n})$ and written as:

$$\mathbf{A}(\mathbf{r_n}) = \frac{\mu_0\, i}{4\pi} \sum_{L=0}^{\infty} \frac{1}{r_n^{L+1}} \oint (r'_n)^L P_L(\cos\theta) d\mathbf{r'_n}. \tag{1.22}$$

The first three terms of the expansion are given as:

$$\begin{aligned} &= \frac{\mu_0\, i}{4\pi} \Bigg(\frac{1}{r_n} \oint d\mathbf{r'_n} + \frac{1}{r_n^2} \oint r'_n \cos\theta d\mathbf{r'_n} \\ &\quad + \frac{1}{r_n^3} \oint (r'_n)^2 \left(\frac{3}{2}\cos\theta - \frac{1}{2} \right) d\mathbf{r'_n} + \cdots \Bigg). \end{aligned} \tag{1.23}$$

The $1/r_n$ term is the magnetic monopole term, which vanishes since the vector displacement over a closed loop is zero. The $1/r_n^2$ and $1/r_n^3$ terms are the magnetic dipole and quadrupole terms, respectively. The parity of the magnetic multipole operator is $(-1)^{L+1}$, and thus even order magnetic multipoles, such as the magnetic quadrupole, vanish. In addition, odd-order magnetic multipoles above the dipole term have been found to have negligible contributions [7], and are not considered here.

The magnetic dipole contribution can be written in a more descriptive form, namely

$$\mathbf{A}_\mu = \frac{\mu_0}{4\pi}\frac{i}{r_n^2}\oint r'_n \cos\theta d\mathbf{r'_n}. \tag{1.24}$$

Noting that $r'_n \cos\theta = \frac{\mathbf{r_n}}{r_n} \cdot \mathbf{r'_n}$,

$$\mathbf{A}_\mu = \frac{\mu_0}{4\pi}\frac{i}{r_n^2}\oint \frac{\mathbf{r_n}}{r_n} \cdot \mathbf{r'_n} d\mathbf{r'_n}. \tag{1.25}$$

The integral of the current i over the area of the loop enclosed by the path $d\mathbf{r'_n}$ can be expressed as $\oint d\mathbf{r'_n} = \int d\mathbf{a}$; therefore,

$$\mathbf{A}_\mu = \frac{\mu_0}{4\pi}\frac{i}{r_n^2}\left(\frac{\mathbf{r_n}}{r_n} \times \int d\mathbf{a}\right), \tag{1.26}$$

which yields

$$\mathbf{A}_\mu = \frac{\mu_0}{4\pi}\frac{(\mathbf{r_n} \times \boldsymbol{\mu_I})}{r_n^3}, \tag{1.27}$$

where $\mu_\mathbf{I} = i\int d\mathbf{a}$ is the nuclear magnetic dipole moment.

The atomic energy shift due to the magnetic hyperfine interaction can be simplified to

$$\Delta E_\mu = -\int \frac{\mu_0}{4\pi} \frac{(\mathbf{r_n} \times \boldsymbol{\mu_I})}{r_n^3} \cdot \mathbf{J_e}(\mathbf{r}) \mathbf{d}\kappa, \tag{1.28}$$

which can be re-arranged as

$$\Delta E_\mu = -\int \frac{\mu_0}{4\pi} \frac{\boldsymbol{\mu_I}}{r_n^3} \cdot (\mathbf{r_n} \times \mathbf{J_e}(\mathbf{r})) d\kappa, \tag{1.29}$$

and expressed as

$$\Delta E_\mu = -\boldsymbol{\mu_I} \cdot \langle \mathbf{H_0} \rangle. \tag{1.30}$$

Here, $\langle \mathbf{H_0} \rangle$ represents the magnetic field produced by the atomic electrons at the nucleus. Transforming the classical argument into a quantum expression leads to

$$\Delta E_\mu = \frac{1}{2} A \left(F(F+1) - I_N(I_N+1) - J(J+1) \right), \tag{1.31}$$

where A is the nuclear magnetic dipole hyperfine coupling constant defined as,

$$A = \frac{\mu_I \langle H_0 \rangle}{\mathbf{I_N} \cdot \mathbf{J}}. \tag{1.32}$$

The change in energy for the magnetic dipole and electric quadrupole hyperfine interactions are additive. In general, the hyperfine shift due to μ_I is 1-2 orders of magnitude larger than the hyperfine shift from Q_s. It is important to note that the electrostatic and magnetic multipole expansions terminate at order $2I_N$ or $2J$, whichever is smaller [7].

1.1.4 Optical-based atomic spectroscopy

Optical-based spectroscopy has been extensively utilized to determine the energy spectra of atomic systems. Electronic transitions between a lower state, l, and an upper state u are shown in Figure 1.2. One means by which an electron may be excited from state l to state

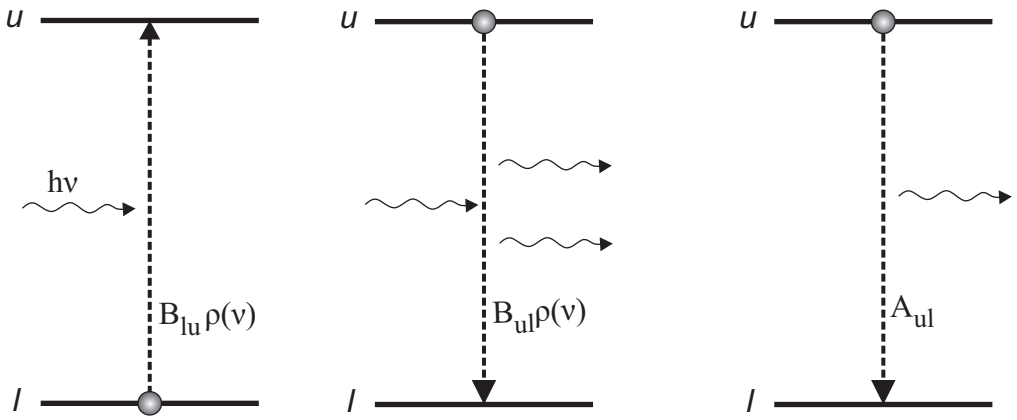

Figure 1.2: Depiction of stimulated absorption (left), stimulated emission (middle), and spontaneous decay (right) of an atomic electron.

u is by absorbing a photon from an applied optical radiation field. The time dependent probability, $\frac{d}{dt}P_{lu}$, that a molecule will absorb a photon with energy $h\nu$ is given as

$$\frac{d}{dt}P_{lu} = B_{lu}\rho(\nu). \tag{1.33}$$

Here, B_{lu} is the probability of stimulated absorption, called the Einstein coefficient of stimulated absorption and $\rho(\nu)$ is the spectral energy density of the radiation field. The radiation field can stimulate transitions of electrons in state u to state l. The probability of this stimulated emission is

$$\frac{d}{dt}P_{ul} = B_{ul}\rho(\nu), \tag{1.34}$$

where B_{ul} is the Einstein coefficient of stimulated emission. Alternatively, the state u may spontaneous decay to state l independent of the external radiation field; the probability of the spontaneous decay is given as

$$\frac{d}{dt}P_{ul}^{\text{spon}} = A_{ul}, \tag{1.35}$$

where A_{ul} is the Einstein coefficient of spontaneous emission. The lifetime, τ_{ul} of state u due to the spontaneous decay is given as

$$\tau_{ul} = \frac{1}{A_{ul}}. \tag{1.36}$$

Considering the absorption and emission processes given in Eqns 1.33-1.35, the population distribution among the lower and upper states is given by the rate equations

$$\frac{dN_u}{dt} = B_{lu}\rho(\nu)N_l - B_{ul}\rho(\nu)N_u - A_{ul}N_u \tag{1.37}$$

and

$$\frac{dN_l}{dt} = -B_{lu}\rho(\nu)N_l + B_{ul}\rho(\nu)N_u + A_{ul}N_u, \tag{1.38}$$

where N_u and N_l are the populations of states u and l, respectively.

Many times transitions among more than two states must be considered. In this case, the time dependent population of the excited state i with transitions to j states is given as:

$$\frac{dN_i}{dt} = \sum_{k\neq i}^{j}\left(B_{ki}\rho(\nu)N_k\right) - \sum_{k\neq i}^{j}\left(B_{ik}\rho(\nu)N_i\right) - \sum_{k\neq i}^{j}\left(A_{ik}N_i\right). \tag{1.39}$$

The lifetime, τ, of the excited state whose decays branch to multiple states is defined as

$$\frac{1}{\tau} = \sum_{k \neq i}^{j} A_{ik}. \tag{1.40}$$

The finite lifetime of state u leads to a width of the decay transition, Γ_{nat}, given as

$$\Gamma_{\text{nat}} = \frac{1}{2\pi\tau}, \tag{1.41}$$

and is called the "natural linewidth". The optical transition can be treated as a damped oscillator, and the amplitude of the transition over time can be Fourier transformed, leading to a Lorentz profile of the transition intensity as a function of transition frequency [10]. The Lorentz profile is defined as

$$L(\nu) = \frac{1}{2\pi} \frac{\Gamma_{\text{nat}}}{(\nu - \nu_c)^2 + \left(\frac{\Gamma_{\text{nat}}}{2}\right)^2}. \tag{1.42}$$

Here, $L(\nu)$ is the intensity of the Lorentzian profile centered at frequency ν_c.

A schematic of the allowed hyperfine transitions [6] for a $J = 2 \rightarrow J = 3$ fine structure transition with $I_N = 1$ is presented in Figure 1.3. The frequency of the fine structure transition is referred to as the center-of-gravity frequency, ν_{cg}, for the hyperfine structure (HFS). It is important to note that the hyperfine interaction is a small perturbation on the overall atomic excitation. Typical atomic transitions have frequencies of 100s of THz, whereas the hyperfine interaction is typically 10^6 times smaller and on the order of 100s of MHz. Thus, in order to resolve the hyperfine structure, resolution of better than 1 part in

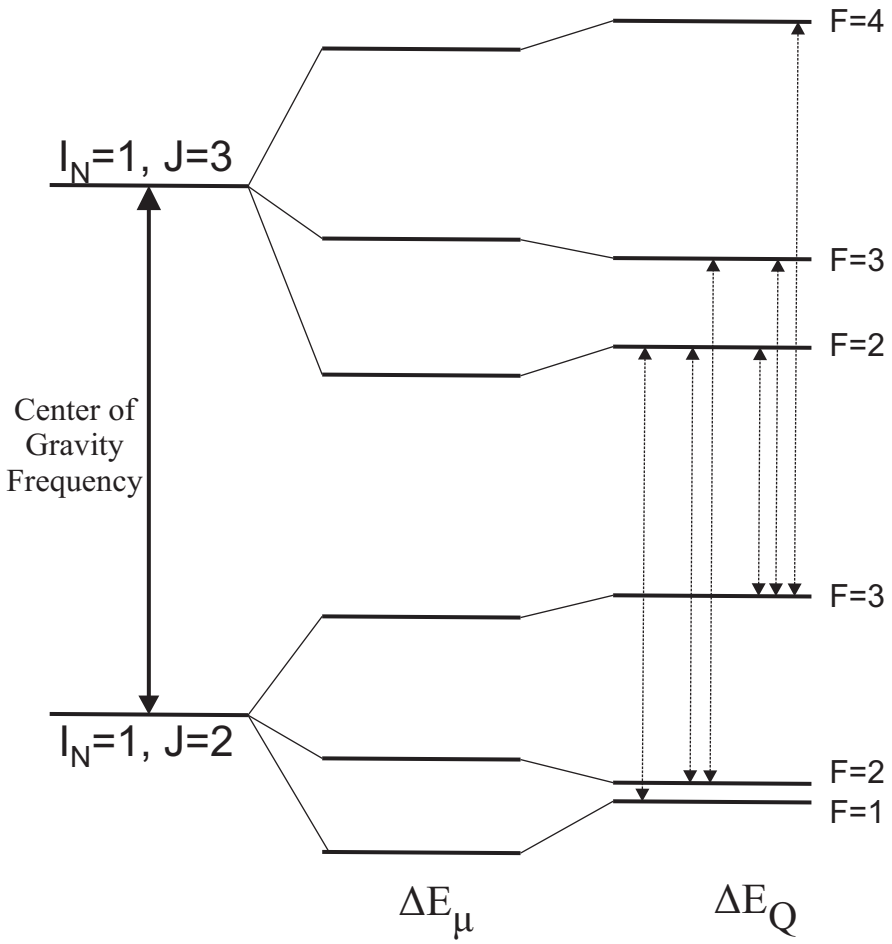

Figure 1.3: An example of allowed hyperfine transitions from a $I_N = 1, J = 2$ fine structure state to a $I_N = 1, J = 3$ state. The hyperfine splittings due to the nuclear magnetic dipole and electric quadrupole moments are indicated by the evolution of the energy of each hyperfine level. Allowed hyperfine transitions are shown as arrows.

10^6 is necessary. One means to achieve such a high precision measurement of the HFS is to employ laser light to excite the atomic transitions [10].

1.1.5 Lasers applied to atomic spectroscopy

The energy spacing between allowed electronic transitions in atomic systems is often of order 1 eV, corresponding to photon wavelengths in the ultraviolet (UV), visible (Vis), or near infrared (NIR) region of the electromagnetic spectrum. Generation of laser light in the UV/Vis/NIR regime is well-developed, and compact table-top laser systems are commercially available [11, 12]. Lasers can provide a narrow bandwidth light to selectively populate excited states in atomic systems. The laser power necessary to achieve atomic excitations may be on the order of 0.1-1 mW, assuming the interaction area of the laser light and sample is on the order of 10s of mm^2. As a reference, typical laser pointers have a power of order 5 mW with cross sectional areas of 10s of mm^2 [13].

One application of narrow-bandwidth light (line width on the order of 100 kHz) is laser-induced fluorescence spectroscopy, where laser light is used to probe an atomic system and the subsequent de-excitation photons, or fluorescence, are measured as a function of the probe laser frequency. When the laser frequency is resonant with an allowed atomic transition, the quantum mechanical system may resonantly absorb the laser radiation. The fluorescence emitted from the atom may be collected, and signal will become more intense when the laser-excitation is on resonance with an atomic transition. The excitation frequency, ν_c, can be deduced from the HFS based on the location(s) of observed resonance peak(s) when the fluorescence is measured.

1.2 Laser spectroscopy of refractory elements

Laser spectroscopic methods, including laser-induced fluorescence spectroscopy, have been employed to measure emission spectra of atomic and molecular systems since the 1960s [14], and HFS have been measured using various methods since the 1890s [15]. The application of laser-induced fluorescence to measure HFS of radioactive nuclides was developed nearly 40 years ago [16] to take advantage of the precision afforded by a narrow-bandwidth to deduce nuclear properties of rare isotopes. Many isotopic chains have been extensively investigated from neutron-deficient nuclides to very neutron-rich isotopes [17]. The range of radioactive isotopes that have been studied using laser-based methods is presented in Figure 1.4. Predicted bound isotopes are shown as white squares, estimated fast-beam production rates at the Facility for Radioactive Ion Beams (FRIB) shown in grey-scale, isotopes studied via laser spectroscopy [17] are shown in red, and stable nuclei are shown in blue.

Most laser spectroscopic studies of radioactive nuclides have been undertaken at so-called Isotope Separation On-Line- (ISOL-) type facilities. The ISOL production mechanism relies on the thermal diffusion of radioactive species from a thick production target. Rare isotopes of elements with low vapor pressures, or so-called "refractory" elements, often decay before they are released from the target and therefore are difficult to study at ISOL facilities. First row transition elements of Sc, Ti, V, Cr, Mn, Fe, Co, Ni, Cu, and Zn ($Z = 21 - 30$) are examples of relatively refractory elements. There is a general dearth of information of nuclear electromagnetic moments of the radioactive isotopes of the first row transition elements [18], and many rare isotopes of these elements are prime candidates for laser spectroscopic studies.

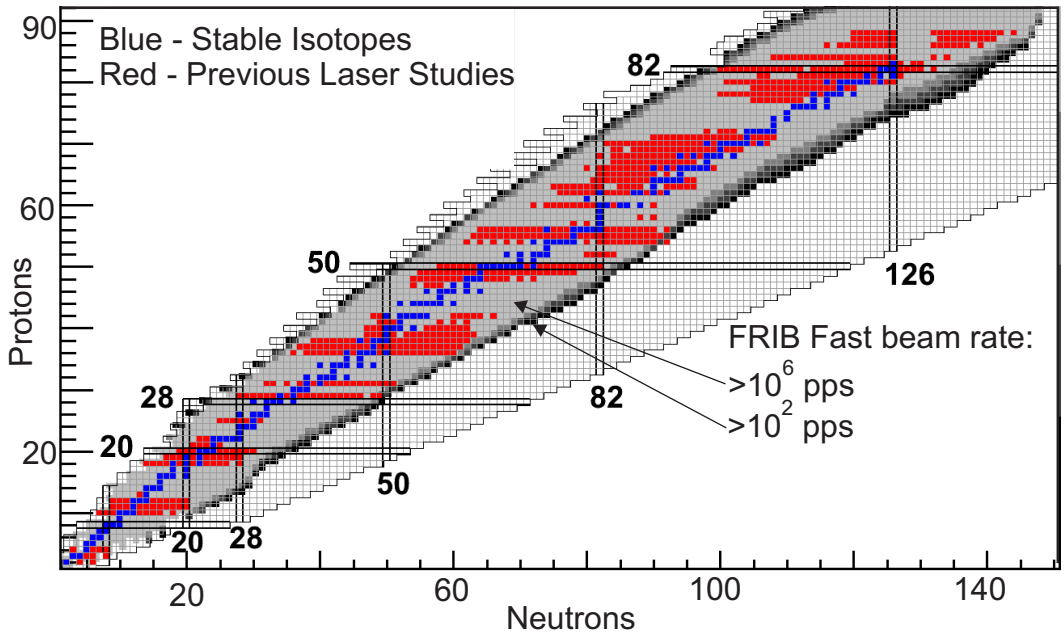

Figure 1.4: A portion of the chart of the nuclides, including isotopes of hydrogen to uranium. The grey-scale boxes indicate the estimated production rates at the FRIB fragmentation target. The lighest grey shading corresponds to rates greater than 10^6 per second and the black shading corresponds to 10^2 per second. The red boxes are isotopes that have been studied using laser spectroscopy methods. For interpretation of the references to color in this and all other figures, the reader is referred to the electronic version of this dissertation.

The BEam COoler and LAser spectroscopy facility is a new resource at NSCL, and in the future FRIB, to apply laser spectroscopy techniques to radioactive isotopes. Projectile fragmentation of heavy ion beams at relativistic velocities (100s of MeV/A) on thin production targets produces radioactive isotopes in a chemistry-independent way [19]. However, the momentum spread of the fragmentation products is not suitable for precision measurements that require an extremely small range of energy of the species of interest. Subsequent thermalization [20] of the rare isotopes and creation of good quality low-energy beams ($<$ 60 keV total kinetic energy) allow precision measurements, such as laser spectroscopy, to be performed on the isotopes.

1.2.1 Motivation for off-line ion source developments

Extraction of nuclear properties, in particular μ_I and Q_s, from the measured A and B hyperfine coupling constants relies on the calculation of the magnetic field and electric field gradient generated by the electrons at the nucleus. These atomic parameters are very sensitive to atomic electron configuration and/or correlations which are difficult to include in the interactions used in typical configuration interaction theories. Therefore, the values of $\langle H_0 \rangle$ and $\langle V_{zz} \rangle$ are extremely difficult to accurately calculate. However, the values of $\langle H_0 \rangle$ and $\langle V_{zz} \rangle$ are generally constant for isotopes of a given element [9]. Assuming $\langle H_0 \rangle$ and $\langle V_{zz} \rangle$ are constant for two isotopes, called '1' and '2', of a given element, the ratios of the A and B factors of the two isotopes can be written as:

$$\mu_{I,2} = \frac{A_2}{A_1} \frac{I_{N,2}}{I_{N,1}} \mu_{I,1}, \tag{1.43}$$

and

$$Q_{s,2} = \frac{B_2}{B_1} Q_{s,1}. \tag{1.44}$$

If the nuclear moments for isotope '1' are known, the moments of isotope '2' can be extracted by measuring the hyperfine coupling constants of both isotopes. In general, nuclear moments of stable isotopes are well known and have been measured using a variety of methods [18]. Therefore, on-line measurements of HFS of radioactive isotopes typically require interleaving off-line measurements of a corresponding stable isotope of the element being studied to determine the hyperfine coupling constant ratio of the two isotopes.

It is noted that the Bohr-Weisskopf effect [21], also called the hyperfine anomaly, can alter the magnetic dipole hyperfine coupling constant for isotopes of a given element at the level of 1% for heavy nuclei, but this effect can be neglected for the light nuclei ($Z < 30$) considered in this work.

Additional experimental requirements necessitate off-line measurements and development as well. Monitoring of the stability of the system to correct for systematic effects including uncertainties of the kinetic energy of the ion beam and the laboratory frame laser frequency. Measurement of reference isotopes is important to compare to the observables to accepted values to calibrate the experimental system.

The laser-excitation schemes used for on-line measurements must be developed off-line using stable isotopes. Therefore, the element(s) that will be studied on-line must be produced off-line ahead of the experiment to investigate the optimal probing scheme for the rare isotopes.

1.2.2 Challenges of off-line refractory ion beam production

Production of stable beams of refractory elements is challenging for similar reasons that the radioactive isotopes have not been studied at ISOL-type facilities: refractory elements have low vapor pressures. Many methods have been developed to generate ion beams of first row transition elements. Vaporization, sublimation or ablation of charge material may be used to disperse material from a solid where it may be ionized via a variety of techniques including via plasma ionization, via laser excitation(s), or via collisions with energetic electrons. The necessity of having a reliable source of stable ions of first row transition elements as references for laser spectroscopic measurements of rare isotopes at the NSCL required the implementation of such ion sources.

1.3 Organization of Dissertation

An introduction to atomic hyperfine structure was presented in this chapter, as well as available opportunities for measuring HFS of refractory element rare isotopes. In addition, the need for reference measurements during HFS measurements of radioactive isotopes was detailed, and the difficulty producing ion beams of refractory elements was discussed. A detailed description of off-line ion beam production using a plasma and electron ionization ion sources, and the technique of collinear laser spectroscopy are presented in Chapter 2. The collinear laser spectroscopy beam line of the BECOLA facility detailed in Chapter 3. Chapters 4 contains the results of development of plasma and electron ionization ion sources. The results of collinear laser spectroscopy measurements of ^{56}Fe and ^{55}Mn are given in Chapter 5. A discussion of the results is presented in Chapter 6. The final section is

Chapter 7, where a summary of the dissertation is given, and outlook of laser spectroscopy at NSCL/FRIB is presented.

Chapter 2

Experimental Techniques

Collinear laser spectroscopy (CLS) is a well-developed technique that has been used for nearly 40 years to measure hyperfine spectra (HFS) of atomic nuclei [22, 23]. CLS relies on the co-propagation of a low-energy (< 60 keV) ionic or atomic beams with laser light. Laser spectroscopic studies of radioactive isotopes on-line generally require reference measurements throughout the on-line experiment in order to calibrate beam energy and reliably deduce nuclear properties of the radioactive nuclides. Reference beams typically contain stable isotopes of the element(s) being studied. One method of providing stable isotopes is the production off-line using an ion source that is independent from the production mechanism of radioactive nuclides. There are a number of ways to vaporize, sublimate, or ablate a substrate, and then ionize atoms or molecules in the vapor. Ionization methods may include: surface ionization, laser ionization, plasma ionization, or ionization via collisions with electrons [24]. The work of this dissertation focused on plasma and electron ionization ion sources. First-row transition elements have first ionization energies of approximately 7-8 eV, and are not suitable candidates for surface ionization. On the other hand, ionization via electron bombardment or in a plasma provide potential pathways to generate singly-charged ion beams of first row transition elements. However, these ionization techniques ionize gaseous atoms and thus require a gaseous charge [24]. In this chapter, the production of stable-isotope ion beams

via plasma ionization and electron ionization are described, selection of appropriate charge material is discussed, and the CLS technique is outlined.

2.1 Production of positive ion beams via collisions with electrons

Electrostatically accelerated electrons can be used as a means to ionize atoms or molecules. Collisions of the accelerated electrons with gasous molecules can ionize the molecule. Alternatively, electrons can be used to spark a discharge that leads to a plasma formation from which positive ions may be formed. Electrons employed for ionization can be generated in various ways. The use of a hot filament provides one means to generate thermal electrons which can be electrostatically accelerated.

2.1.1 Electron generation from a filament

One method to produce electrons uses a resistively-heated filament. The Richardson-Dushman equation [25, 26] can be used to calculate the electron emission areal density I_0 (A cm^{-2}) of a filament with a given work function, ϕ (eV), can be seen to be a strong function of temperature, T (K);

$$I_0 = 120\,T^2 \times \exp\left(\text{-}11600\frac{\phi}{T}\right). \tag{2.1}$$

The fabrication of filaments is generally achieved by drawing or coating materials with high electron emissivities onto thin wires (< 0.5 mm diameter). Filament materials need to have low work functions (< 5 eV) and high melting points, typically greater than 2500 K to be useful. A canonical filament material is tungsten, which has a melting point of 3640 K and

$\phi = 4.54$ eV [27]. Consider a typical tungsten filament that is 10 cm long and has a 0.5 mm diameter. The electron emission current is defined as $I = I_0 \times A$, where $A = 19.6$ mm^2 is the surface area of the filament. A temperature of nearly 2000 K is necessary to produce 1 mA of electron emission current from this tungsten filament. Other considerations that need to be taken into account when choosing filaments include: the lifetime, operating pressure regime, and reactivity, or poisoning, of the material with molecules that may contact the filament during operation. Detailed reviews on thermionic emission and filament materials can be found in Refs. [27, 28, 29, 30].

2.1.2 Electron ionization

Thermally-generated electrons can be electrostatically accelerated to have an energy sufficient to ionize gas atoms or molecules (50-150 eV). Ionization of an atom or molecule via collisions with these electrons cannot occur until the energy transfer from the incident electron is greater than the first ionization potential of the species. Above the ionization threshold, the cross section for ionization of an atom or molecule increases to a maximum when the incident electron energy is between 3 and 4 times the first ionization potential atom or molecule [24, 31]. The ionization process has been extensively studied theoretically for low-energy incident electrons (< 200 eV) [32, 33, 34]. Although the ionization process is sometimes called electron impact ionization, within this work it will be referred to as electron ionization.

2.1.3 Plasma ionization

Ions can be efficiently generated in a plasma. A plasma can be induced by a discharge between two electrodes with a support gas. One way such a discharge can be achieved in an ion source is by resistively heating a filament to incandescence and negatively biasing the filament to a few 100 Volts relative to a nearby anode. The electrons emitted from the filament are accelerated toward the anode, and when the electron emission current is high enough, a continuous discharge of the gas can be realized, and a plasma is generated. The conditions necessary to ignite a discharge are a function of pressure, anode-cathode bias voltage, anode-cathode distance, and electron emission current, related through Paschen's Law [35];

$$V_{\mathrm{bd}} \propto \frac{A\,P\,d}{\ln(P\,d) + B}. \tag{2.2}$$

Here, V_{bd} is the breakdown voltage, or the potential difference across the anode-cathode distance d at which an electric arc between the anode and cathode will be generated in the gas at pressure P. A and B are empirical parameters dependent on the gas. The highest density of ionization in the electric arc (the plasma region) had been found to occur near the anode [24].

Typical laboratory plasma temperatures correspond to average electron energies between 1 eV and 10 eV, well below the optimum energy for electron ionization. However, thermal electrons have a Boltzmann energy distribution and electrons in the high-energy tail of the distribution will have sufficient energy to ionize neutral molecules or atoms in the gas. The overall high density of electrons in the plasma, $\sim 10^{12}$ cm^{-3} [24], makes the ionization process efficient. The physics of plasma ion sources has been described in detail in Refs. [24, 36].

2.1.4 Extraction

A positive ion beam can be extracted from an ion source by applying a positive high-voltage potential to the whole ion source relative to the beam transport line, which is typically held at ground potential. The emittance of the extracted ion beam is relatively sensitive to the electric field gradient between the high-voltage biased ion source and the ground-potential beam line. A carefully shaped extraction electrode is usually placed between the ion source and beam line to control the electric field gradient for improved ion beam extraction. After extraction, additional ion optical elements are used to transport the ions along the beam line.

2.2 Ion source charge material

Different phases and types of source material including solids, liquids, or gases in elemental or molecular form can be used as the charge for production of positive ions inside ion sources. Solid charges can come in many forms, including metals in elemental form, ionic-bonded salts, or compounds with covalent bonds. Solid charges can be sputtered and subsequently ionized inside of an ion source. Alternatively, the solid charge can be vaporized via heating and subsequently ionized [24]. Here, the use of sublimated solid charges is described.

2.2.1 Clausius-Clapeyron relation

Sublimation is the equilibrium phase change of a solid compound to its gaseous state. The temperature dependence of the phase change is characterized by the well-known Clausius-Clapeyron relation:

$$\frac{\mathrm{d}P}{\mathrm{d}T} = \frac{L(T)}{T\Delta V(T)}, \tag{2.3}$$

where, P is the saturated pressure, T is the temperature, $L(T)$ is the latent heat of the phase change, and $\Delta V(T)$ is the volume change of the system. Integrating Eqn 2.3 for a sublimation process and assuming that the molar volume of the solid is small compared to the molar volume of the gas, that the gas can be treated as an ideal gas, and that the latent heat has no temperature dependence, it is easily shown that

$$\ln P = \frac{-\Delta H_{\text{sub}}}{R}\frac{1}{T} + C, \tag{2.4}$$

where, ΔH_{sub} is the heat of sublimation, R is the ideal gas constant, and C is a constant of integration. Sublimation is endothermic, meaning ΔH_{sub} is positive. Therefore, an increase in the temperature of an equilibrium system leads to an exponential increase in the saturated vapor pressure of the compound.

2.2.2 Metal ions from charges heated in situ

The operating temperature of filament-based ion sources can reach 2000 K [30], a temperature at which the vapor pressure of some metallic elements or metal-containing salts is suitable for ion beam production ($> 10^{-2}$ Torr). On the other hand, so-called refractory elements, including most first-row transition metals, must be heated to temperatures >2000 K to achieve an appreciable vapor pressure. Heating of a solid charge can be achieved by radiative transfer of heat from a hot electron-producing filament. Alternatively, an oven can be used to heat the solid charge to the desired temperature. Once sublimated, the atoms/molecules may then be ionized. The consumption rate of charge in the source is dependent on the packing or placement of the charge as well as the operating temperature of the ion source.

2.2.3 Metal ions from volatile organometallic compounds

The production of Metal Ions from Volatile Organometallic Compounds (MIVOC) was developed in the mid-1990's [37, 38] to produce beams of refractory elements from an electron cyclotron resonance ion source. Materials with high melting points and low vapor pressures, such as refractory elements in metallic form, require an external oven to reach temperatures in excess of 2000 K, and implementation of such an oven with an ion source is difficult. The MIVOC technique provided one means to overcome the low vapor pressures of many metallic elements by employing organometallic compounds that contain a refractory metal atom bonded to organic ligands with high vapor pressures. The vapor pressure of such organometallic compounds can reach the level of 10^{-3} Torr at room temperature. Ferrocene ($Fe(C_5H_5)_2$) is an example of a volatile organometallic compound, and the molecular structure of ferrocene is presented in Figure 2.1. Ferrocene consists of an iron atom sandwiched

Figure 2.1: The molecular structure of ferrocene. The pentagons with inscribed circles represent cyclopentadienyl aromatic rings.

between two cyclopentadienyl (Cp) rings. Ferrocene has a vapor pressure of 7.5×10^{-3} Torr at 298 K [39], and a melting point of 445 K. In contrast, metallic Fe must be heated to a temperature 1525 K to achieve a vapor pressure of 10^{-3} Torr [3]. The relatively high vapor pressure and low melting points of organometallic compounds prohibit such compounds from being used directly as charges in the ion source chamber; the charge would melt and be pumped away within minutes of operation if the charge were placed directly inside the ion

source chamber. Therefore, the organometallic charge is placed in a separate vacuum chamber, a so-called MIVOC chamber, which is isolated from the ion source vacuum by a leak valve. The pressure in the MIVOC chamber reduced to a pressure near the organometallic compound vapor pressure and the organometallic vapor is introduced into the ion source chamber by opening the leak valve. The molecule is ionized inside of the source, and some fraction of the ionized products are the metal ion of interest.

The complexity of the molecular ionization/breakup means that many of the ions generated inside of the source are not the desired singly-ionized metal ions. For example, the mass spectrum of ferrocene ionized using electron ionization with 70 eV electrons is shown in Figure 2.2. The spectrum was rendered from data obtained from Ref [1]. The relative

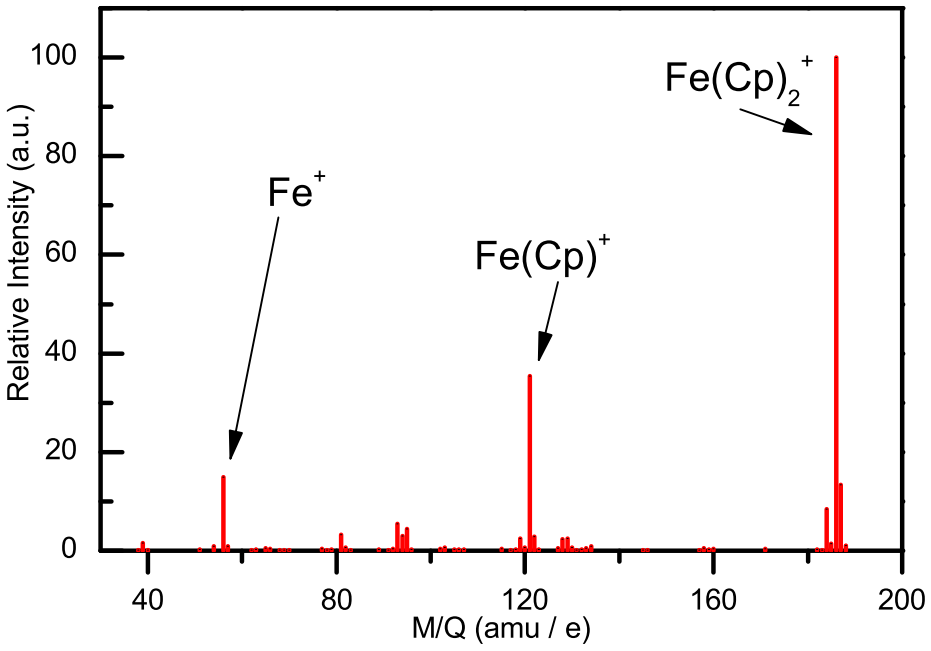

Figure 2.2: Mass spectrum of ferrocene when ionized via 70 eV electrons [1].

intensity of the $^{56}Fe^{+}$ fragment is ~5%, and other fragments, such as the molecular ions of

ferrocene, have larger relative intensities. Thus, one disadvantage of the MIVOC method is that the metal ion intensity is only a fraction of the ion source output. On the other hand, the source can be operated stably at low temperatures for long periods of time, because a large quantity of charge may be placed in the MIVOC chamber. The ion source chamber and the MIVOC chamber are also physically separated, allowing service to each chamber independently. Also, the vapor pressure of the organometallic compound can be increased by heating the charge in the MIVOC chamber, generally to temperatures less than 400 K.

2.3 Collinear laser spectroscopy

2.3.1 Basic principles

Optical spectroscopy of co-propagated laser and ion/atom beams was developed in the late 1970's [16, 22, 23] and has been used extensively to measure hyperfine spectra (HFS) of both stable and radioactive isotopes [9, 17, 40, 41, 42, 43]. A schematic of a typical CLS experiment is shown in Figure 2.3. An ion beam with kinetic energy on the order of 10s of keV kinetic energy is transported to a beam line and continuous-wave laser light is superimposed on the ion beam. Laser-induced fluorescence from the ion beam is then measured as a

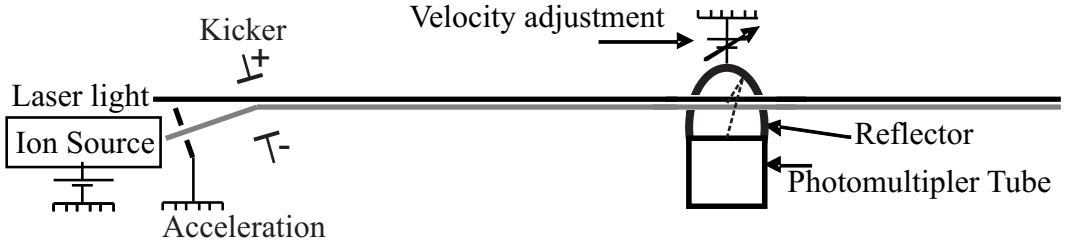

Figure 2.3: Simple schematic of a collinear laser spectroscopy experiment.

function of kinetic energy of the beam in the reflector region, which can be related to the

effective laser frequency due to the Doppler shift. The laser frequency experienced by the ion, ν, is Doppler shifted as

$$\nu = \nu_0(1 + v_z/c), \tag{2.5}$$

where ν_0 is the laser frequency in the laboratory frame of reference, v_z is the ion velocity relative to the laser propagation axis, and c is the speed of light. Substituting for the velocity of the ion,

$$v_z = c\sqrt{1 - \left(\frac{mc^2}{eU + mc^2}\right)^2}, \tag{2.6}$$

where eU is the kinetic energy of the ion beam, into Eqn. 2.5, the Doppler-shifted laser frequency experienced by the ion beam can be written as a function of kinetic energy of the ion beam:

$$\nu = \nu_0 \frac{\left(eU + mc^2\right)}{mc^2}\left(1 + \sqrt{1 - \left(\frac{mc^2}{eU + mc^2}\right)^2}\right), \tag{2.7}$$

where, e is the elementary charge and m is the mass of the ion. The laser frequency experienced by the ion can be readily scanned by altering either ν_0 or eU. Electrostatic manipulation of the kinetic energy of ions is straightforward, thus in practice the kinetic energy is altered while holding the laser frequency in the laboratory frame constant. Scanning of ν is achieved by changing eU on the order of 1 part in 10^5 by varying the electrostatic potential felt by the particle before or at the fluorescence detection region. When the ion-beam velocity is tuned such that the rest-frame frequency is in resonance with an atomic hyperfine transition, the ion beam ensemble resonantly absorbs the laser light and subsequently fluoresces. Within the interaction time between the laser and ion beams, the excitation and emission process can occur multiple times. Thus, it is advantageous to probe an atomic transition that has minimal branching probabilities to other atomic states. Note that the

fluorescence will only be measurable in a CLS experiment if the lifetime of the excited state is comparable to the fluorescence detection time window, typically of order 10^{-7} s for the velocities used in these studies.

Laser-induced fluorescence that is emitted in the light collection region, which determines the detection window, is collected by, for example, a photomultiplier tube, which converts the photons into an electronic signal. This signal is recorded for each ion-beam velocity step to generate the HFS.

2.3.2 Generating atom beams from ion-atom charge-exchange reactions

Sometimes it is useful to excite atomic transitions and not ionic transitions in an isotope. A charge-exchange cell (CEC) can be used to convert an ion beam into an atom beam via charge-exchange reactions with a suitable alkali vapor [23, 44, 45] to take advantage of well-known atomic structure for the selection of atomic transition frequencies. Alkali elements have the lowest atomic first-ionization potentials (4-5 eV) and readily give up an electron to the ion beam. The alkali vapor can be generated by heating of the solid alkali, and the ion beam is passed through the vapor. Some fraction of the ion beam is neutralized in the vapor, with the neutral fraction correlated to the alkali vapor density. Note that various atomic levels in the outgoing neutral beam can be populated in the charge-exchange reactions which can decrease the overall efficiency of the conversion to populate one particular atomic level (e.g. ground state). The velocity tuning of the atomic beam is achieved by changing the potential of the CEC relative to the ground potential (i.e. the kinetic energy of the ionic beam).

2.3.3 Line width broadening mechanisms

HFS transitions may be separated in frequency by less than 100 MHz, whereas the overall atomic excitation frequencies are typically 100's of THz. A precision measurement is necessary to resolve the atomic HFS, and such measurements are sensitive to line width broadening mechanisms. Three sources of broadening will be considered here. One particular example of line width broadening is Doppler-broadening, caused by the velocity distribution of the atom/ions being studied. The resonance frequency experienced by an atom or ion is Doppler-shifted, as presented in Eq 2.5, and velocity spread of δv_z naturally leads to a distribution in the frequency experienced by the atoms/ions:

$$\delta\nu = \frac{\nu_0}{c}\,\delta v_z. \tag{2.8}$$

The frequency distribution broadens the resonance profile and is called the Doppler width ($\Gamma_D = \delta\nu$). For example, the Doppler width of a 400 nm transition of a ^{55}Mn ensemble at 1500 K (a typical ion source temperature) is $\Gamma_D \approx 1.2$ GHz. Such a significant Doppler width will render any complex HFS to be unresolved.

Another mechanism that may increase the resonance line width is laser power broadening [46]. An optical transition is referred to as saturated if the decay rate and absorption rate are equal. The saturation laser power for linearly polarized light can be approximated [46] as

$$P_{\text{sat}} \approx \frac{2ach}{\tau\lambda^3}, \tag{2.9}$$

where a is the cross sectional area of the laser beam, c is the speed of light, h is Planck's constant, τ is the lifetime of the excited state, and λ is the wavelength of the transition.

Saturation broadens the observed linewith [46] as

$$\Gamma' = \Gamma_{\text{nat}} \times \sqrt{1 + \frac{P}{P_{\text{sat}}}}, \tag{2.10}$$

where P is the laser power used for probing the excitation, P_{sat} is the saturation laser power, Γ_{nat} is the natural line width, and Γ' is the laser-power broadened line width.

The resonance line width can also be broadened when the fluorescence measurement time, t_{tr}, is small compared to τ. The transit-time broadening is of order $\Gamma_{tr} = 1/t_{tr}$, which for the fluorescence from a 15 keV $^{55}Mn^{+}$ beam measured over a detection length of 25 mm is $\Gamma_{tr} \approx 1$ MHz.

Inelastic collisions in atomic charge-exchange reactions broaden and introduce asymmetric resonance peaks for CLS measurements of neutral species. The inelastic contribution can be quantitatively investigated in cases where sparse, well-separated inelastic channels are available [44, 45]. On the other hand, species that have a high level density necessitate a phenomenological asymmetric line shape to account for the inelastic processes. The line shapes used in this work are described below in Section 2.3.5.

2.3.4 Doppler-compression of resonance line width

One major advantage of CLS is the Doppler-compression of the resonance line width [22] as opposed to the Doppler broadening just discussed. For a CLS experiment, δv_z is determined by the energy spread, δE, of the ion beam, which can be written as:

$$\delta E = \delta(\frac{1}{2}\, m\, v_z^2) = m\, v_z\, \delta v_z. \tag{2.11}$$

Recall that the energy distribution of the beam is mostly determined by the thermal distribution in the ion source, on the order of $\delta E = 1$ eV plus generally smaller fluctuations in the accelerating potential. When the ions are extracted out of the ion source and electrostatically accelerated using a well-defined potential, δE does not change while v_z increases with eU, corresponding to a relative decrease in δv_z. This is a well-known effect in particle accelerators where the emittance of the beam decreases with acceleration. The Doppler-compressed line width of the 400 nm transition in ^{55}Mn is plotted as a function of total kinetic energy of the ^{55}Mn beam in Figure 2.4. At beam energies of more than 10 keV,

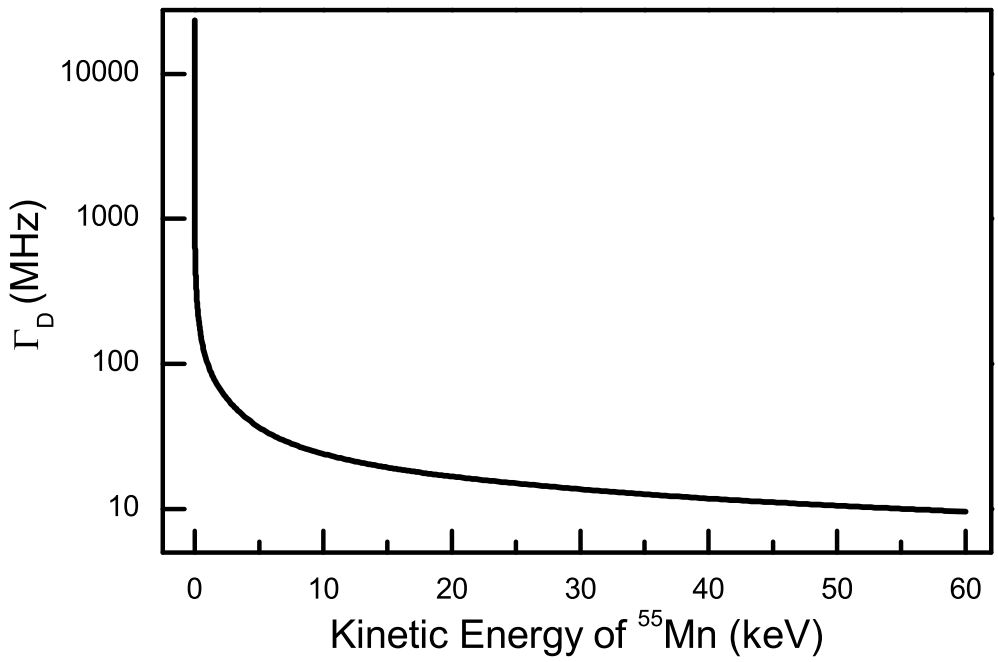

Figure 2.4: Doppler-compressed line width of a 400 nm transition in a ^{55}Mn beam as a function of kinetic energy. The ^{55}Mn beam was assumed to have an energy spread of 1 eV in this example.

the Doppler-compressed width is $\Gamma_D < 20$ MHz, which is small compared to the thermal broadening of 1.2 GHz. The inherent resolution limitation is the natural line width, which

is dependent on the lifetime of the excited state, but is generally less than 20 MHz for the prompt transitions that are probed in CLS.

2.3.5 Resonance line shapes

The line width broadening mechanisms can result in so-called Gaussian (i.e. Doppler broadening) or Lorentzian (i.e. natural line width) line shapes. The Gaussian and Lorentzian contributions to the line width are often comparable in magnitude in CLS, and a profile that can account for both line shapes is necessary. A convolution of the Gaussian and Lorentzian profiles, known as a Voigt profile [47], is routinely employed to reproduce the resonance line shapes. The Voigt profile can be obtained from the real portion of the complex error function, given as

$$V(\nu) = A\frac{2\ln(2)}{\pi^{3/2}}\frac{\Gamma_L}{\Gamma_G^2}\int_{-\infty}^{\infty}\frac{\exp[-t^2]}{\ln(2)\left(\ln(2)\frac{\Gamma_L}{\Gamma_G}\right)^2+\left(2\sqrt{\ln(2)}\frac{\nu-\nu_c}{\Gamma_G}-t\right)^2}\mathrm{d}t. \tag{2.12}$$

Here, A is amplitude, Γ_L and Γ_G are the Lorentzian and Gaussian full width at half maximum, respectively, ν_c is the centroid of the profile, and t is a dummy argument for the integration.

The Voigt profile is a computationally challenging function to compute [48, 49], and approximations of the Voigt function are often used to reduce the calculation time of χ^2 minimization routines that can fit a Voigt profile to HFS data set. One example of an approximation to the Voigt profile [50] is

$$V'(\nu) = f\,L(\nu) + (1-f)G(\nu), \tag{2.13}$$

where $L(\nu)$ and $G(\nu)$ are the Lorentzian and Gaussian profiles, respectively, and $0 \leq f \leq 1$ is the fraction of Lorentzian character. The line shape analysis presented later in Chapter 5 relied on using the full Voigt profile defined in Eqn 2.12, but consistent results were obtained using the Voigt approximation in Eqn 2.13, where f was allowed to vary.

Often it is useful to discuss a single width of the Voigt profile, Γ_V, as opposed to separate Lorentzian and Gaussian components. One approximation to estimate the Voigt width [51] is given as:

$$\Gamma_V = \frac{1}{2}\Gamma_L + \sqrt{\frac{1}{4}\Gamma_L^2 + \Gamma_D^2}. \tag{2.14}$$

Asymmetry in the resonance line shape is not contained in the simple Voigt profiles given in Eqn 2.12. Instead, it is possible to add separate profiles for each inelastic channel in the charge-exchange process [44, 45], but when more than a few channels are available, adding additional Voigt profiles to describe the overall distribution is not practical. One phenomenological approach to model the asymmetric line width is to vary both the Gaussian and Lorentzian line widths of the Voigt profile exponentially from the centroid of the profile [50] as

$$\Gamma(\nu) = \frac{2\Gamma_0}{1 + \exp[a(\nu - \nu_c)]}. \tag{2.15}$$

Here, $\Gamma(\nu)$ is the frequency dependent line width, Γ_0 is the standard width, and a is the asymmetry parameter. Equation 2.15 simplifies to $\Gamma(\nu) = \Gamma$ for a symmetric peak of $a = 0$. Gaussian, Lorentzian, Voigt, and asymmetric Voigt profiles are shown in Figure 2.5. The peaks drawn in Figure 2.5 have FWHM of 10 MHz, and the asymmetry parameter in the asymmetric Voigt profile was $a = 0.025$. The statistical goodness-of-fit of symmetric and asymmetric profiles to a particular resonance spectrum can be investigated on a case-by-case basis to determine the optimum profile to fit to the spectrum.

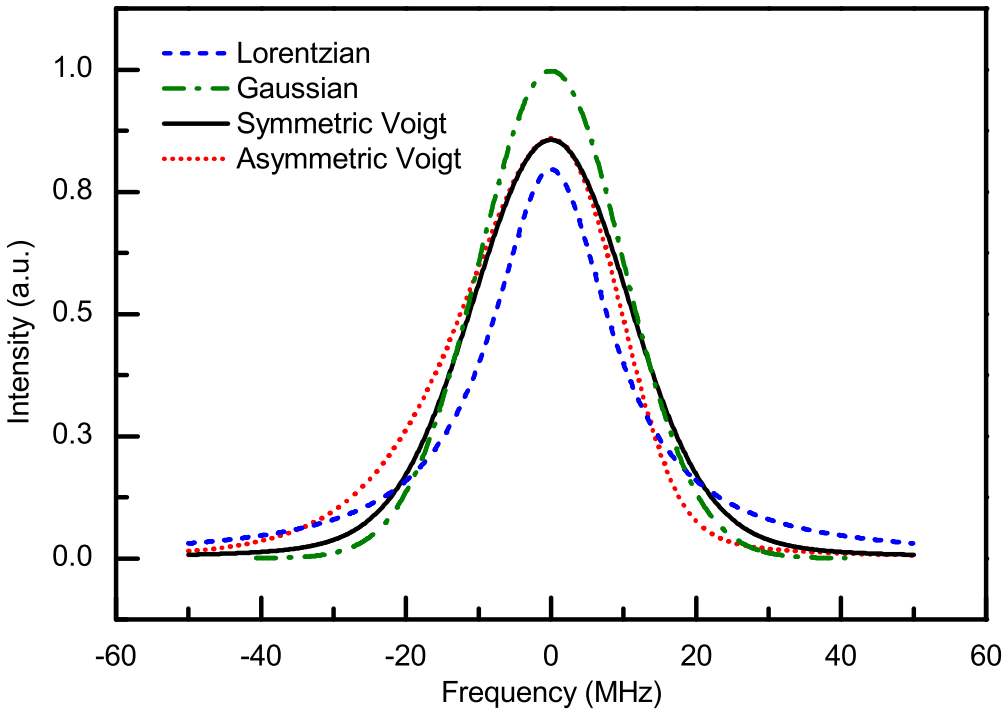

Figure 2.5: Examples of possible resonance line shapes discussed in the text. The profiles are plotted relative to the maxima of the peaks. The FWHM of all profiles was 10 MHz, and the asymmetry parameter of the asymmetric Voigt profile was $a = 0.025$.

Broadening mechanisms will generally decrease the signal height and limit the ultimate sensitivity of a CLS measurement. Therefore, it is important to minimize the factors that contribute to line shape broadening as much as possible and maximize the CLS sensitivity.

2.3.6 Expected transition intensity and hyperfine pumping

The relative intensity, I_{rel}, of a hyperfine transition from a state with quantum numbers (F, m_F, J, L, S, I_N) to an excited state $(F', m'_F, J', L', S, I_N)$ by an electric dipole transition is given by the square of the E1 matrix element of the transition [46] and is proportional to the so-called spin factor:

$$\begin{aligned} I_{\mathrm{rel}} \propto & (2J+1)(2J'+1)(2F+1)(2F'+1) \\ & \times \begin{Bmatrix} L & L' & 1 \\ J' & J & S \end{Bmatrix}^2 \begin{Bmatrix} J & J' & 1 \\ F' & F & I_N \end{Bmatrix}^2 \begin{pmatrix} F & 1 & F' \\ -m_F & q & m'_F \end{pmatrix}^2 . \end{aligned} \tag{2.16}$$

Here, q is the z-component of the excitation photon polarization; $q = 0, +1$, or -1 for linear, right-handed circular, or left-handed circular polarization of light, respectively. The two expressions in braces are Wigner 6j-symbols, and the final expression in parentheses is a Wigner 3j-symbol. Equation 2.16 is valid for a single laser excitation assuming equal distribution of the electrons among all of the m_F states.

The redistribution of electrons among hyperfine states after multiple laser excitations, or so-called hyperfine pumping, must be taken into account in a CLS measurement. After one excitation/de-excitation cycle, the population among the hyperfine states is redistributed since the electrons can decay to different F states. The redistribution can be calculated by considering all allowed transitions, and solving the coupled rate equations (e.g. Eqn 1.39)

for all states involved. The excitation $F \rightarrow F'$ and subsequent decay of F' to $F-1, F$, and $F+1$ is depicted in Figure 2.6. If the laser excitation from the maximum F state ($F_{\max}$ to

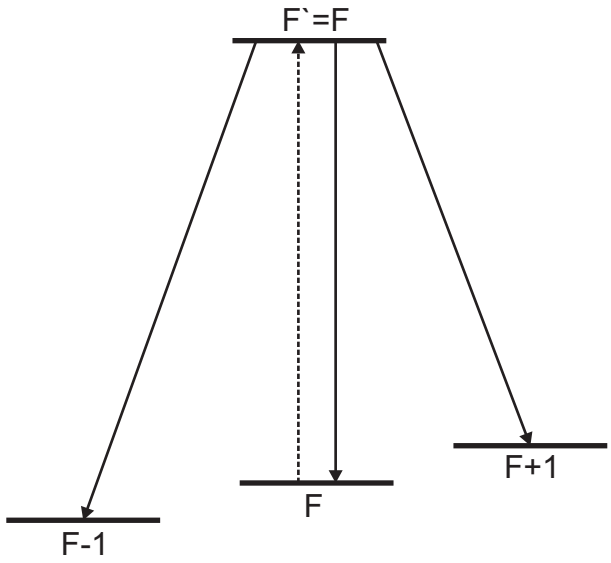

Figure 2.6: Schematic diagram of the hyperfine pumping effect. Electrons are excited from F to F' and subsequently decay to $F-1$, F, or $F+1$.

$F' = F_{\max} + 1$, the de-excitation can only decay to $F_{\max}$. Such a transition is referred to as a cyclic transition. On the other hand, the general end result of multiple excitations of a particular non-cyclic $F \rightarrow F'$ transition is the depletion of the F ground state because the decay of F' can populate the $F+1$ and $F-1$ states. Therefore, the fluorescence photons measured after multiple excitations will decrease. In addition, the probability of stimulated absorption, given in Eqn 1.33 increases linearly with an increasing radiation field. Therefore, the number of excitations, and thus the hyperfine pumping effect, increases as a function of laser power. Hyperfine pumping plays an important role when choosing the probing laser power.

Chapter 3

Experimental Setup

The implementation of a plasma ion source, an electron ionization source, and a CLS apparatus in the BEam COoler and LAser spectroscopy (BECOLA) facility are presented in this chapter. An overview of the BECOLA facility is also given, along with a detailed description of the properties and operation characteristics of the ion sources and the CLS system.

3.1 BECOLA facility layout

The BECOLA facility [52, 53] is designed to accept low-energy ($<$ 60 keV/q) rare isotope beams extracted from the NSCL beam thermalization facility [20] after in-flight production [19], or stable isotopes produced in an off-line ion source. The BECOLA facility has two major components: a cryogenic Radiofrequency Quadrupole beam cooler and buncher [54], and a CLS beam line. A schematic of the BECOLA facility configuration used in this work is shown in Figure 3.1.

Either the plasma or electron ionization source (described in Sections 3.2 and 3.3, respectively) was mounted upstream of the BECOLA facility and was placed on a high voltage potential, which defined the ion beam kinetic energy. The ion source potential was provided by a FuG Elektronik [55] model HCP 350-65 000 MOD high-voltage power supply. The FuG power supply was modified by the vendor to achieve a voltage stability of $\pm 1 \times 10^{-5}$ over 8 hours and $\pm 1 \times 10^{-5}/^{\circ}$C with a residual voltage ripple of $< 1 \times 10^{-5}$ at 60 kV. The ion source

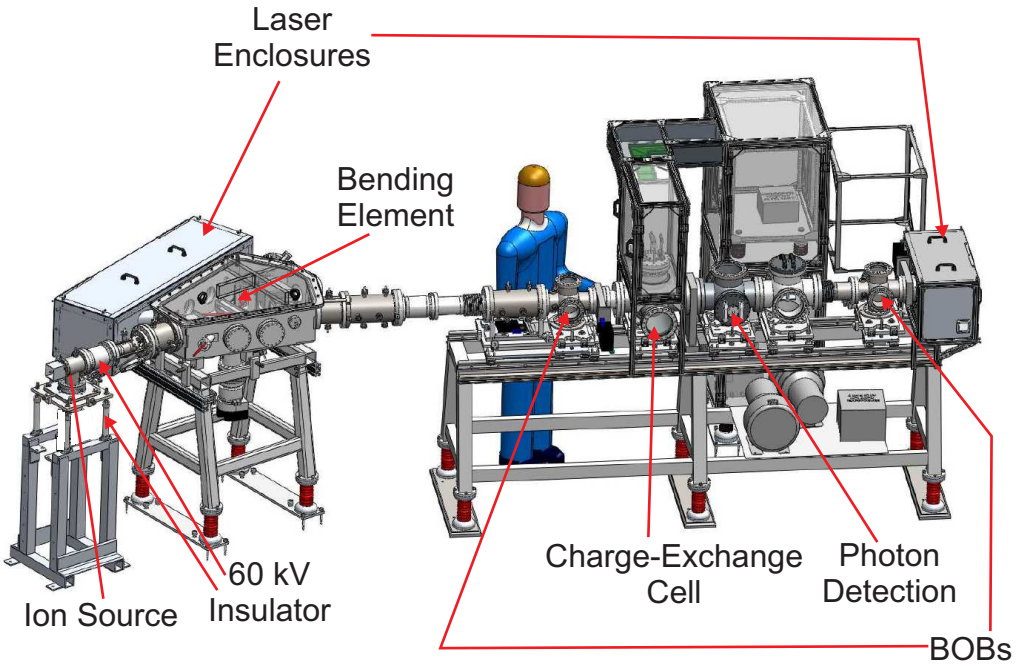

Figure 3.1: Conceptual design of the BECOLA facility used in the present work. Ion beams were generated in an ion source and deflected into the CLS beam line where the ion beam was co-propagated with laser light from an external source.

was electrically isolated from the transport beam line, which was held at ground potential. The extracted ion beam was accelerated and directed into the CLS beam line (Section 3.5) by an electrostatic deflector system.

3.2 Plasma ion source

The plasma ion source used for production of singly-charged ion beams in this work was a Model 100 Ion Source Assembly purchased from the Colutron Research Corporation [56]. A schematic diagram of the ion source is shown in Figure 3.2. The plasma source consisted of a 0.5 mm diameter tungsten filament placed inside a thermally and electrically insulating boron nitride chamber. An anode with a 0.1 mm diameter pin hole was mounted at the extraction end of the chamber. The tip of the filament coil was positioned approximately

5 mm from the anode. The source chamber was then mounted on a 70 mm Conflat flange, and a 6.35 mm (outside diameter) stainless steel tube was utilized to feed a gas through the vacuum flange and into the ion source chamber. The feed gas served as a buffer gas to stabilize the formation of the plasma. A 40-mm long ceramic tube with outer and inner diameters of 3.2 mm and 1.5 mm, respectively, was used as a charge holder for the ion source. The solid charge of interest was placed inside the tube. The charge was secured in the charge holder by packing 5 mm and 3 mm lengths of quartz wool into the downstream and upstream ends of the ceramic tube, respectively. The charge holder was also mounted on a stainless steel pushrod. The entire charge-holding assembly was placed inside of the 6.35 mm stainless steel tube used for gas feeding. A viton o-ring placed between the pushrod and 6.35 mm tube provided a vacuum break and served as a sliding surface when the pushrod was moved.

The entire ion source assembly was held at +15 kV potential by the FuG power supply. The filament was negatively biased relative to the anode, which was held at the FuG potential, using an Ultravolt power supply [57] that was able to apply a maximum of 250 V at 500 mA. The filament was resistively heated to incandescence using a TDK-Lamda [58] ZUP 20-20 power supply, which was floated at the potential of the Ultravolt power supply. A buffer gas of He or Ar was introduced into the source using an MKS [59] 248A leak valve. The buffer gas in combination with the thermally emitted and accelerated electrons generated a plasma near the anode pin hole. The ceramic tube was pushed inside of the cylindrical filament as necessary, resulting in the charge inside of the ceramic tube being radiatively heated by the filament. Some fraction of the vaporized charge was ionized in the plasma, extracted from the ion source chamber, and accelerated to the CLS beam line.

A plasma source configuration employing a heater was also used for increasing the temperature of the charge in the ceramic tube. The heater was a tungsten wire with a smaller

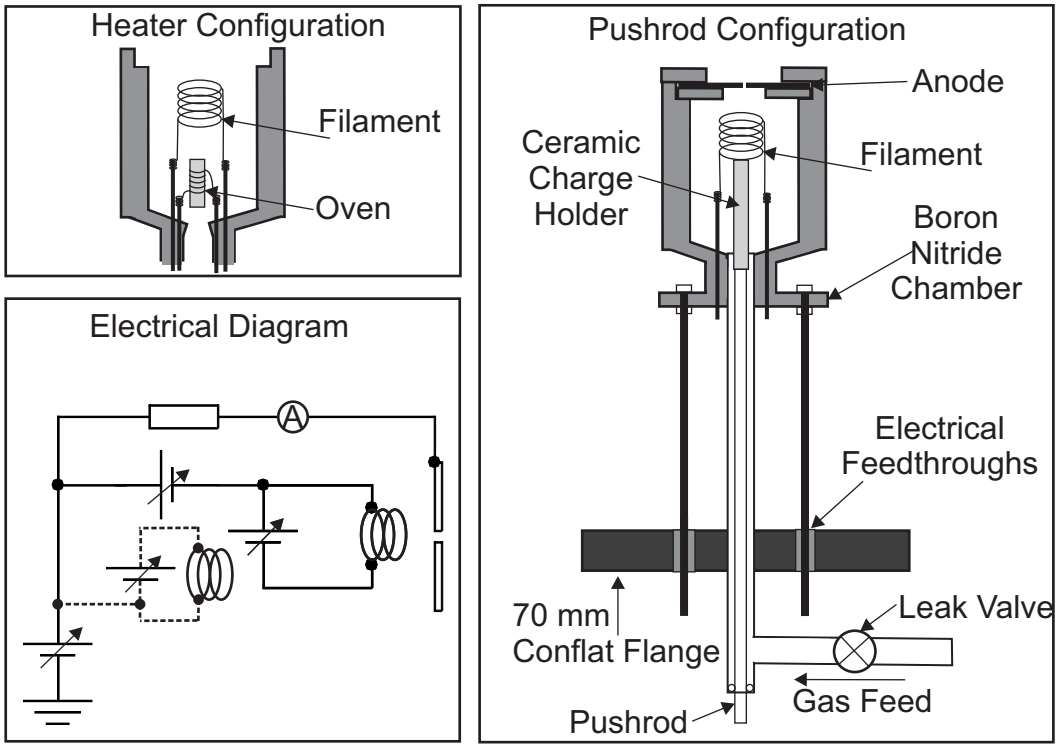

Figure 3.2: A schematic diagram of the electrical connections of the Colutron source is shown on the lower left; the optional heater is depicted with dashed lines. A schematic diagram of the pushrod configuration is presented on the right, and the heater configuration is shown in the upper left.

diameter than the plasma-generating filament. The heater was tightly wound around the ceramic charge holder and conductively heated the charge holder, allowing for a higher temperature to be attained compared to the radiative heating of the filament. The ceramic charge holder had to remain in a fixed location defined by the oven coil, therefore the pushrod could not be used to move the charge in the boron nitride chamber.

3.2.1 Operation and performance

The plasma ion source had a multiparameter operating space, including: filament bias voltage, filament input power, buffer gas type, and buffer gas feed rate. During operation, the typical filament power was held at 100 W (9 V at 11.1 A). The maximum power applied to the filament was 320 W (16 V at 20 A), which corresponded to a nominal maximum temperature of 2000 K based on the results presented in Ref [30]. The filament was typically biased at -125 V relative to the anode. The buffer gas was He, and Ar was also investigated. The parameter space was optimized to achieve a beam current that was stable at the level of a few percent or less over a time scale of five minutes.

With installation of a new charge, the plasma source was outgassed by increasing the temperature of the chamber by appling a voltage to the filament, typically 10 V. When the pushrod configuration was used, the ceramic charge holder was retracted from the boron nitride chamber during the outgassing process so that the charge did not vaporize during the offgassing process. Outgassing of the boron nitride chamber was found to take on the order of 6 to 8 hours to achieve a base pressure of 10^{-7} Torr. The chamber was then cooled by lowering the filament voltage, and the charge was pushed into the chamber to the desired location, usually to the base of the filament coil (Figure 3.2). The source was then operated and the desired beam extracted. As the extracted ion beam intensity decreased, the charge

holder was pushed further into the boron nitride chamber, to maintain a stable current. The limiting operating position of the push rod was when the ceramic tube reached the tip of the filament coil. The plasma ion source took approximately one hour to reach stable operation during daily startup. The daily startup routine was necessary to condition of the buffer gas through the leak value, and obtain thermal equilibrium of the ion source chamber after current was applied to the filament.

The startup conditioning process was accomplished as follows: the regulator attached to the He or Ar buffer gas cylinder was set between 5 and 15 psig. The regulator output was connected to the MKS 248A leak valve; the output of the valve was connected to the ion source via a T-connector upstream of the boron nitride chamber. The leak valve was controlled using a MKS 1249A solenoid valve driver, and a variable voltage in the range of 0-10 V was applied to the driver to adjust the flow rate of gas through the leak valve. The valve was sensitive when it was first opened; that is, the gas flow quickly jumped from no gas flow to high gas flow over a small step size of less than 0.1 V. The effect corresponded to a pressure increase of $> 1 \times 10^{-5}$ Torr from a baseline of 1×10^{-7} Torr, measured with a vacuum gauge placed 2 m downstream from the valve. The gas flow from the leak valve decreased after 30 to 60 seconds after the initial jump without a change in voltage. The leak valve was conditioned by iterating voltage increases and gas-flow jumps until a stable flow was achieved. A stable pressure measurement of 1×10^{-6} Torr was reached when a suitable gas flow was attained. The use of a buffer gas was optional; often ions of interest could be generated from charges without a buffer gas to stabilize the plasma.

The anode leakage current before the buffer gas entered the boron nitride chamber was typically around 0.02 mA. When the plasma was ignited by increased gas flow or increased filament power, the anode current increased to a value of >1 mA. A stable plasma was found

to be characterized by an anode current at least 1 mA that was stable to better than five percent for more than 30 minutes. After a stable plasma was achieved, the anode current was found to be insensitive to buffer gas flow. After startup, the intensity of the extracted ion beams from the plasma ion source was correlated with the filament power, and the lifetime of the charge varied and was dependent on the charge material used. Specific performance characteristics of the plasma source are presented in Section 4.1.

3.3 Electron ionization source

An electron ionization (EI) source was designed as part of this work to ionize gaseous both atoms and molecules. The EI source design was based on the ionizer scheme employed in the Stanford Research Systems [60] model RGA300 residual gas analyzer (RGA). The major components were obtained by modifying an "Ionizer Replacement Kit" for a RGA (part number O100RI). A schematic diagram of the EI source is shown in Figure 3.3. The source consisted of four electrically-isolated components: a repeller cage, a filament, an anode grid, and an extraction plate. A photograph of the EI source is presented in Figure 3.4. The source was mounted on a 70 mm Conflat flange in a geometry similar to that of the plasma ion source. The repeller cage was a wire mesh cylinder 50-mm long and 32.5 mm in diameter. One end of the repeller cage was open, and the other end, which was covered with mesh, was mounted on a 6.35-mm thick macor plate. The filament, anode grid, and extraction plate were mounted on a second insulating macor plate. The extraction plate was mounted directly on this macor plate. The anode was a mesh cylinder with one open end, 27-mm long and 15 mm in diameter. The open end of the anode cylinder was mounted 6 mm from from the extraction plate. The filament was placed in between the anode grid and repeller, 20 mm

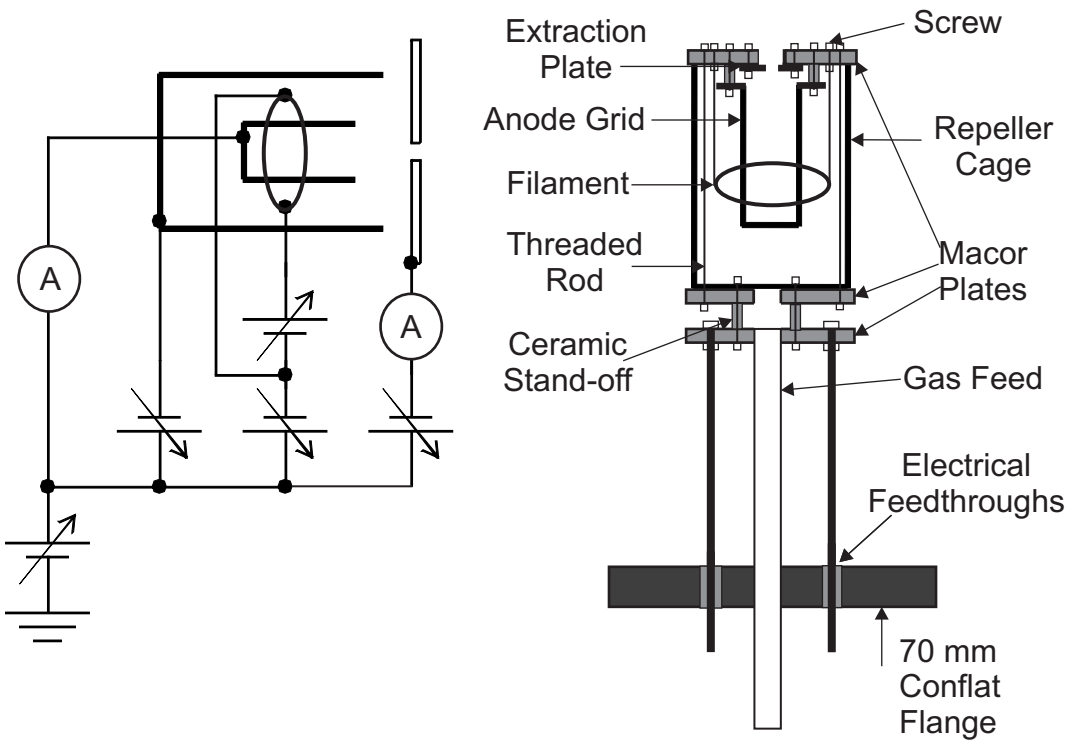

Figure 3.3: A schematic diagram of the electrical connections of the EI source is shown on the left, and a sketch of the physical assembly is shown on the right.

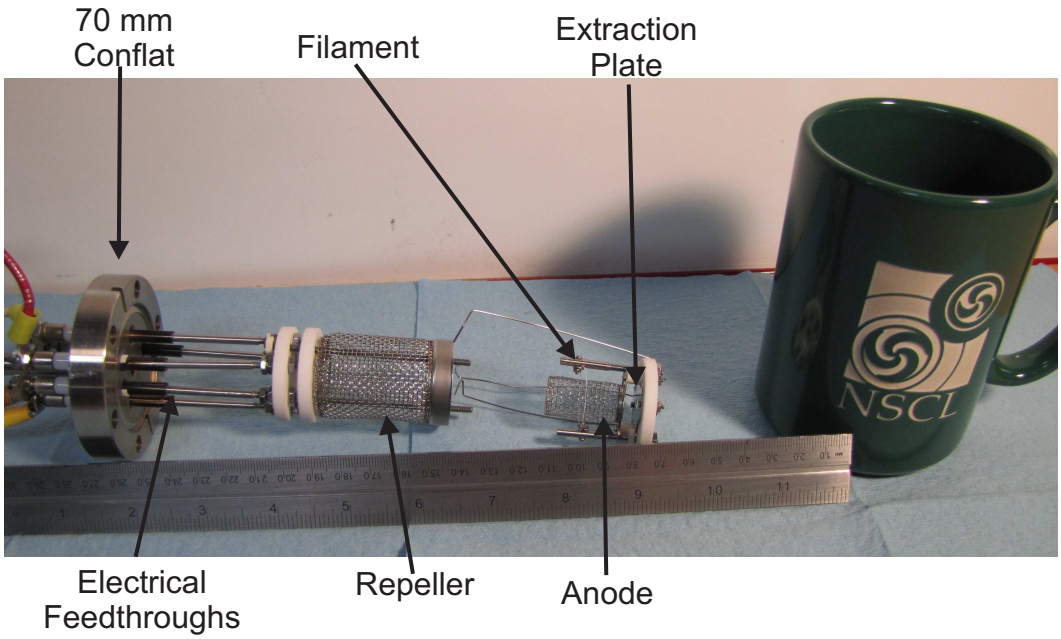

Figure 3.4: Photograph of the EI source. When fully assembled, the macor plate (white) with the filament, anode, and extraction plate was fastened to the repeller cage assembly.

upstream of the extraction plate. The filament was nearly a circular loop with a diameter of 22 mm. The two separate macor-plate assemblies were mounted together using two threaded rods and nuts. The repeller, extraction plate and filament were electrically isolated and were biased to -175 V, -150 V, and -125 V, relative to the anode, respectively. The filament bias was provided by the Ultravolt power supply described above. The extraction plate and repeller voltages were provided by an Ortec [61] 210 4-channel power supply. The filament was made of a thoria- (ThO_2-) coated iridium wire with a 0.25 mm diameter, and was heated to incandescence at a temperature between 1200 K to 1400 K [30] using the TDK-Lamda ZUP 20-20 power supply. Thermal electrons emitted from the filament were accelerated to, and generally passed through, the anode grid. The average energy of the electrons was 125 eV, which was sufficient energy to ionize gas molecules inside of the anode grid. Positive ions generated within the anode grid were drawn towards the extraction plate and extracted out of the ion source. Electrons that passed through the anode grid without interaction entered the opposite electric field region between the repeller cage and anode grid. These electrons were repelled and reaccelerated back towards the anode grid. The cyclic process of a particular electron passing through the anode grid continued until the electron was lost due to collisions with the gas or grid.

The gas feed into the EI source was similar to that into the plasma ion source. A 6.35-mm (outside diameter) tube was used to feed gas through the 70 mm Conflat flange into the EI source assembly. The MKS 248A leak valve controlled the flow of the gas.

3.3.1 Operation and performance of EI source

The EI source variables included the bias voltages applied to the repeller cage, filament and extraction plate, the size of the hole in the extraction plate, filament material type, and the

current applied to the filament. Optimization of these operational parameters is described in Section 4.1.

The filament, extraction plate, and repeller were typically biased at -125 V, -150 V and -175 V, respectively. On the order of 10 nA of ion beam were measured at the Faraday cup in the first Beam Observation Box (BOB) (Section 3.5.5) when 7 W (3.2 A at 2.2 V) was applied to the filament and the extraction plate had a 6.35-mm diameter hole. The EI source was operated with the available gas feeds for hundreds of hours without service because the charge of interest was introduced through the gas feeds. The charge could be changed without venting and servicing the EI source. An ion beam, with stability better than a few percent over 5 minutes, was extracted from the source within 5 to 10 minutes of turning on the ion source power supplies.

3.4 MIVOC chamber

A Metal Ion from Volatile Organic Compound (MIVOC) chamber was designed to feed the vapor of metal-containing compounds into the EI ion source. A photograph and schematic diagram of the MIVOC chamber are presented in Figure 3.5. A solid volatile organometallic charge, ferrocene for example, was placed in a charge-holding dish inside a 70 mm 6-way cross vacuum chamber. A photograph of the charge-holding dish is shown in Figure 3.6. A MKS 248A leak valve was placed between the MIVOC chamber and the ion source. With the leak value closed, the MIVOC chamber was evacuated to a pressure of $\sim 10^{-3}$ Torr, a level similar to the vapor pressure of the solid organometallic charge. The leak valve was then opened, and vapor from the MIVOC chamber entered the ion source chamber and was ionized. The limiting operational pressure of the MIVOC chamber occured when the pressure

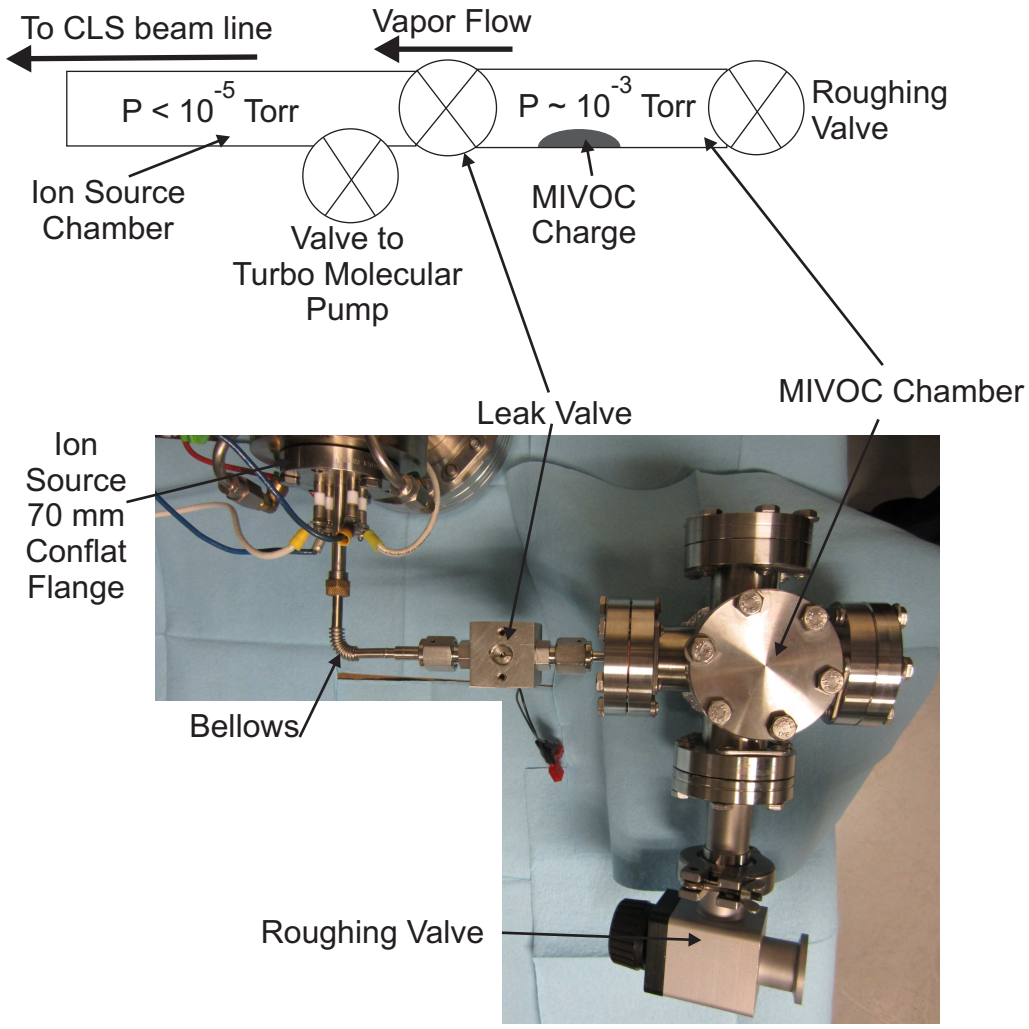

Figure 3.5: A schematic diagram (above) and photograph (below) of the MIVOC Chamber. The MIVOC chamber was vacuum pumped through the roughing valve, and the leak valve was opened to introduce the organometallic vapor into the ion source chamber. A bellows in the transfer line allowed for simple alignment of the two vacuum chambers. Heating tape, discussed in the text, is not shown in this photograph.

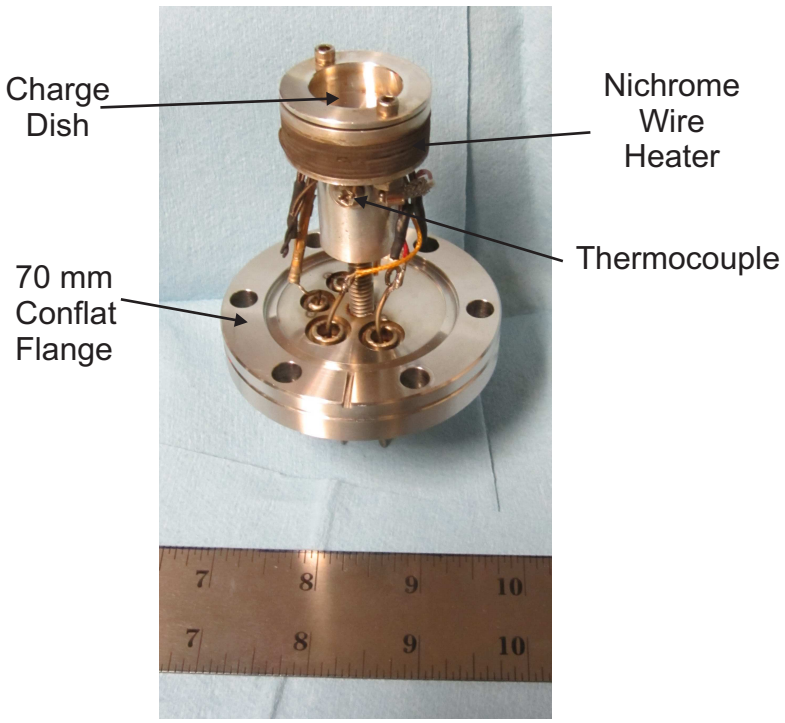

Figure 3.6: Photograph of the MIVOC charge holder. The charge holder was mounted on the bottom flange of the MIVOC 6-way cross vacuum chamber shown in Figure 3.5.

of the MIVOC chamber was greater than the EI source chamber, which was typically less than 1×10^{-5} Torr. The charge dish was wrapped with Nichrome wire, which was used to heat the dish to temperatures up to 373 K. A type-K thermocouple [62] was affixed to the base of the charge holder to monitor the temperature. The MIVOC chamber and transfer line to the ion source were wrapped with heating tape (BSAT101002, BriskHeat) with the intent to keep the chamber and charge-holder at similar temperatures and thus minimize condensation of the vapor on the chamber walls. The MIVOC chamber was mounted within the high-voltage cage of the ion source platform.

3.5 Collinear laser spectroscopy beam line

The CLS beam line was used to detect the laser-induced fluorescence from stable ion/atom beams in this work. A block diagram of the CLS components is shown in Figure 3.7. The major components included: the high vacuum system, ion optical elements, Beam Observation Boxes (BOBs), the Charge-Exchange Cell (CEC), the photon detection system, a residual beam deflector, the scanning high-voltage system, and the data acquisition system. The functionality and detailed description of each component is given below.

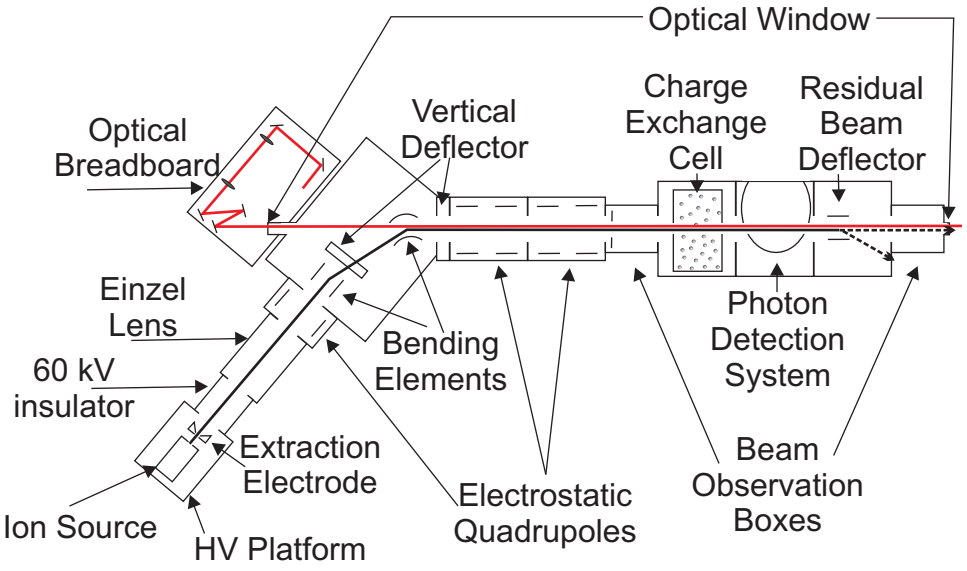

Figure 3.7: Block diagram of the CLS beam line. Individual components are described in the text.

3.5.1 High vacuum system

The vacuum system was divided into three separate sections: the beam switchyard, the CEC, and the photon detection system. A single scroll pump (TriScroll 600, Varian - 500 l/min) was used to provide the rough vacuum for the entire beam line, while each section had a dedicated turbo molecular pump (301 Navigator, Varian - 300 l/s for N_2) for achieving and

maintaining the required vacuum. A pressure at or below $<10^{-5}$ Torr is necessary for CLS measurements to minimize scattering of the ion/atom beam with residual gas molecules that results in resonance line broadening. The BECOLA CLS system was routinely operated at a pressure in the 10^{-7} Torr range. The beam line was vented, when necessary, with argon gas (purity of 99.99%) to reduce the oxidation of the alkali in the CEC, and oxidation of the polished aluminum reflector in the photon detection system [63].

3.5.2 Ion extraction from ion sources

The ion beam was extracted from the plasma ion source using an extraction electrode, which could be biased at a potential between 0 kV and -10 kV relative to the high voltage applied to the ion source. The extraction electrode, depicted in Figure 3.8, had cylindrical geometry, with a 40-mm diameter and 33-mm length. The electrode had a 8-mm diameter hole in its center, which was aligned with the beam axis, with the flat surface facing the ion source and an inverted conical shape facing downstream. The motion of positive ions from the ion source was simulated using the SIMION Monte Carlo software package, version 8.1 [64]. An example of the model for the ion extraction simulation from the plasma ion source is presented in Figure 3.8. The trajectories for the extraction of $^{55}Mn^{+}$ ions centered at the anode pinhole is shown. The extraction electrode was placed 10 mm from the anode of the ion source. The so-called ground tube was included in the simulation and was the first component on ground potential. The ensemble had 1000 particles with a 3D Gaussian spacial distribution at the anode with $\sigma = 0.2$ mm. The initial energy of the ions was 1 eV, and the ions had a random angular distribution over a 2π hemisphere toward the extraction electrode. The ion source was biased to +15 kV in the simulations, and the extraction electrode potential was biased between 12 kV and 15 kV (-3 kV to 0 kV relative to the ion-source potential).

The resulting emittance of the extracted $^{55}Mn^{+}$ ions was studied as a function of the bias voltage applied to the extraction electrode; the result is shown in Figure 3.9. The optimum beam emittance was predicted to occur at an extraction potential of -1 kV relative to the ion source high-voltage potential. The larger beam emittance when applying the smallest extraction electrode potential was due to a larger radial divergence of the ions compared to the ions extracted using a -1 kV potential. The increased radial divergence was due to a from a longer ion extraction time. The increased emittance at extraction electrode potentials greater than -1 kV were due to lensing of the ions from the relatively strong electrostatic field of the extraction electrode. The lensing effect increased the radial deflection of the ions. In practice, the extraction electrode was usually operated at -1.5 kV relative to the ion source potential.

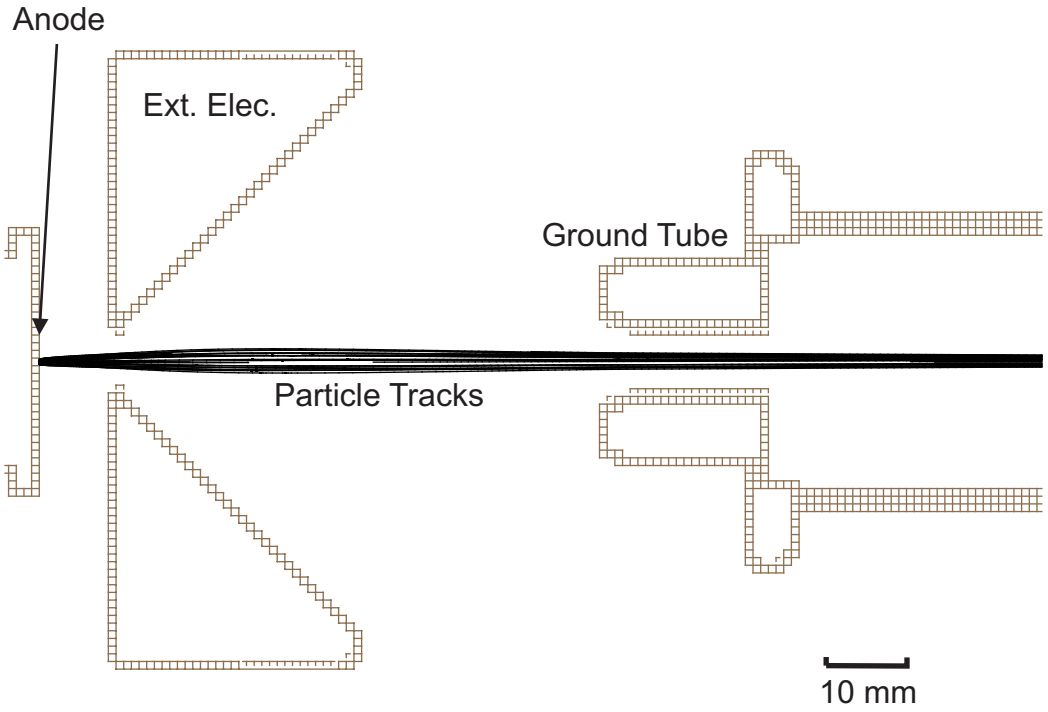

Figure 3.8: The geometry used for the plasma ion source simulations in SIMION. Example ion tracks are shown as black lines. The extraction electrode potential was -1.5 kV relative to the anode in this simulation.

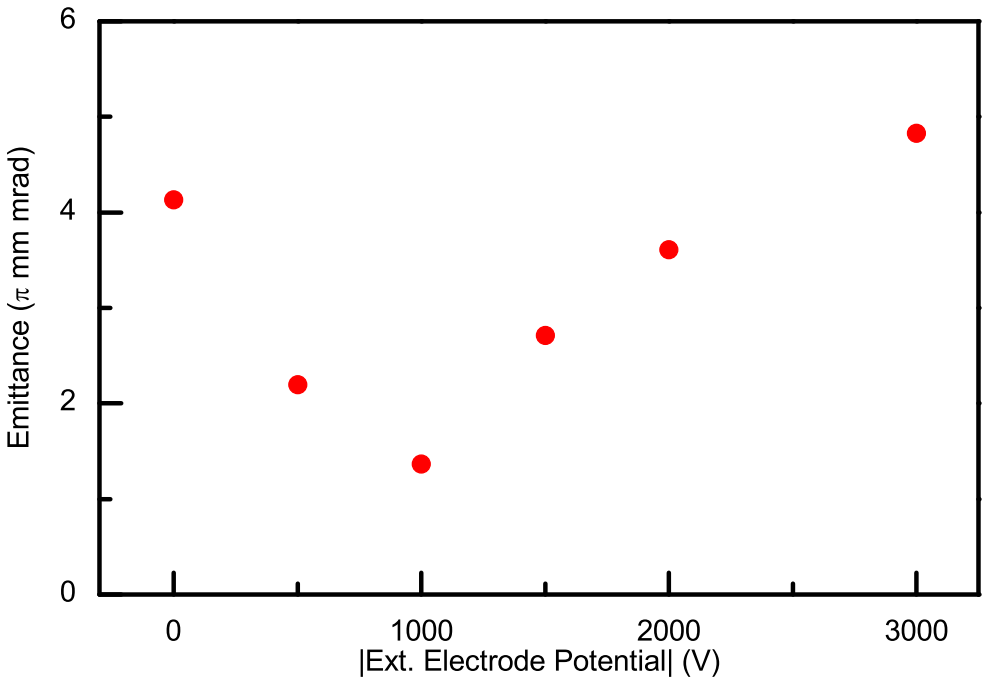

Figure 3.9: The emittance of a simulated 15 keV $^{55}Mn^{+}$ beam extracted from the Colutron plasma ion source as a function of extraction electrode bias. The sign of the extraction electrode bias relative to the ion source high voltage was negative, here the absolute value of the bias is the independent variable.

The extraction of a $^{55}Mn^{+}$ beam from the EI source was investigated as well. The geometry and electrostatic contours for the simulation of the EI source are presented in Figure 3.10. The anode grid and extraction plate were separated by 6 mm, and the extraction electrode was 10 mm downstream of the extraction plate. The ground tube/extraction electrode geometry was the same for the EI as that in the plasma source configurations. The anode grid was biased at +15 kV, and the extraction plate was biased at -150 V relative to the anode grid. The extraction electrode bias voltage was -1.5 kV relative to the anode grid. The source of ions in the simulation had a cylindrical spacial distribution with a length of 15 mm and a diameter of 5 mm centered on the beam axis, and displaced 15 mm longitudinally downstream from the upstream end of the anode grid. The angular distribution was distributed over 4π, and the ions had an initial kinetic energy of 1 eV. The electric field equipotential lines inside the anode grid is presented in Figure 3.10. The -1 V contour relative to the anode grid was predicted to protrude 12 mm into the anode grid from the downstream end. Given that the filament was positioned approximately 20 mm from the downstream end, it was assumed that most of the ions generated were upstream of the -1 V contour.

The dependence of the predicted beam emittance from the EI source is shown as a function of extraction plate hole diameter in Figure 3.11. The simulated emittance was found to be a factor of 2.5 larger for the 2-mm diameter hole compared to either the 4-, 6-, and 8-mm diameter holes. The larger emittance from a smaller extraction plate hole diameter was due to a lensing effect of increased radial deflection through the small diameter hole of the extraction plate. It is noted that the simulated emittance was none-the-less small, being less than 0.5 π mm mrad.

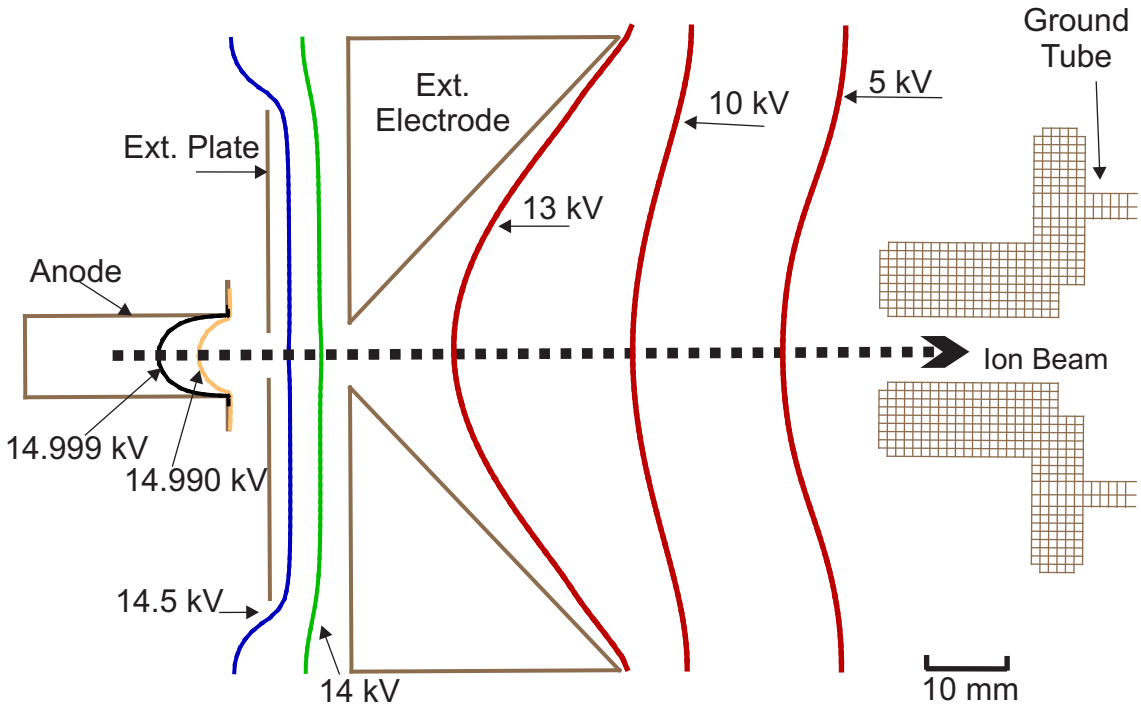

Figure 3.10: Schematic diagram of the geometry used for the simulations of the EI source in SIMION. The diameter of the hole in the extraction plate was 6 mm in this schematic. The solid lines represent equipotential contours.

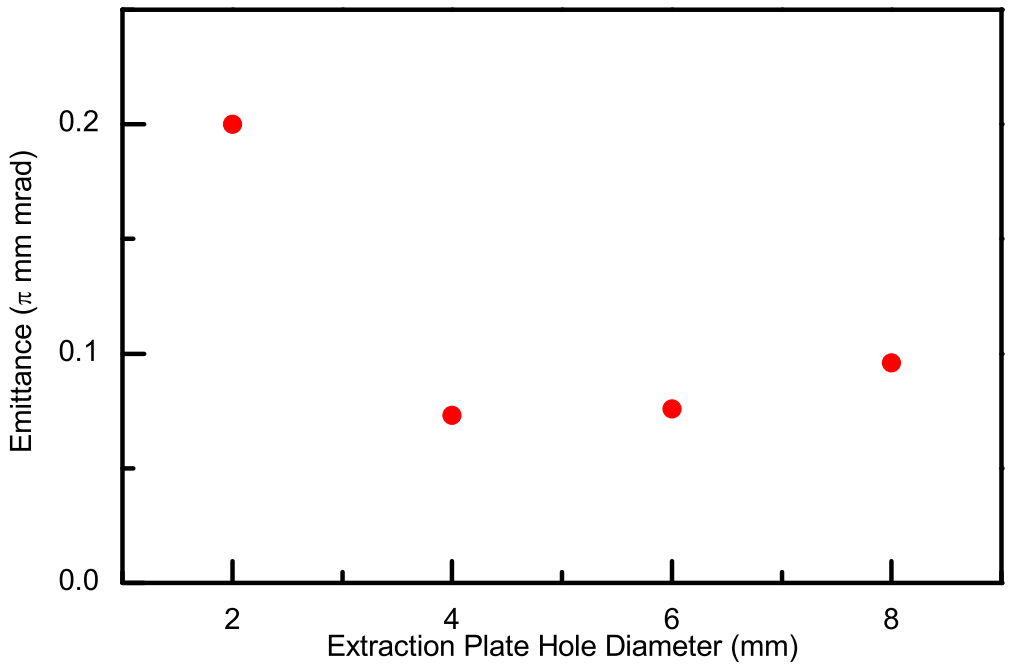

Figure 3.11: Simulated emittance from the EI source as a function of extraction plate hole diameter.

3.5.3 Ion beam transport simulations after the ion source

Transportation of the ion beam from the ion source down the CLS beam line was carried out using a series of electrostatic ion optical elements that are shown schematically in Figure 3.7. The usual convention for the coordinate system used for the ion transport simulations is shown in Figure 3.12. After extraction from the ion source, the beam passed through an

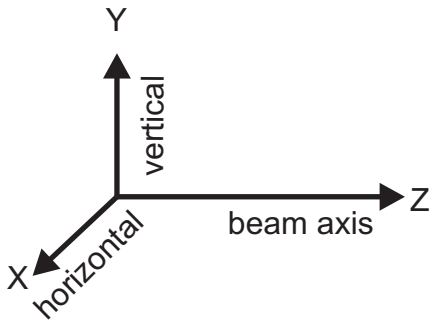

Figure 3.12: Representation of the coordinate convention of the ion beam used in the present work.

Einzel lens. The third electrode of the Einzel lens was segmented and also served as a beam steerer. Co-propagation of laser light with the ion beam required deflection of the ion beam. The beam was deflected a total of 30 degrees in the X direction by two elements: first a 15 degree parallel plate deflector and then and additional 15 degrees by a spherical bender. After each bending element, parallel plates were used to center the beam in the Y direction. An electrostatic quadrupole singlet was positioned upstream of the bending elements and used to de-focus the beam in the X direction to compenstate for abberations of the beam due to the electrostatic deflections. A pair of electrostatic quadrupole doublets was placed after the bending elements and before the first BOB. The quadrupole doublets served to focus the ion beam. The last ion optical element was a four-segmented electrode in the first BOB

that provided a final deflection of the ion beam in either X or Y, before it passed through the subsequent components of the CLS beam line.

The ion beam transport through the ion optical elements was simulated using the infinite-order analytical code COSY Infinity [65]. The voltage settings of the ion optical elements were systematically varied in the COSY simulations and optimized to minimize the ion beam waist symmetrically in the X and Y dimensions at either the photon detection system (position "A") or the end of the CLS beam line (position "B"). An example of an ion-beam envelope calculated using the COSY code is shown in Figure 3.13. The beam trajectories for the bending and non-bending directions are shown as dashed and solid curves, respectively. A 15 keV beam of $^{55}Mn^{+}$ with an emittance of 10 π mm mrad was used for the simulations (1 mm, 10 mrad). Two vertical solid lines in Figure 3.13 indicate the locations of the 5-mm diameter beam-line apertures described in Section 3.5.5. The voltages optimized during the minimization routine included those applied to: the Einzel lens, the quadrupole singlet before the bending elements (QS), and both sets of quadrupole doublets (QD1, QD2) after the bending elements. The bending elements are defined by a bending angle and radius, not by the voltage applied to the parallel/spherical plates. The bending elements were not varied during the minimization process, but the focusing of the beam through the elements (E1 and E2 in Figure 3.13) were included in the simulation.

The magnification, defined as the ratio of the distances of ions from the central trajectory at two points along the beam path, was calculated in the X and Y directions between the source of the ions and the photon detection system. The results of the simulations that were obtained for with and without use of the Einzel lens are summarized in Table 3.1. Use of the Einzel lens affected neither the other ion optical settings nor the quality of the transported ion beam in a significant way. The preferred optics solution was to achieve a symmetric point

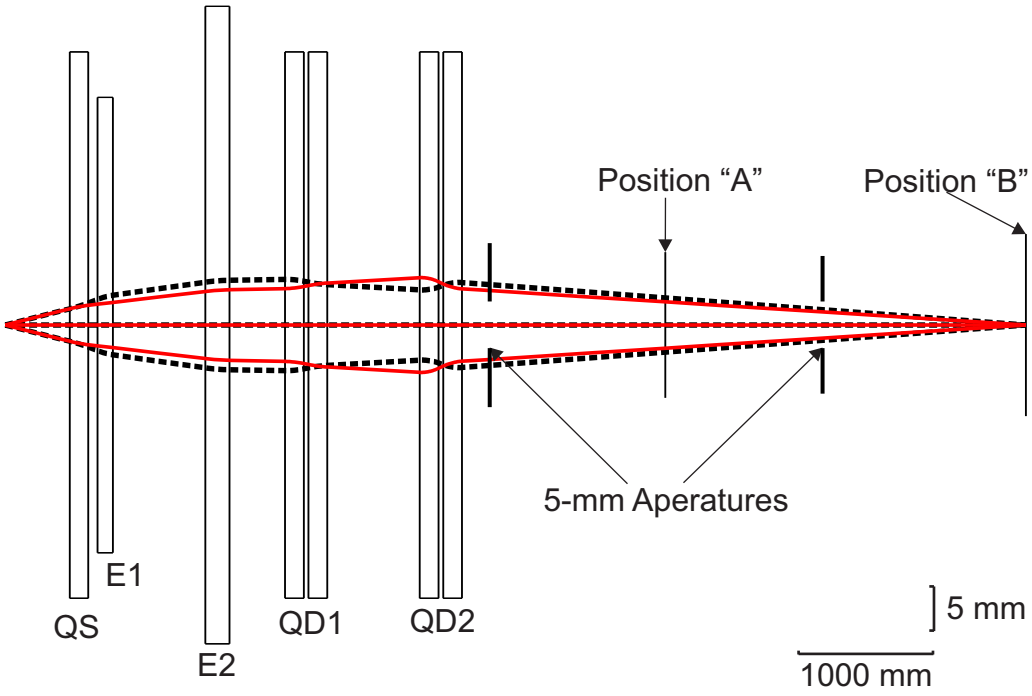

Figure 3.13: Simulated ion beam ray traces obtained using COSY infinity. The dashed and solid curves represent the X and Y directions, respectively. Note the different scales in the X and Y directions.

focus at the end of the CLS beam line; the magnifications at the focus at position “B” were 3.25 for both X and Y directions. The magnification was found to be independent of ion beam emittance for emittances less than 50 π mm mrad. Kinematically, the magnification decreases with the square root of increasing beam energy; thus, operating at the highest possible voltage has the advantage of minimizing the radial divergence of the ion beam in the CLS beam line.

3.5.4 Experimental optimization of ion beam transport

The initial values of the voltages applied to the ion optical elements were taken from the simulation results. One operational solution to transport the ion beam through the CLS beam line was then found by adjusting the applied voltages from the simulation results, and

Table 3.1: Optimum voltage values and magnification ratios for the symmetric focus in the COSY minimizations at positions "A" and "B". The bottom two rows were results obtained without inclusion of the Einzel lens in the minimization process.

Pos	X-Mag	Y-Mag	EL(V)	QS(V)	QD1(V)	QD1(V)	QD2(V)	QD2(V)
A	2.21	2.18	531	677	619	-404	-1730	1648
B	3.25	3.25	558	657	467	-321	-1210	1091
A	3.35	1.93	–	872	666	-470	-1305	1034
B	3.16	3.16	–	606	325	-179	-1270	1147

monitoring the ion beam current on Faraday cups located in the BOBs, which are described in Section 3.5.5. The ion beam transport maximization process was as follows: the voltages of the parallel plate and spherical electrode bending element, including the vertical steerers, were manipulated systematically to obtain a maximized beam current at the Faraday cup in the first BOB. The voltage applied to the quadrupole singlet was then adjusted to maximize the measured beam current at the first BOB, with additional (small) adjustments of the focusing using the bending elements voltages. The final focusing of the ion beam to the first BOB was achieved using a set of electrostatic quadrupole doublets downstream of the bending elements. The voltage settings of the first and second doublets were iteratively adjusted until the maximum beam current was measured at the first BOB. Additional adjustment of the bending and focusing elements was performed until the beam current measured at the first BOB reached a maximum value. The process was then repeated to optimize the beam current measured using the Faraday cup of the second BOB, near position "B" of the CLS beam line. The final tuning step was the application of voltages to the four segments of the steering electrode in the first BOB to maximize transport from the first BOB to the second BOB.

Table 3.2: Example of operational voltages applied to the BECOLA ion optics.

Element	EL	QS	QD1	QD1	QD2	QD2
Voltage (V)	0	150	125	-120	-180	135

The experimental voltage values for the ion optical elements were then entered as fixed values in COSY and used to visualize the beam envelope. An example set of experimental ion optical voltages are given in Table 3.2. The calculations in COSY with the operational voltages revealed that the ion beam was not symmetric in X and Y at the location of the photon detection system; the ion beam had magnification ratios of of 1.91 and 6.21 in the X and Y directions, respectively. However, the operational ion optical settings provided an acceptable beam envelope with reasonable transmission of 50-80% from the first to second BOB with 5 mm apertures in the beam path at both BOBs. The differences between the simulation results and the experimental results were mainly due to misalignment of the ion optical components from the central trajectory.

3.5.5 Beam observation boxes

The BOBs contained devices to measure ion/atom beam intensity and ensure alignment of the ion and laser beams. There were two BOBs along the CLS beam line (Figure 3.1); one upstream of the CEC, and the other downstream of the residual beam deflector.

Aperture plates mounted on linear drives were used to limit the size of the beam at the BOBs. Aperture holes with 3 mm, 5 mm, and 7 mm diameters were drilled in a 1.5-mm thick plate, which was mounted on the linear drive that was actuated in the Y direction. The aperture plate was centered in the X direction to within 0.1 mm of the beam axis using an optical telescope placed at the end of the CLS beam line.

A Faraday cup in the BOB was used to measure beam currents. The Faraday cup assembly was mounted on a pneumatic actuator that was used to remotely insert the cup into the beam path for a beam current measurement. The cup assembly consisted a metallic cup, and a secondary-electron suppressor ring, which were electrically isolated from each other and from ground potential. A schematic diagram of the aperture system and Faraday cup assembly is shown in Figure 3.14. The Faraday cup was mounted downstream of the aperture system so that the effect of the apertures could be measured to give an estimate of the beam size.

The induced current on the Faraday cup was measured using a picoammeter (Keithley, model 6487) or a NSCL Beam Current Monitor. Note that several electrons can be ejected from the surface of the cup due to impact of a 15-keV ion/atom beam and the number of secondary electrons emitted per incident atom/ion is called the conversion efficiency. The beam current due to positive ions was determined by applying a -50 V bias voltage to the electron suppressor, suppressing the number of secondary electrons that could escape from the cup. The intensity of atomic beams was determined by setting the voltage of the secondary electron suppressor to +50 V, so that all secondary electrons from the cup were ejected from the cup by the potential applied to the suppressor ring. An empirical value of the conversion efficiency was determined by reversing the polarity of the voltage applied to the electron suppressor while a pure ion beam of known intensity was impinged on the Faraday cup. The conversion efficiency was determined for each mass and beam energy used, and had values ranging from 2 to 10. Conversion efficiencies of around 3 are typical for singly-charged elements with 10's of keV of kinetic energy on a foil [66]. In this work, however, the species impinged on the foil included ions/atoms in elemental form along with a large fraction of molecular species. When the molecular species was impinged on the foil,

the increased number of atoms involved in the collision was thought to increase the observed conversion efficiency from the typical value of around 3 to values approaching 10.

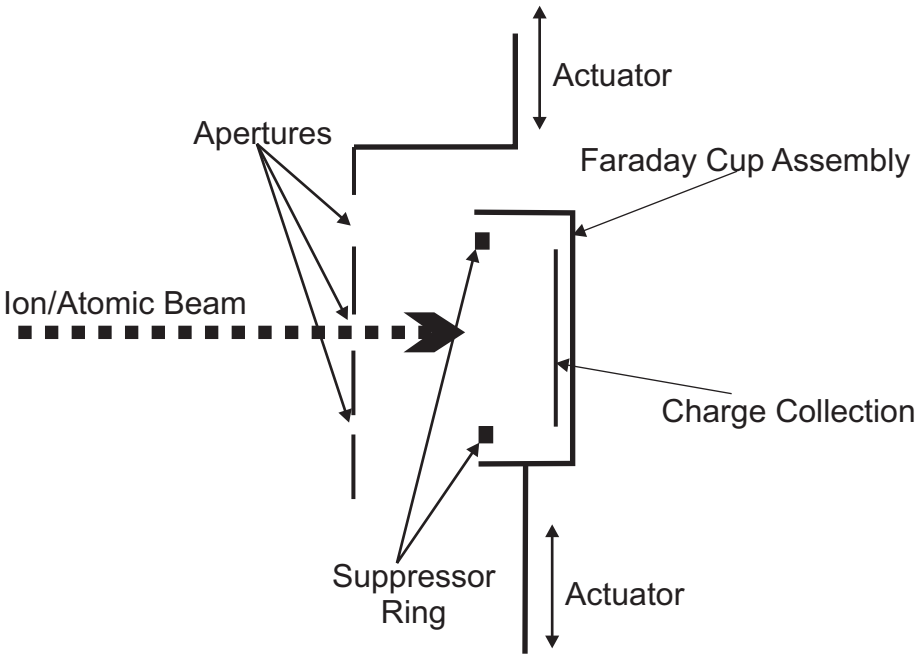

Figure 3.14: Schematic diagram of aperture system and Faraday cup assembly. The aperture system and Faraday cup assembly were mounted on actuators so that they could be inserted and removed from the beam path. The electrical connections and insulating mounting fixture connecting the suppressor and charge collector to the Faraday cup chasis are not shown.

3.5.6 Charge-exchange cell

A CEC was used to neutralize the ion beams via charge-exchange reactions of the ion beam with an alkali vapor [44, 45]. The vapor was generated inside of the CEC by heating a solid alkali metal. The conceptual design of the CEC is presented in Figure 3.15 and is based on the design of the CEC developed at TRIUMF [45]. The components of the CEC included: reservoir and heater, interaction and condensing regions, beam inlet and outlet ports, and viewing ports. The CEC assembly was vertically mounted on an 203 mm Conflat flange such that the reservoir was suspended below the beam axis and the condensing region was

located above the beam axis. The complete CEC assembly was electrically isolated from the vacuum chamber at ground potential. A high voltage (± 10 kV maximum) was applied to the CEC via a series of electrodes connected to a resistor chain. The electrodes were designed to smoothly shape the electric potential from ground to the high voltage applied to the CEC assembly.

The reservoir contained the solid alkali metal and was resistively heated using a 17-Ω wire coil that was covered by a copper jacket to provide uniform heating. The reservoir was connected to the beam interaction region by a stainless steel vertical tube that had a 22-mm inner diameter. The vaporized alkali rose through the interaction region where it intersected the ion beam. The vertical CEC was 127 mm in length along the beam axis, and geometrically defined the interaction region between the incident ion beam and alkali vapor. Note that the alkali vapor did not have a uniform density across the entire geometrical interaction region. The effective interaction length was mostly determined from the solid angle of the beam axis seen from alkali in the reservoir and was estimated to be (35 ± 5) mm.

The beam inlet and outlet ports were 35 mm in length and had an opening diameter of 16 mm. The ports had a conical geometry to help return the alkali vapor into the central region. Typically, 100% of the ion beam passed through the 16-mm openings of the beam inlet and outlet ports. The alkali metal was condensed to liquid at the upper condensing region by holding the temperature of the inner wall of the vertical tube at only a few degrees above the melting temperature of the alkali metal. A silicon-based heat-exchange fluid (Julabo C20S) was circulated using an external bath heater/chiller circulator (Thermo Scientific A28) to control the temperature in the condensing region. After condensation, the alkali metal returned to the reservoir along the walls via gravity. The alkali vapor density was controlled by varying the temperature of the reservoir.

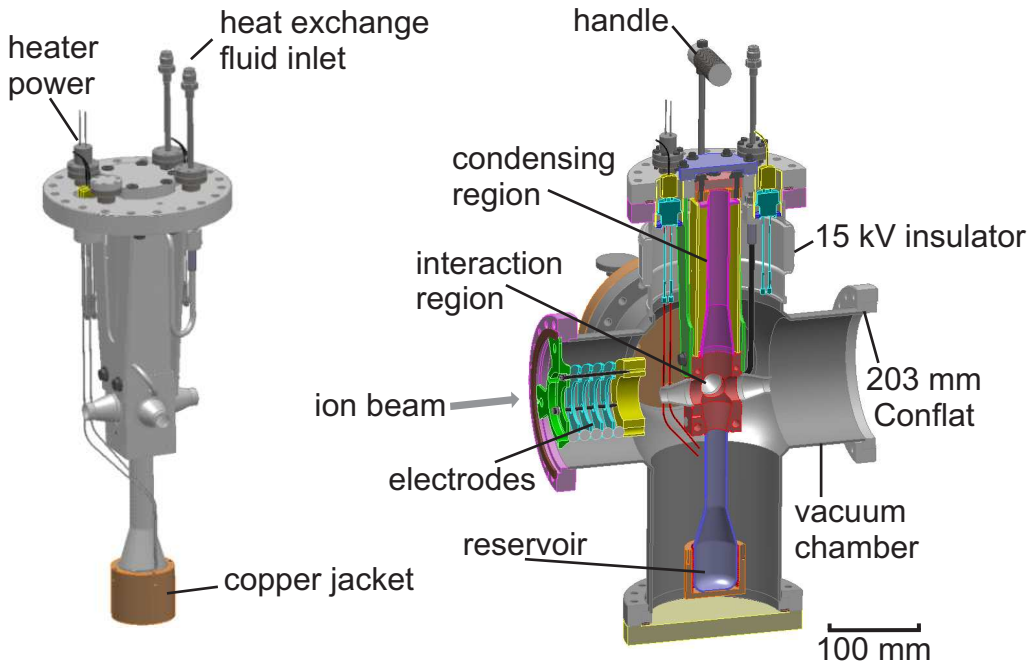

Figure 3.15: Conceptual design of the CEC assembly (left) and cut away view of the CEC in the vacuum chamber (right).

The CEC was commissioned by studying the neutralization of a 10 keV Rb^+ beam with a K vapor at the University of Mainz and the results have been published [45]. The commissioning tests revealed that the alkali vapor density at the interaction region was 1-2 orders of magnitude below the saturation vapor density expected for the temperature of the reservoir.

Sodium was used as the charge-exchange alkali in the work discussed here. The heater was operated at a temperature of 623 to 723 K (± 2 K for a single HFS scan), and the condensing region was held at a temperature of (373 ± 5) K. The vapor density of Na in the interaction region of the CEC was approximately 1×10^8 cm^{-3}, assuming the vapor was 50 times lower than the saturation density [3, 67] based on results in Ref [45]. Typical neutralization efficiencies were found to be between 30% and 50% for these operating conditions of the CEC.

It should be noted that a stainless-steel mesh cylinder was placed vertically from the reservoir to ∼10 mm below the interaction region for the work presented in Ref [45] but was not used in the present studies. When the mesh was used, the condensed alkali vapor could be recycled back to the reservoir via wicking action on the mesh in addition to gravity. The maximum temperature for stable CEC operation in this work was found to be ∼730 K; the installation of the mesh may have allowed for a higher temperature to be achieved.

3.5.7 Photon detection system

A photon detection system was used to collect light from the laser-induced fluorescence from the ion/atom beams. The photon detection system was described by Vinnikova [63] and was composed of the following: an ellipsoidal reflector, an inverted quartz-window viewport, a photomultiplier tube (PMT), a circular iris in front of the PMT head, and four conical apertures along the beam axis. A mechanical drawing of the detection system is shown in Figure 3.16. The ellipsoidal reflector was fabricated from aluminum and hand polished to a reflectivity of $(60 \pm 2)\%$ for 397 nm laser light. The ellipsoidal reflector was mounted on an 203 mm Conflat flange and electrically isolated from the vacuum chamber, which was held at ground potential. The semi-minor ellipsoidal axis was parallel to the beam axis, and had a radius of $b = 38.1$ mm. The semi-major axis of the ellipsoidal reflector had a radius of $a = 53.3$ mm and was perpendicular to the beam axis. A schematic diagram of light collection from the ellipsoidal reflector is presented in Figure 3.17. The beam entered and exited the reflector through 16-mm diameter openings and passed through one focus of the ellipse. Laser-induced fluorescence from the ion/atom beam reflected off the aluminum surface, passed through the quartz vacuum-window, and was incident on the photocathode of a Hamamatsu H11123 PMT placed at the second focus of the ellipse. A scalar module

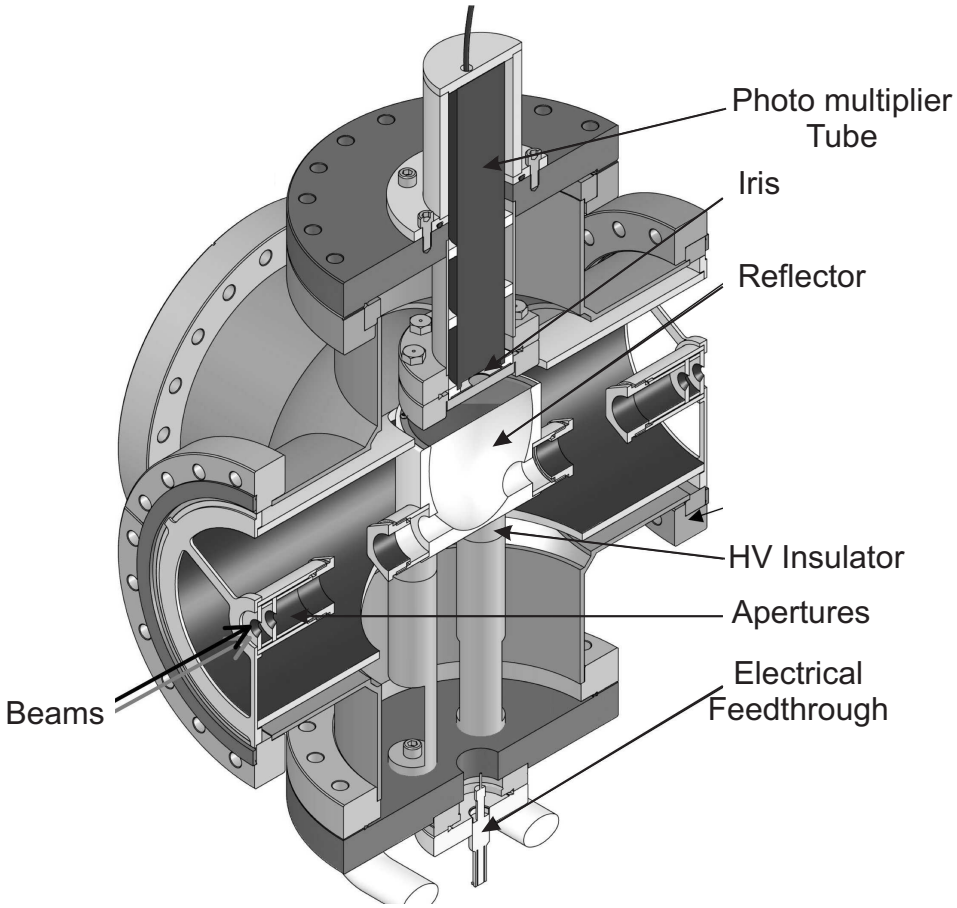

Figure 3.16: Mechanical drawing of the photon detection system used in this work.

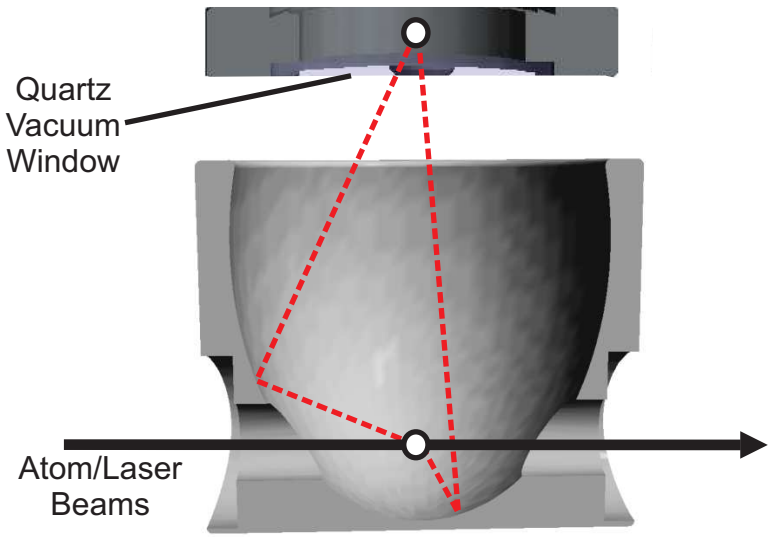

Figure 3.17: Co-propagated atomic and beams passed through one focal point point in the ellipse, which is shown as a white circle. The dashed red line represents the reflection of laser-induced fluorescence emitted by the ion/atom beam at the focal point. The photocathode of the PMT was placed near the quartz window at the second focal point of the ellipse.

was used to read out the PMT electric signals generated by photons that hit the PMT photocathode; the scalar module and data acquisition system are described below.

Background from scattered laser light and the signal from laser-induced fluorescence was found to be spacially separated at the second focal point of the ellipsoidal reflector [63]. Rejection of the background light was achieved by placing a 19-mm diameter iris in front of the photocathode of the PMT at the second focal point of the ellipsoidal reflector.

Scattered laser light that entered the aluminum reflector was reduced by placing four conical-shaped apertures along the beam axis at the entrance and exit of the large vacuum chamber which housed the reflector assembly. Each pair of apertures were separated by 15 mm, and the openings were 7 mm and 8 mm in diameter for the apertures that were furthest and closest to the reflector, respectively. The outermost apertures cut out any halo of laser light, and the inner apertures absorbed any light scattered by the outer apertures.

The interior of the entire 6-way cross vacuum chamber and all apertures were coated with conductive black paint to absorb scattered light.

3.5.8 Residual beam deflector

A residual ion-beam deflector was positioned downstream of the photon detection system. The deflector was composed of two aluminum plates that were aligned parallel to the beam path, with a 50 mm gap and 100 mm in length. The deflector was used to deflect the residual ion beam after the charge-exchange cell and fluorescence detection region. The deflection of residual ion beam after charge-exchange allowed for beam current measurements of the neutral beam using the Faraday cup of the second BOB as described above.

3.5.9 Data acquisition

Fluorescence signals were collected by recording the PMT signal as a function of beam velocity. A block diagram of the HV control and data acquisition system is shown in Figure 3.18. Computer control of the HV relied on a VME-based system that consisted of a Digital to Analog Converter (DAC) with 18-bit resolution (HYTEC 2670, WIENER). The DAC output (-5 V to 5 V) was filtered by an isolation amplifier to reduce noise, and was used to drive a AMP series Matsusada $\pm$10 kV DC amplifier. The amplifier output was applied to the CEC or ellipsoidal reflector for atom or ion spectroscopy, respectively. A 10 kΩ resistor was placed in series with the amplifier output to limit current fluctuations. A typical scan of the HV covered a 500 V range in 1 V steps with a 0.25 s dwell time per step. A VME scalar module was used to record the PMT signal at each voltage step. Communication with the VME crate was achieved via a CSS [68] software package. Variables for a voltage scan

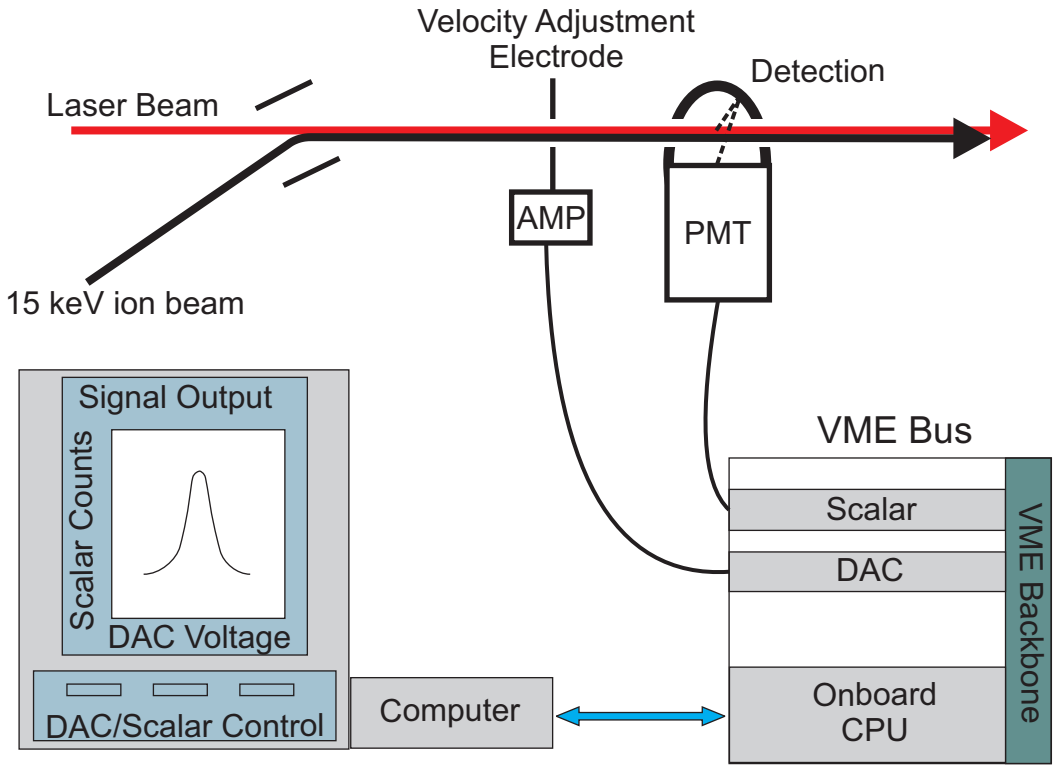

Figure 3.18: Schematic of the scanning high voltage and data acquisition system.

included: the initial and final voltages to be applied, the step size, the dwell time, and the number of scans. The local computer monitor displayed the PMT response as a function of set voltage (the HFS) after each scan, along with the cumulative spectrum. The raw data were recorded for further analysis.

The high voltage scanning system was calibrated by measuring the high voltage output from the Matsusata amplifier as a function of the set voltage. The high-voltage was measured using a precision high-voltage divider (Ohm Labs Model KV-25), and the result is presented in Figure 3.19. The output of the high-voltage divider (1500:1 ratio) was connected to a 6.5 digit multimeter and the output voltage was recorded as a function of applied voltage. The slope and intercept of the calibration curve for a range of -3 kV to +3 kV are given in Figure 3.19. The typical range used for most high-voltage scanning in this work was between

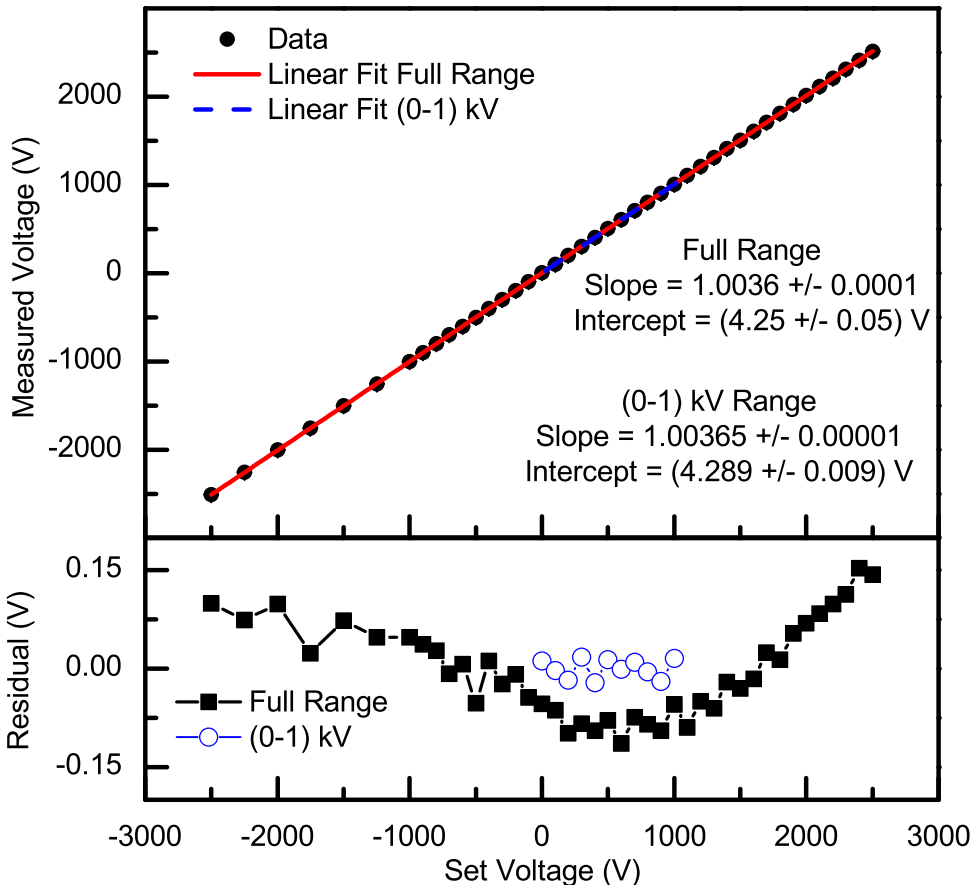

Figure 3.19: Scanning high voltage system calibration.

0 V and +1 kV. The extracted slope and intercept from a linear fit to data in the 0 V to +1 kV range were 1.00365 ± 0.00001 and (4.289 ± 0.009) V, respectively.

3.6 BECOLA laser system

The laser system used for the CLS studies in this work was a continous-wave solid-state laser system that was frequency stabilized via an external reference. A photograph of the laser system is presented in Figure 3.20. The laser system was assembled from commercially available components, which are described below. The conditions for stable and safe laser operation required placing the laser system in a single purpose, limited access room, separated some 20 m from the CLS beam line of the BECOLA facility. Additionally, the optical breadboard used as a table for the laser system was mounted on vibration-damping legs to minimize effects from building vibrations, and the laser system was enclosed in a plexiglass structure with a HEPA fan filter to limit dust and dirt accumulation on the sensitive optical components.

3.6.1 Ti:Sapphire laser and diode pump laser

The BECOLA laser system relied on a Ti:Sapphire ring laser (Matisse TS, Spectra Physics), which was pumped using a 15 W continous-wave 532 nm laser (Millennia Pro 15sJ, Spectra Physics). A schematic diagram of the optical elements of the Ti:Sapphire ring laser are shown in Figure 3.21. Continuous Visible/Near Infrared (Vis/NIR) laser light in the wavelength range of 700 nm to 1000 nm can be generated from this lasing system. Laser power was optimized for a given wavelength and was typically between 1-2 W for a 10 W power setting of the pump laser.

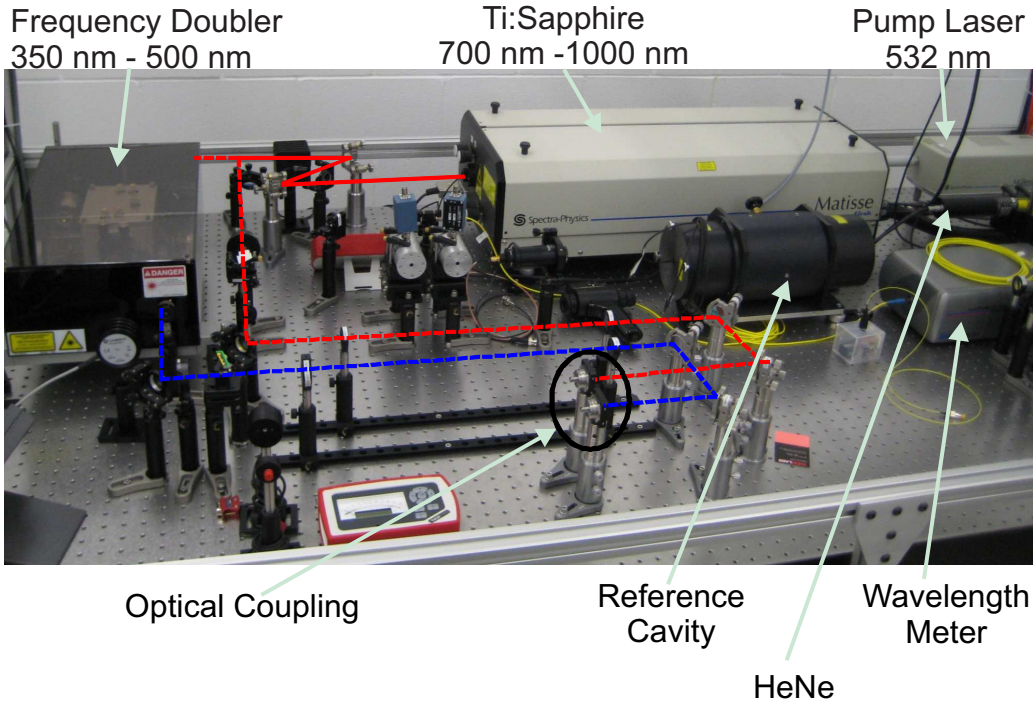

Figure 3.20: Photograph of the continuous-wave laser system used in this work.

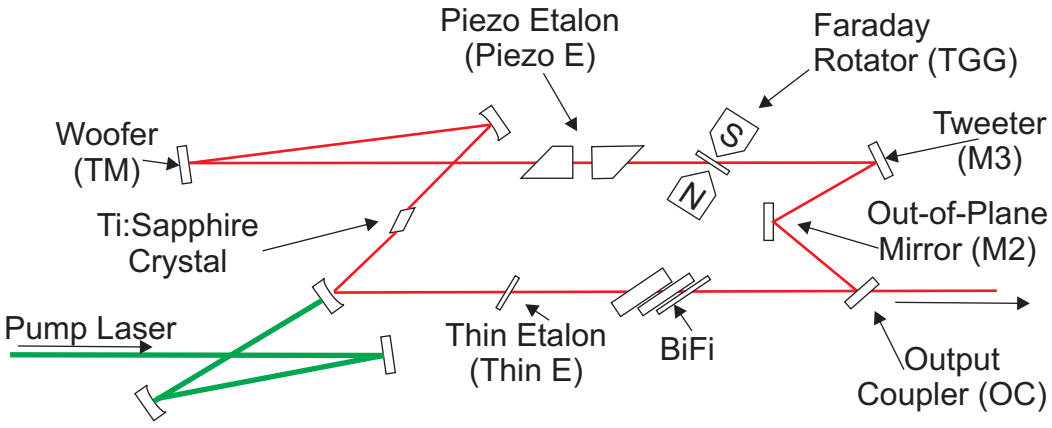

Figure 3.21: Schematic diagram of the Ti:Sapphire ring laser cavity. The labeled elements are described in the text. Labels in parentheses indicate the naming convention defined by the vendor [2].

The Free-Spectral Range (FSR) of the Matisse optical cavity was 160 MHz, leading to approximately 350,000 modes over the entire bandwidth of the lasing medium. Four frequency-selective elements were used in the optical cavity to reduce the broadband light to a single mode to provide narrow-bandwidth light. The Matisse ring laser had three mirror sets coated to be reflective over a $\sim$100 nm bandwidth. The mirror sets were interchangeable, and a particular mirror set was selected based on the desired wavelength. Laser wavelengths outside of the respective bandwidth (e.g. 750 nm to 870 nm for one mirror set) suffer reflective losses resulting in reduction of the intensity of outgoing light. A birefringent filter (BiFi) consisting of three stacked quartz plates of varing thicknesses in the ratio of 1:3:15, was positioned at Brewster's Angle with respect to the incident laser beam. The thickness of the thinnest plate was on the order of 300 μm. The bandpass of the BiFi was 50 GHz, and was tunable to cover the entire wavelength range for a given mirror set. The BiFi was tuned by rotating the quartz plate with respect to its surface normal using a motor-controlled fixture. A solid state Fabry-Perot etalon, called the thin etalon, with a FSR of 250 GHz with a relatively high-finesse, or large spacing of transmitted optical modes relative to the width of the transmitted modes, was utilized to further reduce non-desirable lasing-modes that were resonating in the optical cavity. Finally, a Piezo Etalon (PE), with a FSR of 20 GHz and a low-finesse of about 3 was tuned such that all but one laser mode had high attenuation losses in the optical cavity.

A by product of the ring geometry of the optical cavity was that counter propagating modes of the same frequency could exist. Unidirectional mode operation of the ring optical cavity was achieved by reflecting the laser beam from an out-of-plane mirror and passing the beam through a terbium gallium garnet (TGG) crystal placed in a strong magnetic field. The polarization vector of the electric field was rotated by a few degrees by the TGG

crystal regardless of the propagation direction of the laser light (a so-called Faraday rotator). The out-of-plane mirror also rotated the polarization vector, in a way that depended on the laser-beam propagation direction. The so-called "optical diode" had no overall effect on the counter-clockwise-propagating beam, but suppressed the clockwise-propagating laser light by increased reflective losses at the Brewster surfaces of the optical cavity.

3.6.2 Ti:Sapphire laser frequency stabilization

Two feedback mechanisms were utilized to stabilize the frequency of the Ti:Sapphire ring laser. A confocal resonator with an FSR of 600 MHz and a finesse of approximately 15 was employed as a reference cell to provide feedback to the Ti:Sapphire optical cavity and reduce short-term frequency jittering of the laser line width. The transmission through the resonator was recorded by a photo diode. A feedback loop was locked onto the half-maximum intensity of the side of an Airy-fringe of the transmitted laser intensity monitored by the photo diode [69]. Any intensity variation at the locked-in frequency was interpreted to be from a frequency jitter of the Ti:Sapphire laser. If the measured intensity at the locked-in frequency varied, feedback was sent to piezo actuated mirrors in the Ti:Sapphire cavity that compensated for the change through the feedback loop. This resonator feedback produced a narrow laser linewidth on the order of 100 kHz on a time scale of ms.

Stabilization on a longer time-scale (minutes to hours), was achieved by comparison of the laser frequency to an external reference using a wavelength meter. The external frequency was provided by the 633 nm light from a frequency stabilized helium-neon laser (Research Electro-Optics, Inc.), which had a frequency stability of ± 2 MHz over 8 hours. The absolute frequency of the helium-neon laser had uncertainty of ± 300 MHz. The external reference and Ti:Sapphire frequencies were compared using a High Finnese Angstrom WS Ultimate

wavelength meter, in which a Fizeau interferometer [10] was used to compare the frequencies. A feedback signal from the wavelength meter was used to adjust the Ti:Sapphire piezo mirror system. Feedback signals from both the short- and long-term stabilization were mixed and used to adjust two peizo-mounted mirrors; one operating a higher frequency (tweeter), and the other operating at a lower frequency (woofer) to stabilize the frequency of the Ti:Sapphire system.

3.6.3 Second harmonic generation cavity

A WaveTrain (Spectra-Physics) frequency doubler was used to generate the second harmonic (SHG) that converted a fraction of the VIS/NIR laser light from the Ti:Sapphire laser into UV/Vis laser light. SHG was achieved by angle phase matching through a nonlinear lithium triborate (LBO) crystal [70]. The LBO crystal was placed in a resonator cavity to increase the conversion efficiency for SHG [71]. A schematic diagram of the resonator cavity is shown in Figure 3.22. The resonator cavity was configured in a triangular geometry, with two

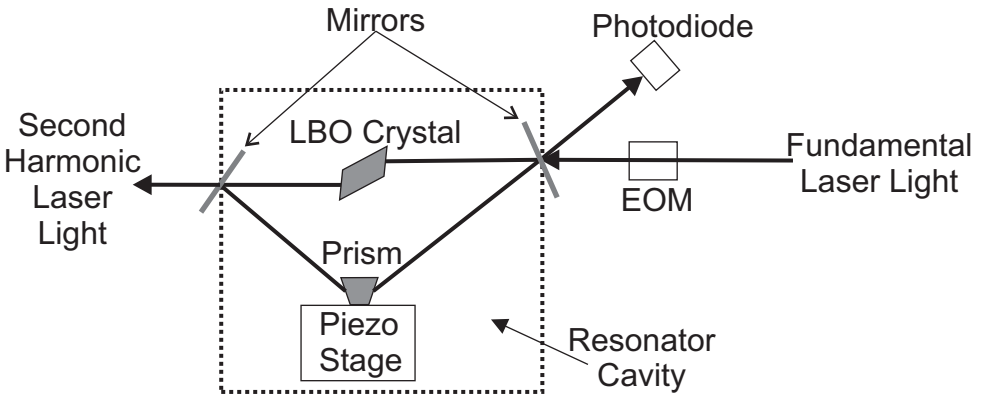

Figure 3.22: Schematic diagram of the WaveTrain frequency doubler. The translation and phase matching stage of the LBO crystal is not depicted in the figure, see the text.

mirrors and a prism that was mounted on a piezo platform. A fraction of the horizontally-polarized fundamental light from the Ti:Sapphire ring laser was transmitted through a highly

reflective mirror and entered the cavity. The fundamental light then passed through the LBO crystal, was reflected by a second mirror, was refracted through a prism, and then again was reflected by the first mirror. The vertically-polarized second harmonic beam generated in the LBO crystal exited the resonator cavity through second mirror.

The WaveTrain unit was actively stabilized using the Pound-Drever method [72]. The fundamental laser light sidebands necessary for the Pound-Drever stabilization were generated using an Electro-Optic Modulator (EOM) prior to the beam entering the WaveTrain resonator cavity. The interference of the fundamental beam with the sidebands was imaged using a photodiode, which was positioned to collect the fundamental light that was reflected by the first mirror. A feedback loop from the Pound-Drever apparatus was used to stabilize the resonator cavity by adjusting the applied voltage to the Piezo-motor platform, on which the prism was mounted.

In general, the second harmonic power is proportional to the square of the fundamental input power and the WaveTrain SHG output power was found to range from 2% to 15% of the fundamental Ti:Sapphire power. Translation of the LGO crystal and phase matching the light through the crystal were critical to achieve the optimum second harmonic power, provided that the mode matching of the fundamental light with the cavity was good.

3.6.4 Light transportation to the CLS beam line

Optical fibers were used to transport the laser light by ∼20 m from the laser room to the CLS beam line. The transport of the laser light through the air using a mirror system was initially considered but the necessary system to compensate for mirror vibrations would have been expensive to implement and would have come with significant safety concerns. Building vibration provided additional potential for risk; slight vibrations or instabilities in mirror

mounts would cause significant optical misalignment over 20 m. Optical fiber transport avoided all of these concerns. Single mode fibers were chosen that transmit only the lowest-order excitation mode of light in the fiber. This mode has a Gaussian transverse power distribution and small divergence compared to higher-order modes making manipulation of exiting light significantly easier. The specific fibers that were tested included: Thorlabs PM-350-HP, PM-405-HP and PM-630-HP, along with a large mode area fiber from NKT photonics (Newport LMA-PM-5). Note that optical fibers are characterized by, for example, the effective area the fiber covers in transverse dimensions, or effective mode area. The fibers used had small effective mode diameters, about 2 μm for the single-mode fibers and 5 μm for the large mode area fiber.

Control of the size and divergence of the incoming laser beam was critical to achieve efficient light coupling. A beam telescoping system, consisting of two lenses of equal focal length, was installed to control the size of the beam. A photograph of the telescoping system is presented in Figure 3.23. The laser light to be coupled into the optical fiber was first impinged on the input coupler. The positions of the telescoping lenses were then adjusted so that the laser beam diameter at the focusing lens of the input coupler was ~ 4 mm, about half of the diameter of the lens. As the first step of the alignment procedure, a laser diode with an optical fiber output was attached to the coupler, and the light from the diode was back-aligned with the input laser light using a tuning mirror placed near to the coupler. The incoming laser light was then tuned using the adjustment mirror directly following the telescoping lens so that the light passed through the center of the input coupler lens. The process was iterated until the incoming laser light passed though the coupler lens, and the back-coupled light was co-propagated with the incoming light. The back-alignment process

was critical to achieve initial rough alignment of the incoming laser light through the optical fiber.

Following the back-alignment process, the percentage of incident laser power transmitted through the optical fiber was maximized by comparison of the laser power measured before and after the optical fiber. The optimization process was initiated by adjusting the X and Y screws of the fiber coupler, shown in the bottom of Figure 3.23. After optimization of the

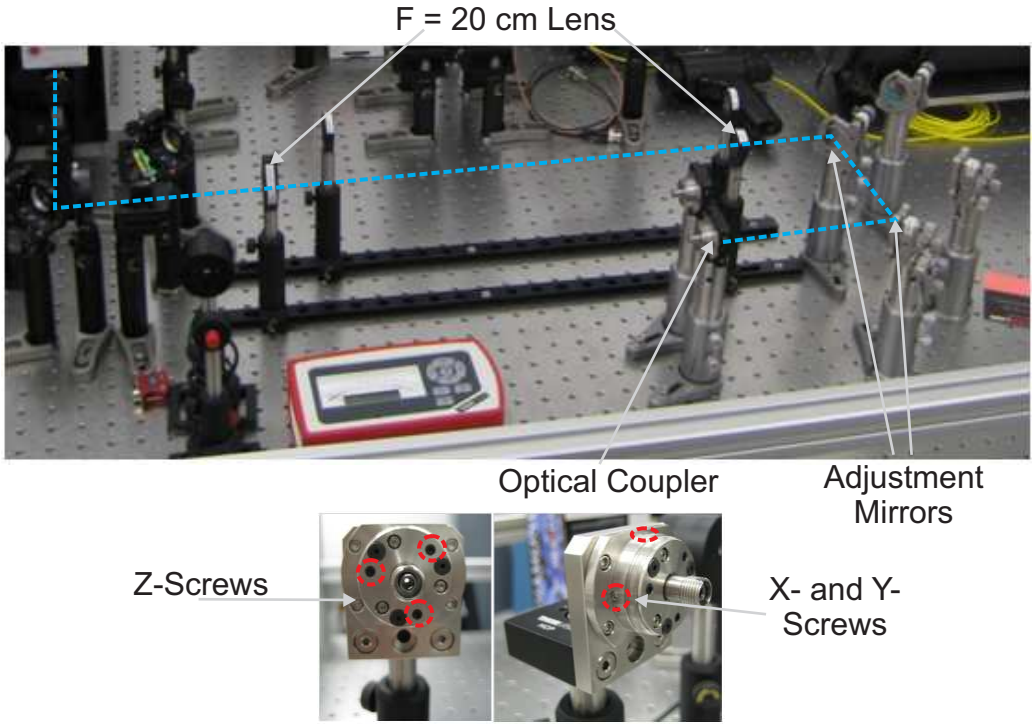

Figure 3.23: Photographs of the optical telescoping system (above) and fiber couplers (below).

positions of the X and Y screws a process of iterative adjustment, so-called walking, of the tuning mirrors followed by adjusting the Z-screws of the fiber coupler was done to maximize the transmission. The Z-screws of the fiber coupler were used to adjust the translation of the lens so that the laser-spot size illuminating the optical fiber core was optimized. The screws were moved in or out by about 1/16 of a full rotation, and the tuning mirrors were walked to

maximize the transmission. The screws were systematically adjusted until maximum laser light transmission was achieved. Typical optical fiber transmission was found to be 20% to 40% for UV/Vis (PM-350-HP, PM-405-HP, and LMA-PM-5) and 60% to 80% for Vis/NIR wavelengths (PM-605-HP and LMA-PM-5).

3.7 Co-propagation of beams

The output laser light from the optical fibers was collimated using a telescoping system on the optical breadboard next to the electrostatic bending elements of the CLS beam line. Two mirrors after the fiber output coupler were used to tune the laser light through the telescope lenses, and two mirrors after the telescoping system were utilized to tune the laser light along the CLS beam line. A photograph of the optical breadboard is shown in Figure 3.24.

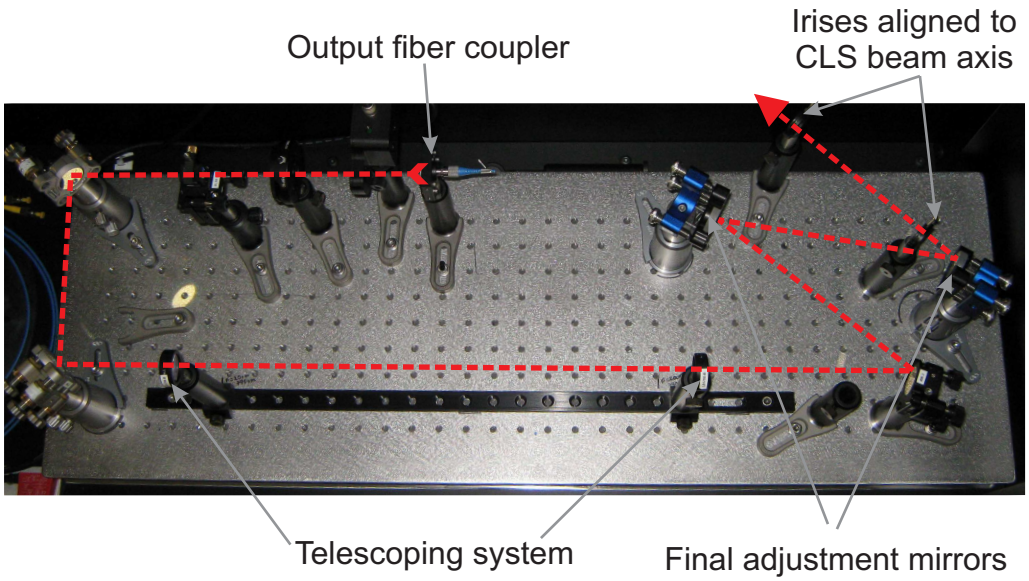

Figure 3.24: Photograph of the optical breadboard placed next to the CLS beam line. Propagation of laser light is shown with the red dashed line.

Optimum overlap of the ion/atom and laser beams was critical for maximizing atomic interactions and enhancing the fluorescent light signal. Alignment of the laser and ion/atom

beams relied on the aperture systems in each BOB. The ion beam was tuned by optimizing the transmission through apertures by adjusting the ion optical components following the process described in 3.5.4. With no apertures in the beam path, the ion beam transport from the first BOB to the second BOB was optimized by iterating the tuning process. The 5 mm apertures in the BOBs were then inserted into the beam path and the ion beam tuning process was repeated again to maximize the current at the Faraday cup at both BOBs. The nominal transmission between the BOBs ranged from 50% to 80% depending on the emittance of the ion beam.

Alignment of the laser light with the ion/atom beam was achieved by adjusting the positions of the two final adjustment mirrors located on the optical breadboard before the laser-light entry window into the CLS vacuum chamber (the optical window on the CLS beam line is not shown in Figure 3.24). The laser beam profile was adjusted using a telescoping system such that the light remained parallel over the 5 meter path through the CLS beam line. The diameter of the collimated laser light through the beam line was typically 2-3 mm. Initial laser light alignment was done by passing the light through two irises that were aligned to the ion/atom beam axis using the beam line alignment telescope. The irises were placed downstream of the two adjustment mirrors on the optical breadboard. After the rough alignment through the irises, the laser light transmission from the entrance to the exit vacuum chamber windows was maximized by maximizing the laser power at the exit with no apertures in the BOBs, where the only adjustment was by repositioning the two adjustment mirrors. The 5-mm apertures were then inserted into each BOB and the same tuning process was repeated. The typical laser light transmission from the entrance to exit windows with 5-mm apertures in place ranged from 85% to 100%.

Some final adjustments to the ion beam optics were made during initial resonance scans. Optimum overlap of the ion/atom and laser beams was achieved by tweaking the deflection of the ion beam after setting the kinetic energy of the ion/atom beam on resonance with a hyperfine transition. The steerer electrodes in the first BOB were then adjusted to maximize the fluorescence signal from the PMT. Although this additional tuning changed the ion beam transmission between the first and second BOBs, the slight steering of the ion beam seems to have resulted in an optimum resonance signal.

Chapter 4

Ion Source Development Results

Results from the ion source development are presented in this chapter. A commerical Colutron plasma ion source was implemented and used to produce ion beams of Ca^+, K^+, and Mn^+. An electron ionization source used to produce metal ions from volatile organometallic compounds was developed and was found to be reliable for producing a stable ion beams of Mn^+ and Fe^+ from metallocene compounds.

4.1 Plasma ion source results

The Colutron plasma ion source was implemented first and used to produce ion beams from varied solid charges. The solid charges were packed into the ceramic charge holder described in Section 3.2. The charge holder was positioned in either the pushrod or oven configuration. The operating conditions of the plasma source to generate ion beams of Ca^+, K^+, and Mn^+ are described below. Unsuccesful attempts to produce other metal beams are briefly discussed as well.

The ion beams produced from the plasma source were unambiguously identified via CLS, but the purity of the ion/atom beam current was not determined, only the total current was measured including contaminent ions. Operating conditions specified below were the typical conditions that resulted in a CLS signal.

4.1.1 Production of Ca^+

A singly-charged calcium beam was produced using metallic calcium powder (Alfa Aesar #42917 granules, redistilled, -16 mesh 99.5%). The calcium charge was packed inside a ceramic charge-holder tube, and the plasma ion source was operated as described in Section 3.2. When the voltage applied to the filament exceeded 6 V, a Ca^+ beam could be extracted. A fluorescence signal was obtained with an ion beam current < 10 pA at the first BOB, where the measured ion beam current was limited by the Faraday cup sensitivity. Stable ion beam currents up to 10s of nA were achieved. The metallic calcium charge in the Colutron ion source provided 40 to 70 hours of Ca^+ beam at a sustained level of 100s of pA.

The use of He buffer gas to stabilize the plasma was studied; there was no significant increase in the extracted ion beam current when the buffer gas was present. Other solid charges to produce Ca^+ were investigated and included calcium bromide (Alfa Aesar #87893, anhydrous, 99.5%) and calcium chloride. A Ca^+ beam could be produced with both solid salt charges, but the beam intensity and charge lifetime were about 10 times lower compared to that obtained with the metallic Ca charge.

4.1.2 Production of K^+

A reliable K^+ beam was produced using a solid potassium iodide charge (Alpha Aesar #87627 99.99%). The KI charge provided 20-40 hours of K^+ beam at 1-3 nA of ion beam current. A fluorescent signal from neutral K was detected when the neutralized beam current was 0.5-1 nA. The photon detection system was configured to detect Vis/NIR light from neutral K (see Refs [53, 63]). The Vis/NIR photon detection system configuration was not used for the CLS of Mn I or Fe I, and is not discussed here; however, the Vis/NIR

configuration was ∼3 times less efficient in detecting fluorescence in the Vis/NIR wavelength range compared to the UV/Vis configuration used to detect fluorescence from Ca II in the UV/Vis wavelength range [53].

4.1.3 Production of Mn^+

A manganese ion beam was produced using a metallic manganese charge (Strem Chemicals #25-0100, powder, 99+%). A fluorescent signal was detected when 100s of nA of ion beam was produced and transported through the beam line. A filament voltage in the range of 10 to 12 V was necessary to produce this ion beam intensity. Both the pushrod and oven configurations of the plasma ion source were investigated, and both configurations offered a similar lifetime and ion-beam intensity with the Mn solid charge. The charge lasted 8 to 16 hours with maximum ion beam currents of 100 to 3500 nA. Stabilizing the beam current during a single scan of the HFS of about 5 minutes was difficult due to the high operating temperature. Adjustment of the filament voltage and/or the pushrod location were necessary every 10 to 15 minutes to extract the Mn^+ beam, due mainly to the quick consumption of the charge.

4.1.4 Other elements investigated

The production of Sc^+ from the plasma source was attempted. Scandium powder (ESPI Metals #knd1178, -40 mesh, 99.9%) was used in both the pushrod and oven configurations of the plasma source. The filament and oven were increased to their maximum values of 16 V and 12 V, respectively. A 100 nA ion beam current was measured at the first BOB during operation of this source. After operation of the source with the Sc charge, it was observed

that the ceramic charge holder was empty; however, a fluorescent signal was not detected. For the given sensitivity of the photon detection system, a fluorescence signal should have been detected if more than 0.1% of the 100 nA of extracted ion beam was Sc^+.

The production of In^+ was attempted using metallic indium in the pushrod configuration. Both helium and argon were used as support gases, but a stable ion beam current could not be achieved. A unstable beam current of up to 50 nA was extracted at a filament setting of 9 V, but the beam current did not stabilize regardless of the filament, anode, or gas flow conditions.

The use of a metallic Fe charge was also investigated as a means to produce Fe^+. A metallic Fe charge was installed in the pushrod configuration, and the filament was increased to its maximum valve of 16 V. An ion beam current of 10s of nA was measured at the first BOB, but no fluorescent signal was detected.

4.2 Electron ionization source and MIVOC chamber development results

Commissioning tests of the EI source are detailed below. Production of beams of Fe^+ and Mn^+ using volatile compounds as charges in a MIVOC chamber, and subsequent ionization using the EI source, are described.

4.2.1 Electron ionization filament power variation

The electron emission current measured on the anode grid was investigated as a function of the input power applied to various filament materials. The filaments utilized were a 0.25 mm

diameter thoria-coated iridium wire from a residual gas analyzer ionizer from Stanford Research Systems, a 0.125 mm diameter thoriated tungsten filament purchased from Electron Tube Store, and a 0.4 mm diameter tungsten filament procured from Scientific Instrument Services. The filament geometry was a half-circle around the anode grid, compared to the full-circle geometry presented in Figure 3.3. The thoria-coated iridium filament had been operated for ∼100 hours before the emission current measurements dicussed here, whereas the other two filaments were not used before this test. The repeller cage was not used during the emission current measurements, and the bias voltages of the filament and extraction plate were fixed at -125 V and -150 V, respectively. It should be noted that the reported electron current was the effective electron emission current, since the measured quantity was the total leakage current from the anode grid, and was not directly equal to the electron emission current from the filament but proportional. The "effective" emission currents obtained for the thoria-coated iridium and thoriated tungsten filaments are presented in Figure 4.1 as a function of the input power. The typical operating regime for the electron ionization source was 5 mA of electron emission current, which was achieved with the lowest input power with the thoria-coated iridium filament. Stable operation of the source at 5 mA emission current was also achieved using the thoriated tungsten filament. An electron emission current was also obtained with the bare tungsten filament, but a power of 75 W was necessary to achieve 5 mA of emission current. The ion source assembly developed an electrical short from the filament to the ground potential at the vacuum system electrical feedthrough after 75 W was applied to the tungsten filament. Both the thoria-coated iridium and thoriated tungsten provided the needed filament performance. The thoria-coated iridium filament was more expensive, $250 per filament, compared to the thoriated tungsten, which was $100 for a 3 m long coil.

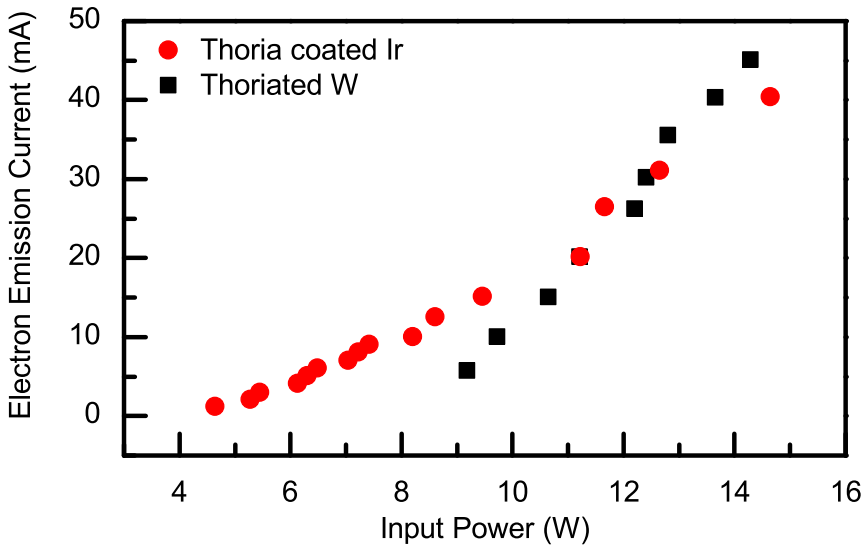

Figure 4.1: Electron emission current for the thoria coated Ir filament and the thoriated W filament as a function of input power.

4.2.2 Electron ionization extraction plate hole size variation

The fraction of positive ions extracted from the electron ionization source through the extraction hole in the extraction plate was studied as a function of the hole diameter. Ions generated inside the anode grid were attracted toward the extraction plate, which was biased at -150 V. Some fraction of the ions hit the extraction plate and the remainder of the ions passed through the extraction plate hole and were collected in an aluminum Faraday cup placed 20 mm downstream from the extraction plate. The Faraday cup was biased to -50 V relative to the extraction plate. The current of the extraction plate and Faraday cup were measured for various diameter holes in the extraction plate. The fraction of ions passing through the hole in the extraction plate was calculated with the expression:

$$\%\,\text{Extracted Beam} = \frac{CE_1\, I_1}{CE_1\, I_1 + CE_2\, I_2} \tag{4.1}$$

where I_1 and I_2 were the measured ion currents from the Faraday cup and tungsten extraction plate, respectively. The parameters CE_1 and CE_2 were the secondary-electron conversion efficiencies of the aluminum Faraday cup and tungsten extraction plate, respectively. The percent ion beam extracted from the source for each hole diameter was calculated assuming $CE_1 = CE_2$, and the results are shown in Figure 4.2. The fraction of the beam extracted was found to saturate at a hole diameter of 3 mm. It is noted that if CE_1 is taken to be different than CE_2, the saturation behavior at 3 mm does not change.

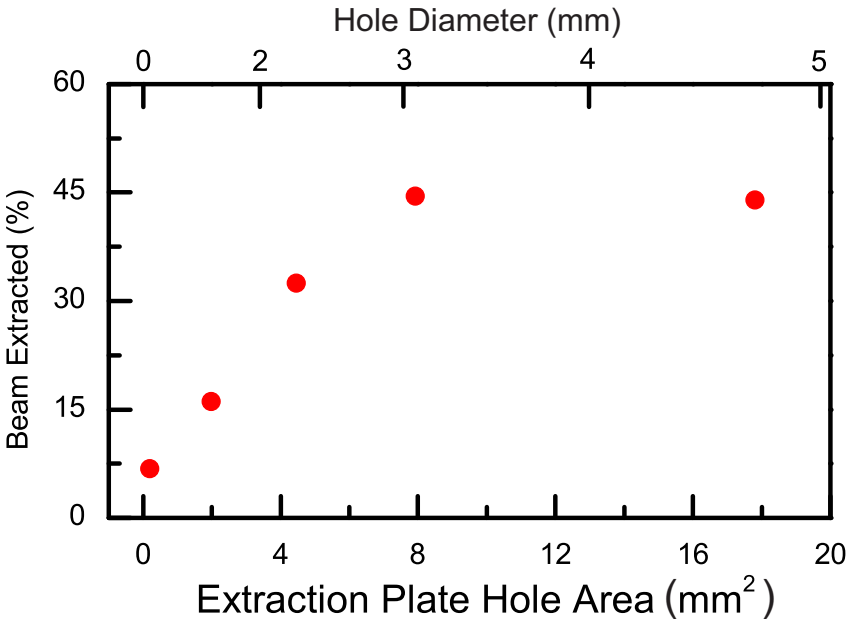

Figure 4.2: The extraction efficiency of the EI source as a function of extraction plate hole area, see the text.

4.2.3 Electron ionization source bias voltage optimization

The effectiveness of biasing the repeller cage was investigated by measuring the effective electron emission current at the anode grid while varying the bias voltage applied to the repeller grid. For these tests, the bias voltages applied to the filament and extraction plate

were held at -125 V and-150 V, respectively. The current applied to the filament was 3.6 A. The results are presented in Figure 4.3.

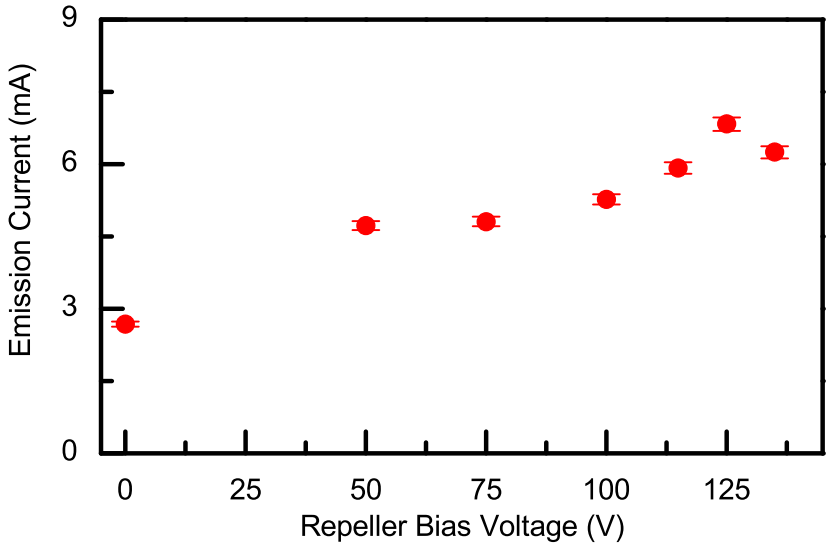

Figure 4.3: Electron emission current measured on the anode grid as a function of repeller grid bias voltage. Here the magnitude of the bias voltage is presented; the actual voltage was negative. The conditions of the measurement are described in the text.

The effective electron emission current was found to increase as a function of repeller cage voltage up to a maximum when the voltage of the repeller cage matched the bias voltage of the filament. The optimum setting of the repeller cage was also investigated by varying the input power applied to the filament with its bias voltages set to 0 V and -125 V. The measured electron emission current is shown in Figure 4.4. The emission current increased with increasing filament power, consistent with the data presented in Figure 4.1. In addition, the effective emission current measured with a -125 V bias applied to the repeller cage was approximately a factor of two larger than the emission current with a 0 V repeller cage bias regardless of the filament current.

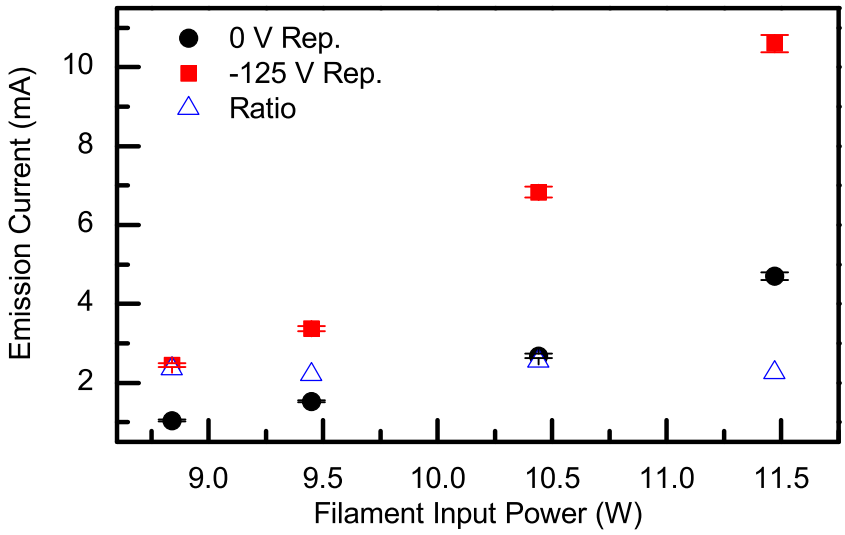

Figure 4.4: Effective electron emission current measured on the anode grid as a function of filament current with and without a bias voltage applied to the repeller cage. The open blue triangles show the ratio of emission currents with and without a bias voltage applied to the repeller cage are all in the range of 2-3.

The intensity of the extracted ion beam current was investigated as a function of incident electron energy. The energy of the electrons inside the anode grid was mostly determined by the filament bias voltage, which was varied between -60 V and -130 V. The measured ion beam current at the first BOB as a function of the electron energy is shown in Figure 4.5. The results show a maximum near 110 V.

Ferrocene was used as a charge in the MIVOC chamber for the electron energy variation. The fraction of the total ion beam current that was $^{56}Fe^{+}$ was also important and may depend on the electron energy. The Fe I resonance signal normalized for counting time, laser power, and neutralization efficiency in the charge-exchange process, is also presented as a function of electron energy in Figure 4.5. The spectroscopy of Fe I is described in detail in Section 5.1. The trend of the ion beam current increased as a function of electron energy to $\sim$ 100 eV, where it became saturated, consistent with the expected behavior of electron

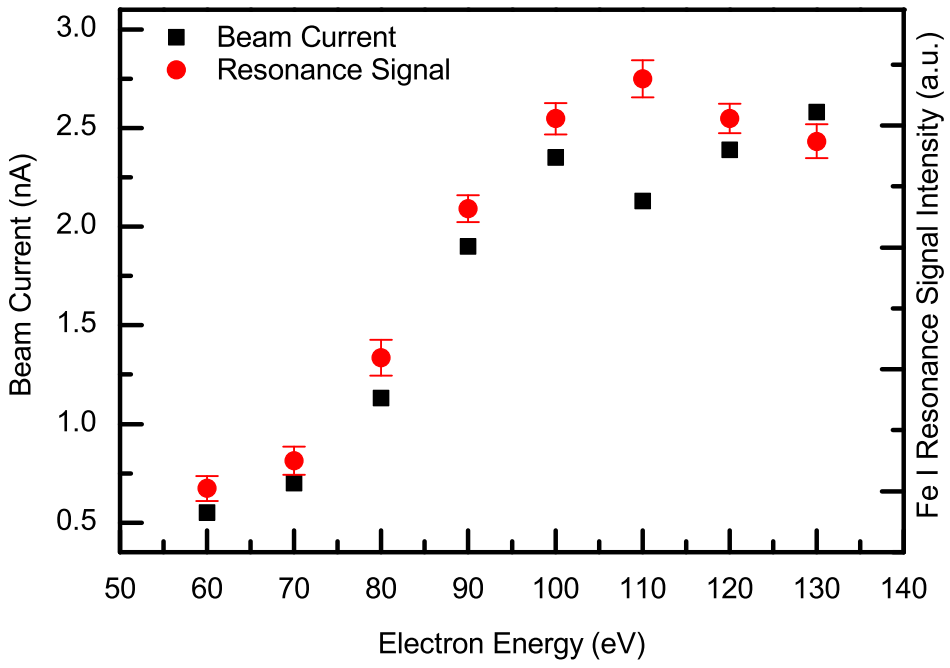

Figure 4.5: The ion beam current measured at the first BOB and normalized Fe I resonance signal as a function of electron energy.

ionization cross sections [31]. The normalized Fe I resonance signal followed the trend of the extracted ion beam, saturating near an electron energy of 100 eV. Therefore, the fraction of $^{56}Fe^{+}$ in the extracted ion beam did not appear to change as a function of electron energy over the energy range investigated. The normalized Fe I resonance signal is displayed in Figure 4.6 as a function of the extracted beam current measured at the first BOB for all EI bias-voltage variations discussed above. The intensity of the normalized resonance signal increased with extracted ion beam current implying the fraction of $^{56}Fe^{+}$ in the extracted ion beam was not sensitive to variation of bias voltages applied to the EI source components.

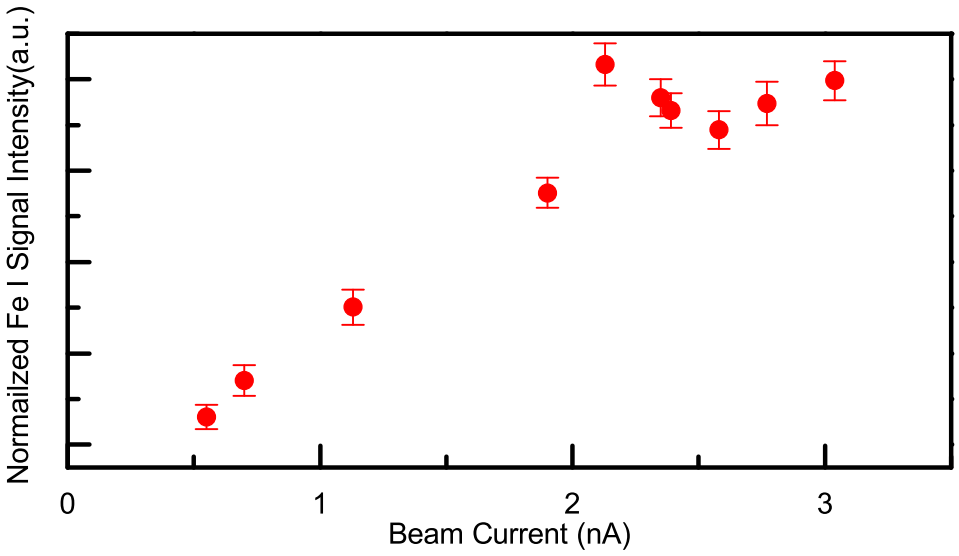

Figure 4.6: The Fe I resonance signal intensity as a function of ion beam current extracted from the EI source for all bias voltage variations investigated.

4.2.4 Speciation of MIVOC charges in the electron ionization process

The molecular distribution of the sublimated organometallic molecules when the MIVOC chamber was connected to the EI source was investigated with a Stanford Research Systems Residual Gas Analyzer (RGA300). The RGA contained an electron ionizer and quadrupole mass filter; residual gas molecules were ionized via collisions with 80 eV electrons, and were analyzed in the mass filter. The RGA was attached to the high vacuum system, opposite the MIVOC chamber leak valve. A pressure of $< 10^{-6}$ Torr was achieved in the beam line on which the RGA was mounted. The MIVOC chamber was evacuated to a pressure between $10^{-4} - 10^{-3}$ Torr. RGA mass spectra were collected with the leak valve closed and open for two organometallic charges; ferrocene (Aldrich F408-5G, 98%) and iron (III) aceylacetonate (Aldrich 517003-10G, >99.9%).

A representative RGA mass spectrum obtained with ferrocene is shown in the top panel of Figure 4.7. The bottom panel of Figure 4.7 is the baseline measurement obtained from the background gas in the high-vacuum chamber when the leak valve separating the MIVOC chamber and RGA was closed. There are a number of peaks in the ferrocene mass spectrum, and the experimental spectrum was compared with the reference electron ionization mass spectrum in Figure 2.2 to identify the components of the spectrum associated with ferrocene. Other lines in the mass spectrum were attributed to hydrogen ($M/Q = 2$), water vapor (18), and nitrogen (28), all of which were the dominant species in the baseline RGA spectrum (leak valve closed). An increase in the nitrogen peak intensity was observed when the leak valve was opened, indicative of residual atmospheric gas inside of the MIVOC chamber. The amount of $^{56}Fe^{+}$ was quantified by integrating the area under the $M/Q = 56$ line in

the spectrum relative to all fragments associated with ferrocene, and all fragments in the spectrum. The percentage of the $^{56}Fe^{+}$ fragment relative to all peaks attributed to ferrocene was found to be 25%. The overall fraction of $^{56}Fe^{+}$ in the total RGA spectrum was 13%. The present EI source was modeled after the RGA ionizer, thus the speciation of compounds in the EI source was assumed to be similar to that observed with the RGA.

The same RGA measurements were repeated for iron (III) acetylacetonate ($Fe(acac)_3$). An attempt to reduce the background signal was made by pumping the MIVOC chamber to $< 10^{-5}$ Torr. The RGA was mounted directly on the MIVOC chamber, and a mass spectrum was recorded with the $Fe(acac)_3$ installed in the MIVOC chamber; the spectrum is shown by the solid line in Figure 4.8. The lower panel is a baseline spectrum recorded with no charge installed in the MIVOC chamber. The relative intensity of the baseline spectrum is $\sim$5 times higher than that of the $Fe(acac)_3$ spectrum. The intensity difference is mostly due to the pumping time before each spectrum was aquired; the baseline spectrum was obtained after two hours of pumping with no charge in the chamber, and the $Fe(acac)_3$ spectrum was taken after 12 hours of pumping with the charge in the chamber. The 12 hours of pumping were required to achieve the desired $< 10^{-5}$ Torr pressure. The lines attributed to $Fe(acac)_3$ had small intensities, even after 12 hours of vacuum pumping time to remove residual atmospheric gases, as highlighted in the insets of Figure 4.8. The $Fe(acac)_3$ spectrum was compared to the spectrum given by Ref [1] to determine the M/Q lines associated with $Fe(acac)_3$. The molecular weight of $Fe(acac)_3$ is 353.17 amu, and the RGA300 can only measure M/Q<300. Thus, the molecular ion of $Fe(acac)_3$ and fragments with M/Q>300 were not observed. Therefore, only an upper bound on the fraction of $^{56}Fe^{+}$ in the observed $Fe(acac)_3$ fragments could be determined, and was deduced to be $< 3\%$. The overall fraction of $^{56}Fe^{+}$ in the entire RGA spectrum was less than 0.2%.

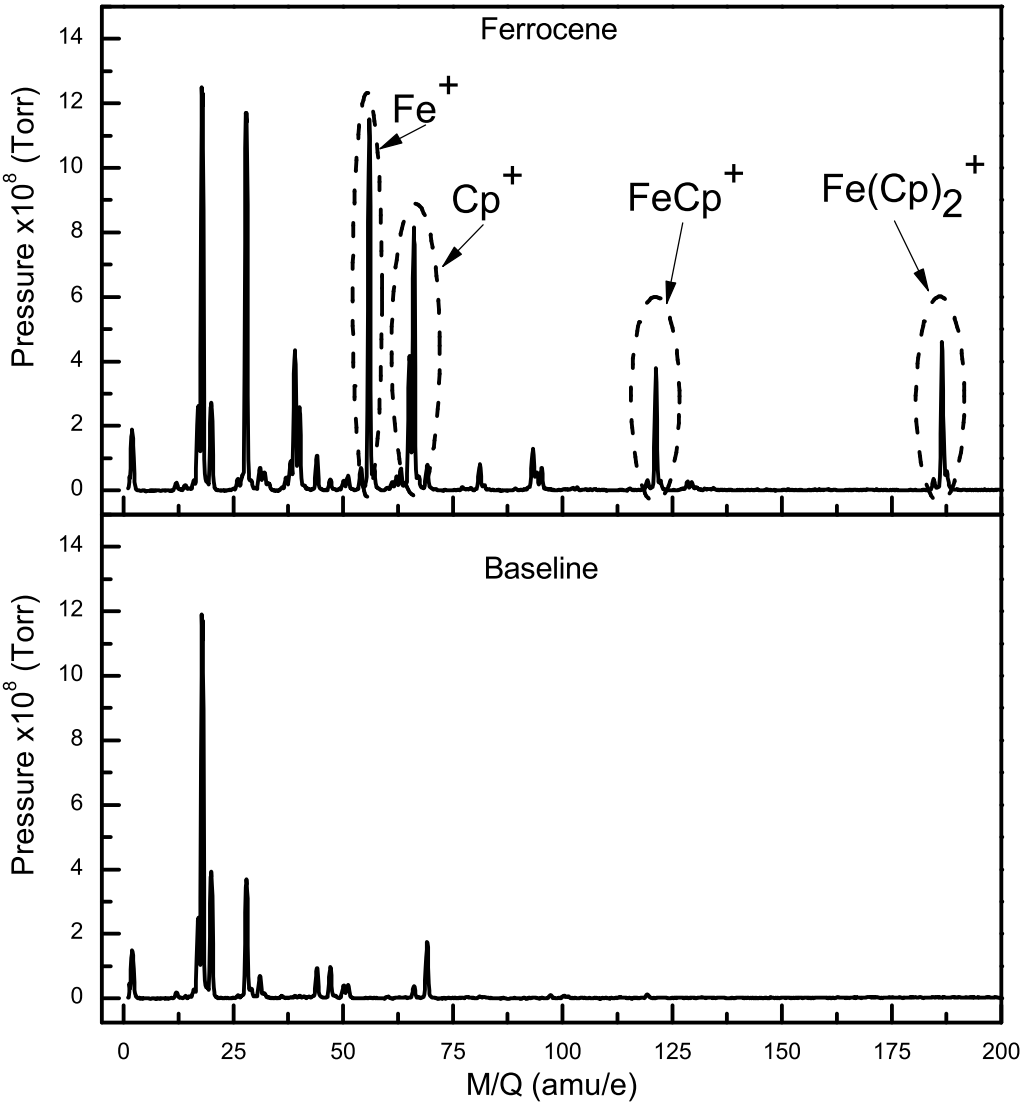

Figure 4.7: Ferrocene RGA results. The top panel represents the ferrocene spectrum, and the bottom panel is the baseline spectrum. Lines attributed to ferrocene are indicated with dashed ovals

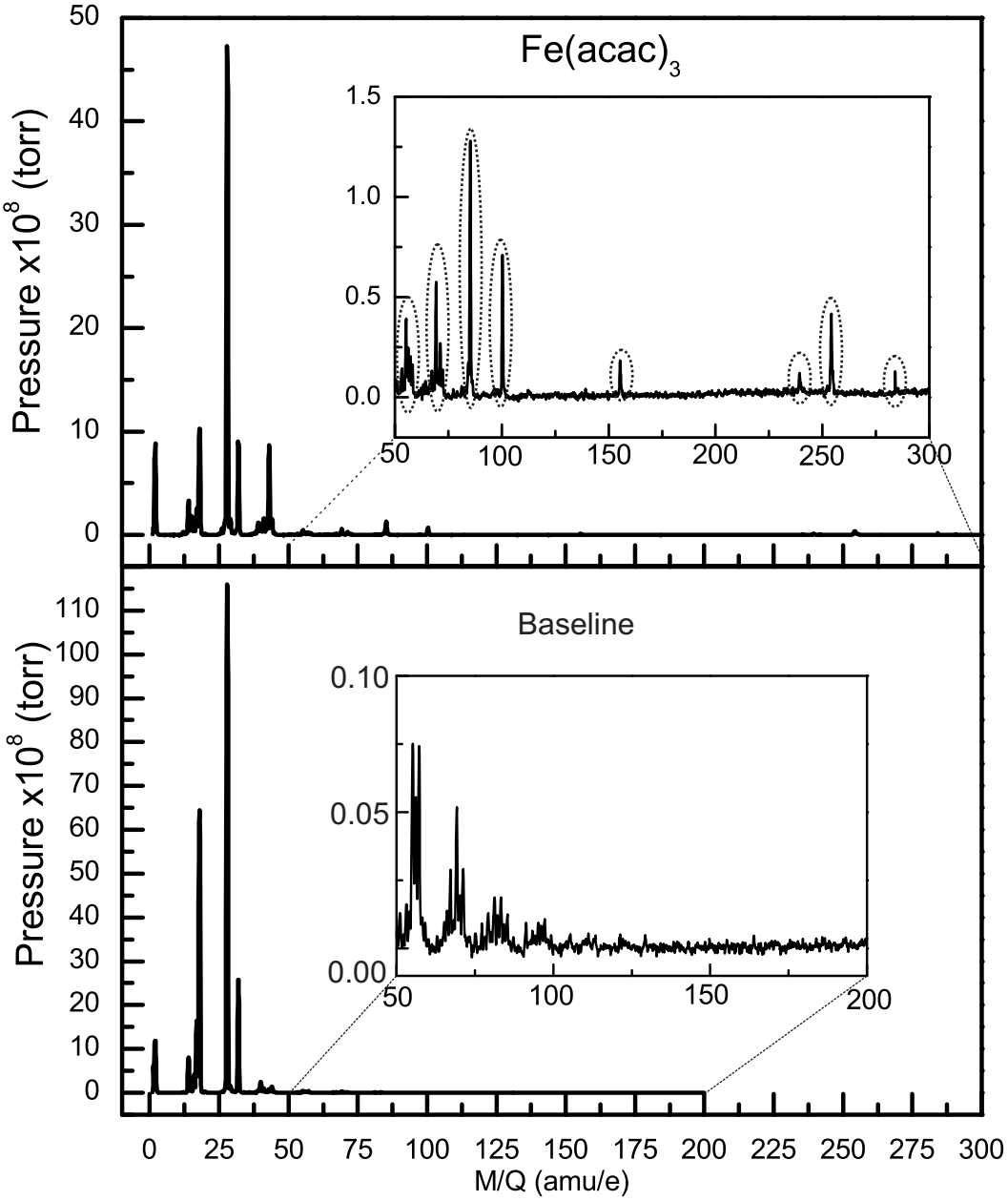

Figure 4.8: Iron (III) acetylacetonate RGA mass spectrum. The top panel represents the $Fe(acac)_3$ spectrum, and the bottom panel is the baseline spectrum. Lines attributed to $Fe(acac)_3$ are indicated with dashed ovals.

4.3 Metal ion beams from EI + MIVOC setup

4.3.1 Production of Fe^+

Singly-charged ^{56}Fe ions were produced in the EI source by fragmenting ferrocene vapor that was introduced into the source from the MIVOC chamber. The ferrocene charge, about 0.5 g, was placed in the MIVOC chamber, and the chamber was evacuated to a pressure of $\sim 10^{-3}$ Torr. The ferrocene vapor was introduced into the EI source by fully opening the leak valve separating the two vacuum chambers. The maximum throughput of the fully open leak valve was specified by the manufacturer to be 50 liters per minute with a pressure of 760 Torr at the inlet of the valve. It should be noted that the leak valve was fully open for all MIVOC + EI configurations; therefore the relative flow rate of the vapor from the MIVOC chamber was determined by the pressure in the MIVOC chamber (e.g., the vapor pressure of the metal-containing compound). An ion beam of $^{56}Fe^+$ was produced when the ferrocene charge was at room temperature (e.g. 293 K). One ferrocene charge was used for 40 hours over 5 days and performance of the MIVOC system and EI source was stable with a typical ion beam current intensity of 1-10 nA.

A iron (III) aceylacetonate charge was placed into the MIVOC chamber and leaked into the EI source chamber after the MIVOC chamber was evacuated. The MIVOC chamber was heated to 373 K, but no evidence of $^{56}Fe^+$ production was found in the CLS studies.

Using ferric chloride ($FeCl_3$) to produce Fe^+ was also investigated. Although $FeCl_3$ is not an organometallic compound, it has a vapor pressure of 3×10^{-3} Torr at 381 K [73]. The $FeCl_3$ (0.5 g) was placed in the MIVOC chamber, the chamber was evacuated, and the leak value was opened to introduce the $FeCl_3$ vapor into the ion source. Resonance peaks in

CLS measurements of ^{56}Fe I were recorded when the temperature of the MIVOC chamber and charge holder were heated above 318 K.

4.3.2 Production of Mn^+

Singly-charged ^{55}Mn ions were produced by fragmenting manganocene vapor in the EI source. The manganocene charge (Strem Chemicals 25-0200, >98%) of about 0.5 g was placed in the MIVOC chamber, and the chamber was pumped to a pressure of $\sim 10^{-3}$ Torr. The manganocene vapor was introduced into the EI source by opening the leak valve separating the MIVOC and EI chambers. A beam of $^{55}Mn^+$ was produced when the MIVOC chamber was heated above 319 K.

The production of $^{55}Mn^+$ by the EI source was quantified via CLS and studied as a function of the manganocene charge temperature between 298 K to 373 K. The amount of $^{55}Mn^+$, which was extracted from the normalized resonance peak area of a cyclic transition in the hyperfine spectrum of neutral ^{55}Mn, is given as a function of charge temperature in Figure 4.9. Details on CLS measurements of ^{55}Mn I are given in Chapter 5.

The peak area of the cyclic transition was normalized for counting time, laser power and $^{55}Mn^+$ neutralization efficiency in the charge-exchange process. The temperature of the MIVOC chamber was measured using a thermocouple attached directly to the MIVOC charge-holding dish. The MIVOC vacuum chamber and the transfer line between the MIVOC and EI source chambers were wrapped with heating tape and maintained at a temperature of 365 K. It was not possible to keep the entire vacuum chamber/transfer line at temperatures above 365 K, since the leak valve was only rated to operate at temperatures below 373 K. At temperatures below 365 K, the amount of manganocene vapor transferred from the MIVOC chamber to the EI chamber was thought to be directly related to the saturated

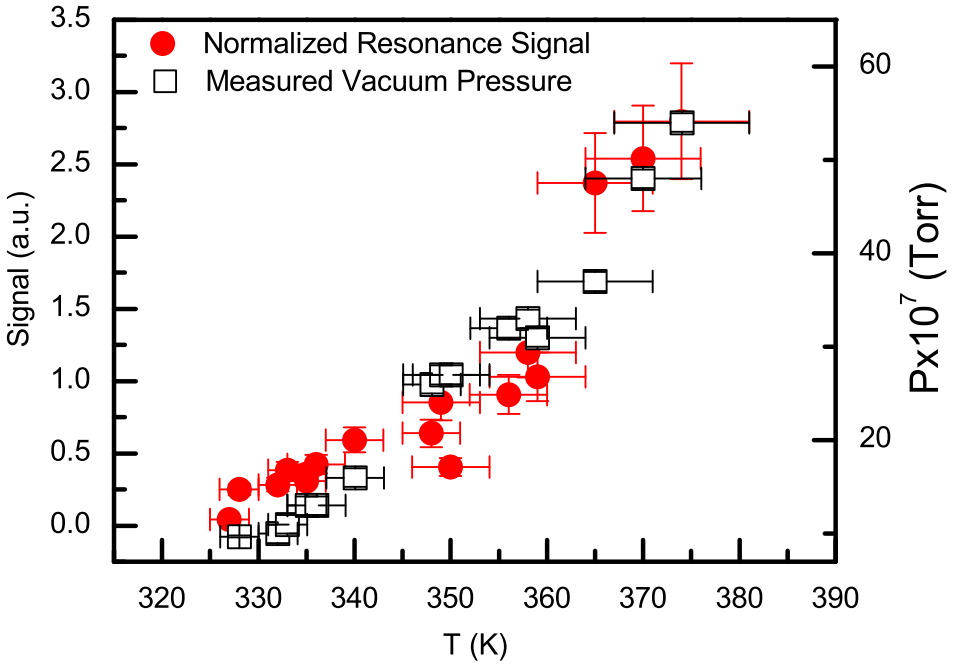

Figure 4.9: ^{55}Mn I resonance signal and measured ion source vacuum pressure as a function of manganocene charge temperature.

manganocene vapor pressure at the measured temperature of the MIVOC charge-holder. At charge holder temperatures above 365 K the temperature which defined the saturated vapor pressure may have been determined by the the lowest temperature of the transfer line. The temperatures deduced for the charge above 365 K reflect the uncertainty in measurement of the temperature that defined the saturated vapor pressure.

The pressure in the EI source chamber was found to increase with an increase in the MIVOC charge temperature. The pressure measured 2 m downstream of the EI source is presented as a function of charge temperature in Figure 4.9. The intensity of Mn^+ extracted from the ion source, determined by the normalized Mn I resonance signal, should be directly proportional to the amount, and hence pressure of manganocene in the EI chamber. The normalized ^{55}Mn I resonance signal is given as a function of MIVOC charge temperature in Figure 4.9. The amount of $^{55}Mn^+$ extracted from the EI source and the measured pressure behave similarily as a function of MIVOC charge temperature. The temperature and vapor pressure of the MIVOC material are related through the Clausius-Clapeyron relation, Eqn 2.4. The natural log of the ^{55}Mn I resonance signal is given as a function of 1/T in Figure 4.10. The appartent heat of sublimation of ΔH_{sub} of (79 ± 9) kJ/mol for manganocene was deduced from the slope of a linear fit to the data in Figure 4.10 and is in good agreement with the literature value of (75.7±1.7) kJ/mol [74]. The natural log of the change in the pressure in the two-way bending element was also examined as a function of the charge temperature. The baseline pressure measurement may be subtracted from the total pressure, but the "baseline" pressure was ambiguous. Three cases for the baseline pressure were considered: one was no baseline, the second case was the using the measured pressure before the ion source was turned on (2.2×10^{-7} Torr), and the third when the resonance signal was first observed (6.5×10^{-7} Torr). The ΔP versus 1/T plot for each baseline

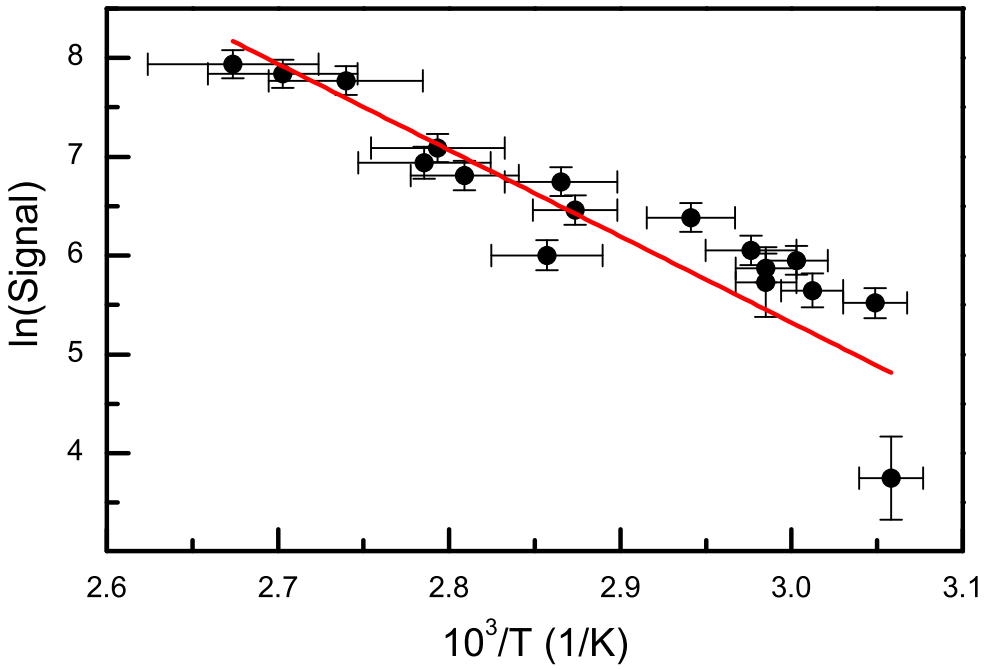

Figure 4.10: Natural log of the ^{55}Mn I normalized resonance signal given as a function of the inverse of the manganocene charge temperature. The signal is representative of the amount, and hence pressure of manganocene, see the text.

condition is presented in Figure 4.11. Linear functions were fitted to each data set, and

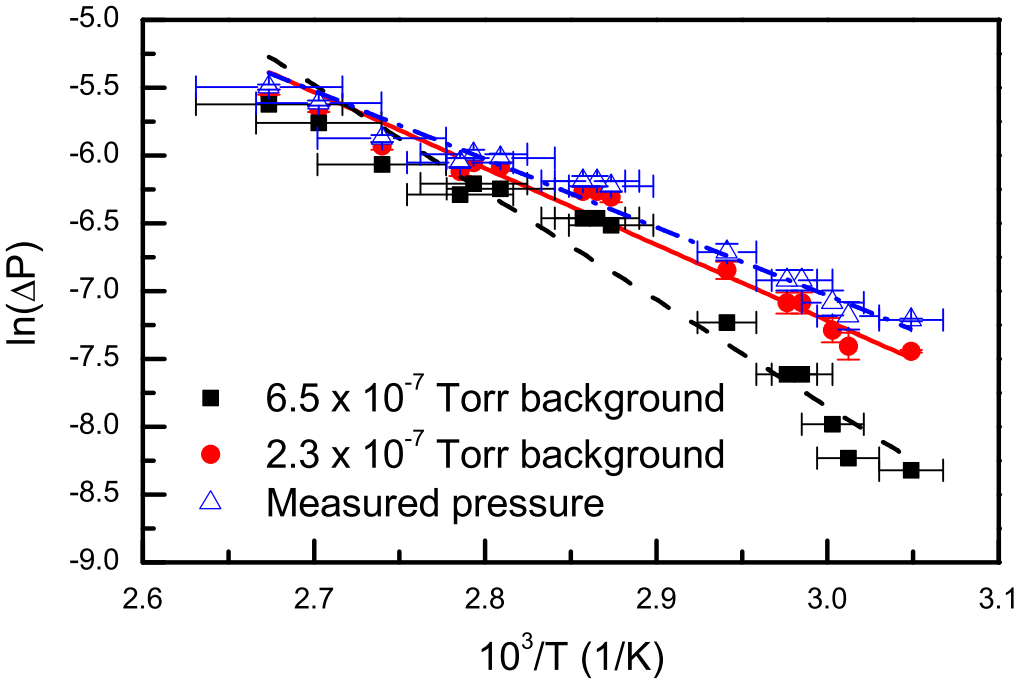

Figure 4.11: Clausius-Clapeyron plot of the measured ion source vacuum pressure and manganocene charge temperature.

an averaged value of $\Delta H_{\text{sub}} = 56 \pm 12$ kJ/mol was deduced for all these data sets. The uncertainty given in the extracted ΔH_{sub} includes the systematic error associated with the baseline pressure. The ΔH_{sub} deduced from the data in Figure 4.11 did not agree with the literature ΔH_{sub} of manganocene. The source of the discrepancy is likely that the increase in pressure can be attributed to a variety of species being released from the EI source, not exclusively manganocene. The percent of the total EI source vacuum chamber pressure that was a manganocene component was estimated by comparing the extracted ΔH_{sub}, called $\Delta H_{\text{sub}}^{\text{exp}}$, from the data in Figure 4.11 and the literature value, $\Delta H_{\text{sub}}^{\text{lit}}$ for manganocene. The relations

$$\ln(P_{\text{tot}}) = \frac{-\Delta H_{\text{sub}}^{\text{exp}}}{R}\frac{1}{T} + C_1 \tag{4.2}$$

and

$$\ln(P_{\text{Manganocene}}) = \frac{-\Delta H_{\text{sub}}^{\text{lit}}}{R}\frac{1}{T} + C_2, \tag{4.3}$$

were re-arranged and expressed in terms of 1/T. Upon dividing of Eqn 4.2 by Eqn 4.3:

$$\ln(P_{\text{tot}}) = \frac{\Delta H_{\text{sub}}^{\text{exp}}}{\Delta H_{\text{sub}}^{\text{lit}}} \ln(P_{\text{Manganocene}}) + C_3, \tag{4.4}$$

where

$$C_3 = C_1 - C_2\frac{\Delta H_{\text{sub}}^{\text{exp}}}{\Delta H_{\text{sub}}^{\text{lit}}}. \tag{4.5}$$

The total pressure was then expressed as a function of the vapor pressure of manganocene

$$P_{\text{tot}} = \exp[C_3] \times P_{\text{Manganocene}}^{1.35}. \tag{4.6}$$

The percent manganocene vapor in P_{tot} was determined as function of temperature, assuming $\exp[C_3] = 1$. The result is given in Figure 4.12. The lower limit of the temperature for introducting manganocene into the EI source vacuum chamber was deduced by extrapolating to zero percent manganocene with the linear regression line. The extracted manganocene lower-limit temperature was found to be (315±7) K, which agreed with the lower limit of 319 K obtained from CLS studies when using manganocene as the MIVOC charge. The uncertainty reported in the manganocene lower-limit temperature from the above analysis includes systematic errors from the baseline pressure measurement and a variation of the value of $\exp[C_3]$ from 0.1 to 10.

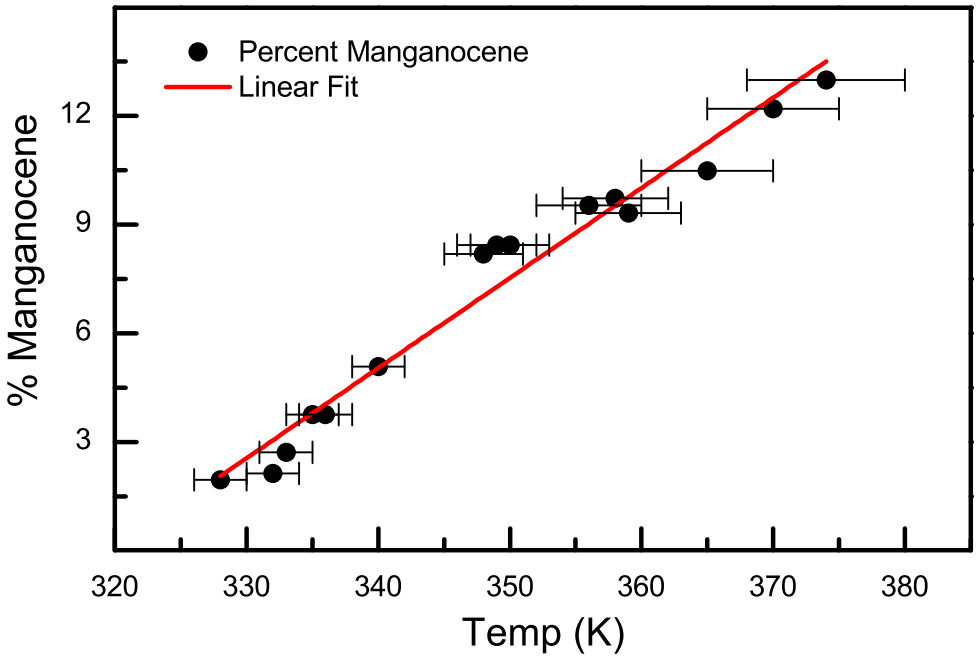

Figure 4.12: Percent manganocene as a function of the manganocene charge temperature extracted from the variation of the overall pressure, see the text.

Table 4.1: Summary of ion beams extracted from the plasma and EI sources.

Source	Ion Beam	Charge	Lifetime (hr)	Intensity (nA)
plasma	Ca^+	metallic Ca	40-80	0.1
plasma	Ca^+	$CaCl_2$	10-20	0.1
plasma	Ca^+	$CaBr_2$	10-20	0.1
plasma	K^+	KI	20-40	2
plasma	Mn^+	metallic Mn	8-16	100
EI	Fe^+	ferrocene	> 40	5
EI	Fe^+	$FeCl_3$	> 40	5
EI	Mn^+	manganocene	> 40	5

4.4 Summary of developed and extracted ion beams

The extracted ion beams from the plasma and EI sources are summarized in Table 4.1. The charges used to achieve the ion beams, operational lifetime of the charge, and the typical intensity of the total ion beam current measured at the first BOB while using the 5-mm aperature are provided as well. The lifetime for the MIVOC charges listed is something of a lower bound as the charges were not exhausted after operation.

Chapter 5

Collinear Laser Spectroscopy Results

Results from the CLS measurements of ^{56}Fe I and ^{55}Mn I will be presented in this chapter. The HFS recorded for ground state electronic transitions in ^{55}Mn I were consistent with known hyperfine coupling constants, and provided a quality check of the experimental system. Hyperfine coupling constants deduced from the HFS for metastable state transition improved the precision of previously reported values by two orders of magnitude, where available. The metastable state was populated in charge-exchange reactions of Na + Mn^+.

5.1 ^{56}Fe I hyperfine structure measurements

5.1.1 Transition frequency

A 15 keV beam of $^{56}Fe^+$ was extracted from the EI source as described in Section 4.3.1, and CLS was subsequently performed on ^{56}Fe atoms that were neutralized in charge-exchange reactions with a Na vapor. The Na+Fe^+ charge-exchange process and the atomic levels probed via laser spectroscopy are depicted in Figure 5.1. It should be noted that the atomic energy levels referred to in the charge-exchange processes are defined in units of eV, and for the spectroscopy transitions, the level energies are defined in terms of cm^{-1}, consistent with convention. Energy and wavenumber are related through Planck's Law, $E = hc/\lambda$, where E is energy, h is Planck's constant, and λ is the wavelength.

The first ionization potential of Fe is 7.9024 eV and the ionization potential of Na is 5.13908 eV [3]. An energy gain of 2.76332 eV is exptected for a Fe^+ ion from the transfer of an electron from the ground state of Na to the ground state of Fe. The atomic transition in Fe I between the $3d^6(^5D)4s\ ^5D_4$ ground state to the $^5F_5$ state at 26874.548 cm^{-1} was excited using laser light, and the resulting laser-induced fluorescence was measured using the photon detection system. The Einstein coefficient for this transition is $A_{ik} = 1.62 \times 10^7\ s^{-1}$ [75], corresponding to a natural linewidth of 2.58 MHz.

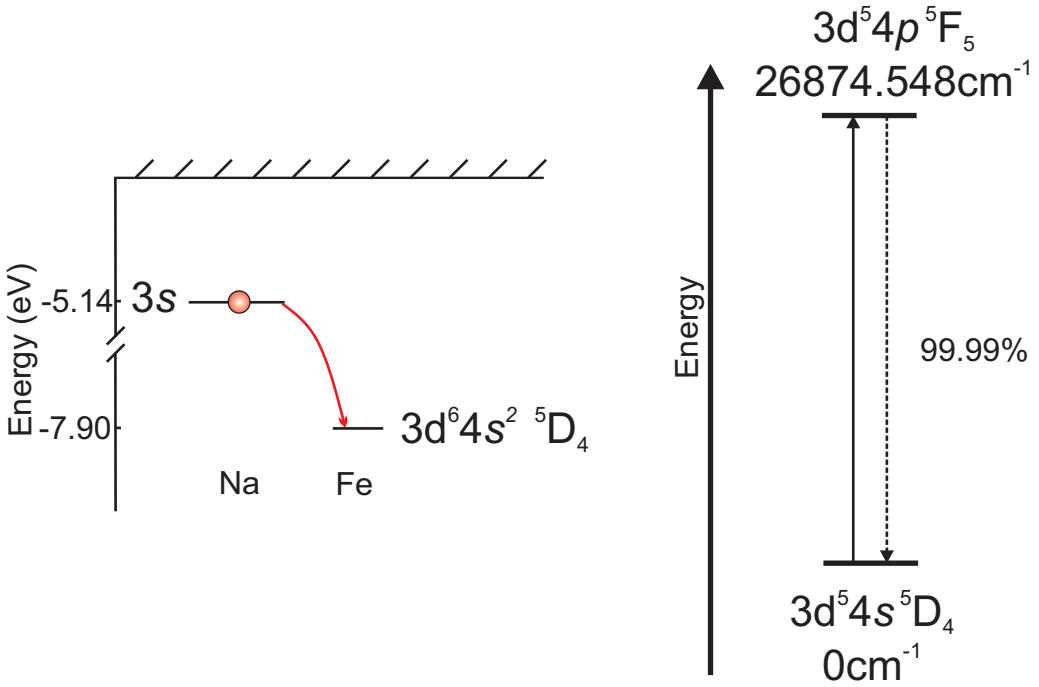

Figure 5.1: The Na-Fe^+ charge-exchange process is depicted on the left, and the Fe I $^5F_5 \rightarrow ^5D_4$ transition probed via laser spectroscopy is shown on the right.

A representative laser-induced fluorescence spectra for the ^{56}Fe I $^5F_5 \rightarrow ^5D_4$ transition is presented in Figure 5.2. The ^{56}Fe nucleus has $I_N = 0$ and thus, there are no hyperfine structure levels. The line shape was fitted with both symmetric and asymmetric Voigt functions, which were described in Section 2.3.5. The reduced chi-squared (χ^2/ν) values from the fitting routine, where ν is the number of degrees of freedom, were found to to be $\chi^2/\nu = 28$,

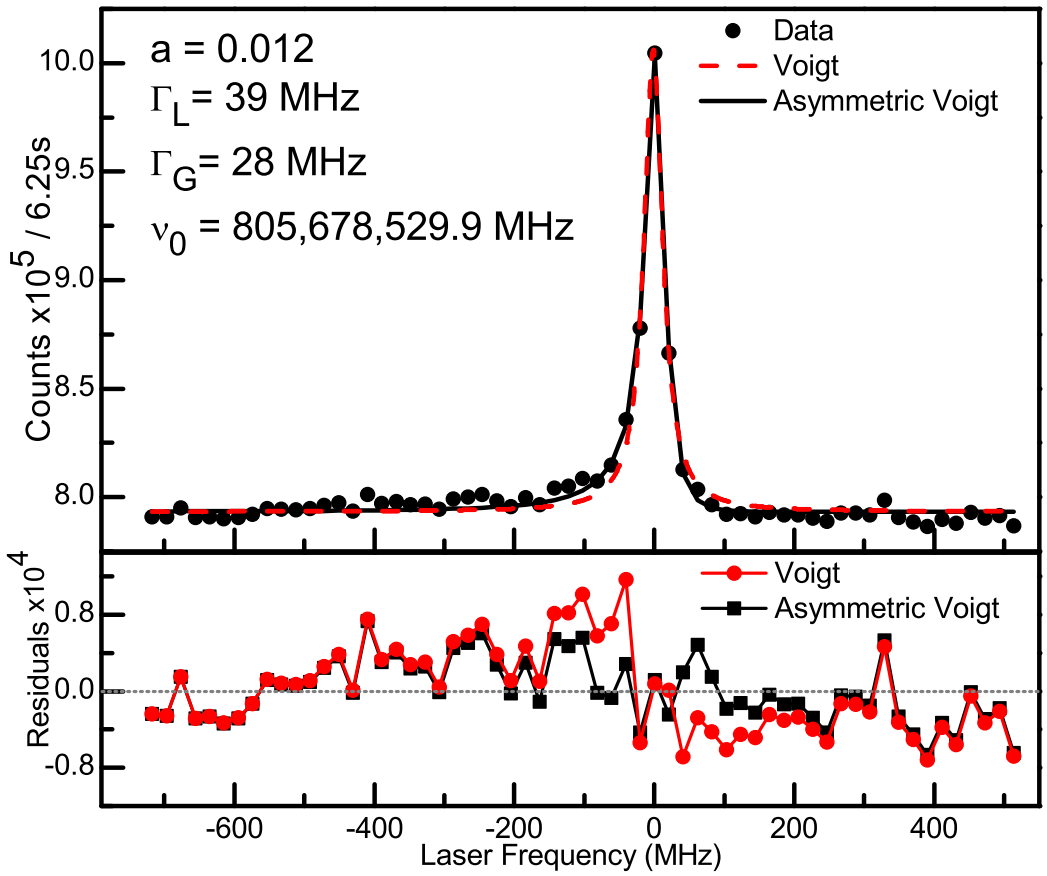

Figure 5.2: An example of an ^{56}Fe I HFS spectrum obtained while using a ferrocene charge in the MIVOC chamber is presented in the upper panel. Residuals from the symmetric and asymmetric Voigt function fits to the data are displayed in the bottom panel.

Table 5.1: The center of gravity frequency of the Fe I $^5F_5 \rightarrow ^5D_4$ transition investigated.

Present ν_c (MHz)	Literature ν_c (MHz)	Ref
$805,678,536.6 \pm (0.1) \pm (21) \pm (300)$	$805,678,680 \pm 30$	[76]

and $\chi^2/\nu = 4.3$ for the fitted symmetric and asymmetric Voigt profiles, respectively. The centroid of the line shape deduced from the symmetric function was found to be shifted from the determined centroid of the asymmetric function by 1.5 MHz. The asymmetric Voigt profile provided a better description of the low-energy tail on the fluorescence peak due to inelastic charge-exchange reactions. The extracted centroid obtained using the asymmetric resonance is presented in Table 5.1, where the reported uncertainty in the centroid value had three contributions. The first contribution was the statistical error from the fitting routine. The systematic error seen in run-to-run variation of the extracted centroid was assigned by taking the standard deviation determined from centroids of 33 data sets and is reported as the second uncertainty in Table 5.1. A ±300 MHz uncertainty from the helium-neon reference laser for the wavelength measurement give a systematic uncertainty in the absolute laser frequency (Section 3.6.2). This systematic error is the third centroid uncertainty presented in Table 5.1. The overall agreement with the literature value is excellent and the uncertainty is dominated by the He-Ne laser reference.

5.1.2 Saturation laser power

The recorded signal height was investigated as a function of the laser power used to excite the transition to determine the effect of laser power broadening. Here, the signal height is defined as the height of the resonance peak above the background. The saturation laser power for the Fe I $^5F_5 \rightarrow ^5D_4$ transition was calculated using Eqn 2.9 to be $P_{\text{sat}} = (610 \pm 250)\ \mu$W,

assuming a (2.5 ± 0.5)-mm diameter laser beam. The signal height, normalized for counting time and beam current, is shown as function of laser power in the top panel of Figure 5.3. The signal to noise ratio, defined as the signal height divided by the square root of the photon background is shown as a function of laser power in the bottom panel of Figure 5.3.

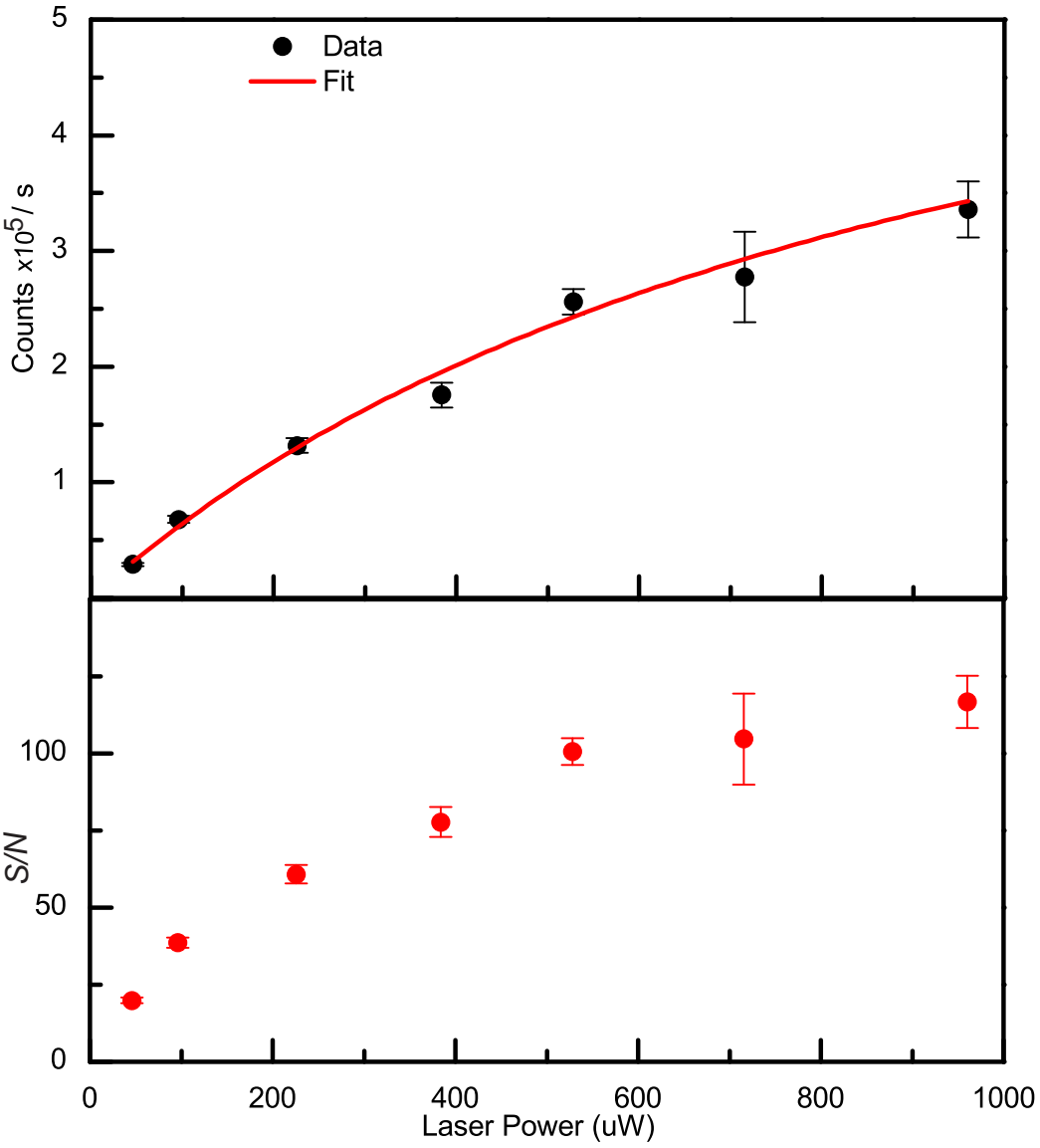

Figure 5.3: The signal height as function of laser power used to excite the Fe I atoms is displayed in the top panel. The signal-to-noise ratio of the Fe I $^5F_5 \rightarrow ^5D_4$ transition with increasing laser power is presented in the lower panel.

The data in the top panel of Figure 5.3 were fitted to the saturation function [46] using a least-squares minimization:

$$\text{Signal} = C \times \frac{\frac{P}{P_{\text{sat}}}}{1 + \frac{P}{P_{\text{sat}}}}, \tag{5.1}$$

where P is the laser power used for the excitation. The fitted parameters C and P_{sat} represent a normalization constant and the saturation laser power, respectively. The function fitted to the data and shown in Figure 5.3 has $P_{\text{sat}} = (976 \pm 210)\mu$W, in general agreement with the calculated value of (610 ± 250) μW. The signal-to-noise ratio of the Fe I resonance peak was found to saturate at a laser power of $\sim$600 μW.

The deduced line width of the Fe I resonance spectra was 60 ± 10 MHz, which is a factor of $\sim$25 larger than $\Gamma_{\text{nat}} = 2.58$ MHz. The line width can be seen to be broadened mostly by energy transfer in the Fe^+ + Na charge-exchange reactions. As noted earlier, the Fe atom gained $\sim$2.7 eV in the charge-exchange reaction with the Na vapor, and the differential Doppler-shift of the ^{56}Fe beam at 15 keV was 20.54 MHz/V. Thus a 2.7 eV kinetic energy broadening corresponds to a 55 MHz broadening of observed line width.

5.1.3 Sensitivity

The sensitivity of fluorescence detection was explored by determining the number of atoms necessary to observe 1 photon, given as

$$\eta = \frac{\text{Number of Fe Atoms}}{\text{Peak Height}}. \tag{5.2}$$

The number of Fe atoms was deduced from the measured neutral beam current divided by the Faraday cup conversion efficiency, which was empirically determined to be 9.2 ± 0.5 for

ferrocene using the procedure described in Section 3.5.5, and multiplied by the counting time. Assuming that 13% of the ion beam extracted from the EI source was $^{56}Fe^{+}$ (Section 4.2.4), a sensitivity of $\eta = (20,000 \pm 7,000)$atoms/photon was obtained. The sensitivity was deduced assuming the laser light probed the entire atomic beam profile.

5.2 ^{55}Mn I hyperfine structure measurements

The atomic structure of Mn I relevant to the laser-excitations employed in this work is presented in Figure 5.4. The solid lines in Figure 5.4 represent the laser-exciations used and the dashed lines indicate the expected de-excitation of the excited states. The Einstein coefficient for the transition between the $3d^5 4s^2\ ^6S_{5/2}$ ground state to the $3d^5 4s4p\ ^6P_{7/2}$ state at 24802.25 cm^{-1} is $A_{ik} = 1.73 \times 10^7$ s^{-1} [77], and the branching fraction is 96.82%. Other states populated during the de-excitation include the $3d^6 4s\ ^6D_{7/2}$ state at 17282.00 cm^{-1} (0.64%) and the $3d^6 4s\ ^6D_{9/2}$ state at 17052.29 cm^{-1} (2.44%). The wavelength of fluorescence resulting from de-excitations of the $^6P_{7/2}$ level to the $^6D_{9/2}$ and $^6D_{7/2}$ levels was ∼1200 nm, in a wavelength region that the PMT was not sensitive to.

A transition from the $^8P^o_{9/2}$ metastable state at 18705.37 cm^{-1} in Mn I that was populated in the charge-exchange reactions was investigated as well. The $^8P^o_{9/2}$ state lifetime is greater than 100 μs, and the state did not radiatively decay within the flight time from the CEC through the detection system of < 5 μs. The Einstein coefficient for the transition between the $3d^5(^6S)4s4p(^3P_0)\ ^8P^o_{9/2}$ state and the $3d^5 4s(^7S)4d\ ^8D_{11/2}$ level at 46712.58 cm^{-1} is $A_{ik} = 1.93 \times 10^8$ s^{-1} with a branching ratio of 99.99%.

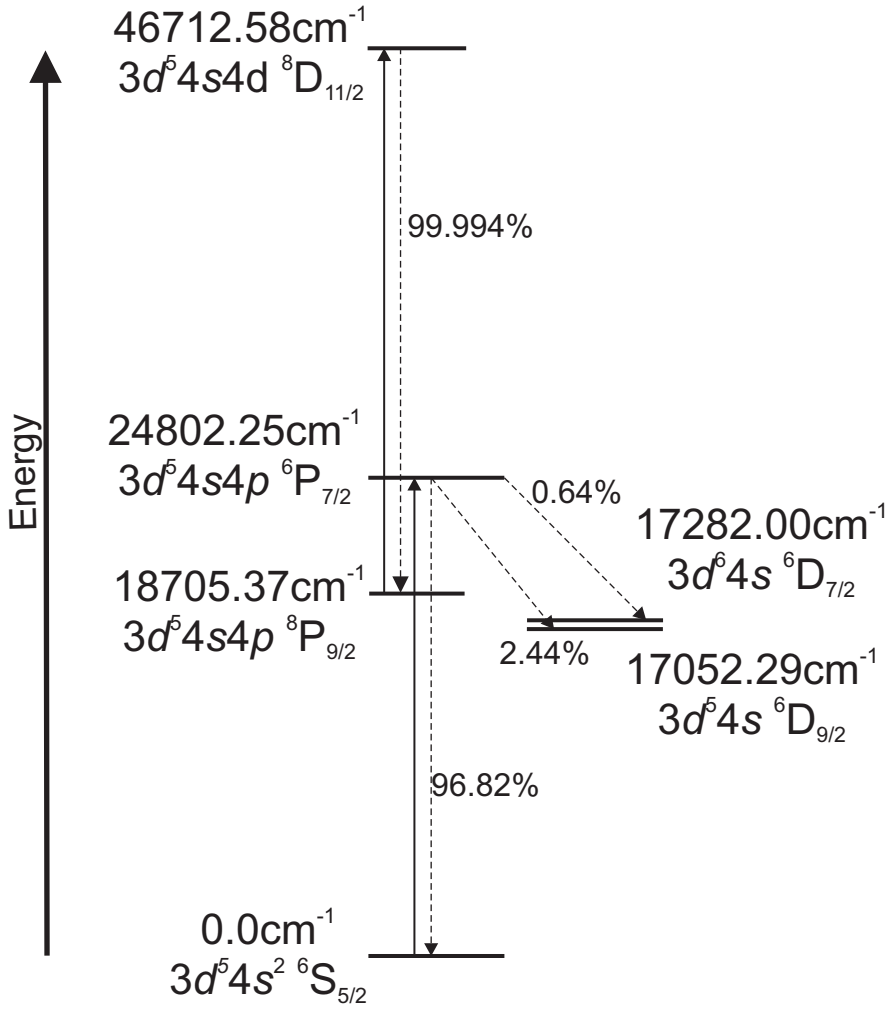

Figure 5.4: Partial atomic structure of Mn I relevant to the present work. Solid lines indicate laser-exciations, and dash lines represent the expected de-excitation pathways for fluorescence.

5.2.1 Mn^+-Na charge-exchange

The ionization potential of Mn is 7.43402 eV and the ionization potential of Na is 5.13908 eV [3], thus an energy gain of 2.29494 eV is expected in Mn from the transfer of an electron from the ground state of Na to the ground state of Mn. The 18705.37 cm^{-1} level in Mn I is 2.31911 eV above the Mn I ground state, making this state nearly resonant with the ground state of Na I. In this work, both the non-resonant exchange between the Na and Mn ground state and the near-resonant exchange from Na to the Mn metastable state were studied. The charge-exchange reactions studied are depicted in Figure 5.5.

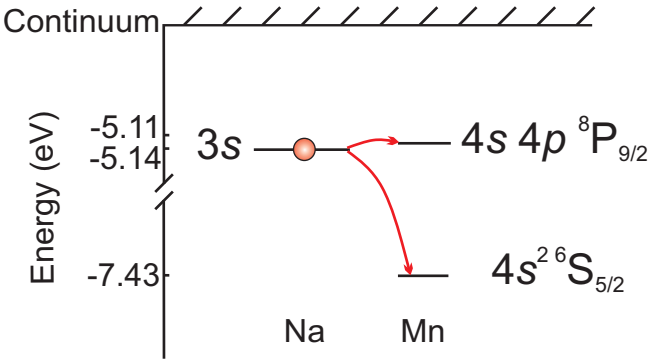

Figure 5.5: The charge-exchange processes between Na and Mn^+ that were investigated in this work.

5.2.2 HFS by exciting the Mn I ground state

A representative laser-induced fluorescence spectrum of the Mn I $^6P_{7/2} \rightarrow ^6S_{5/2}$ transition is presented in the top panel of Figure 5.6. The nuclear spin of ^{55}Mn is $I_N = 5/2$, leading to hyperfine levels of $F = 0$ to $F = 5$ for the $^6S_{5/2}$ ground state. Allowed hyperfine transitions are depicted in the bottom panel of Figure 5.6. All 15 allowed transitions were observed. The spin-factor intensities of the transitions, calculated using Eqn 2.16, are shown in the middle panel of Figure 5.6.

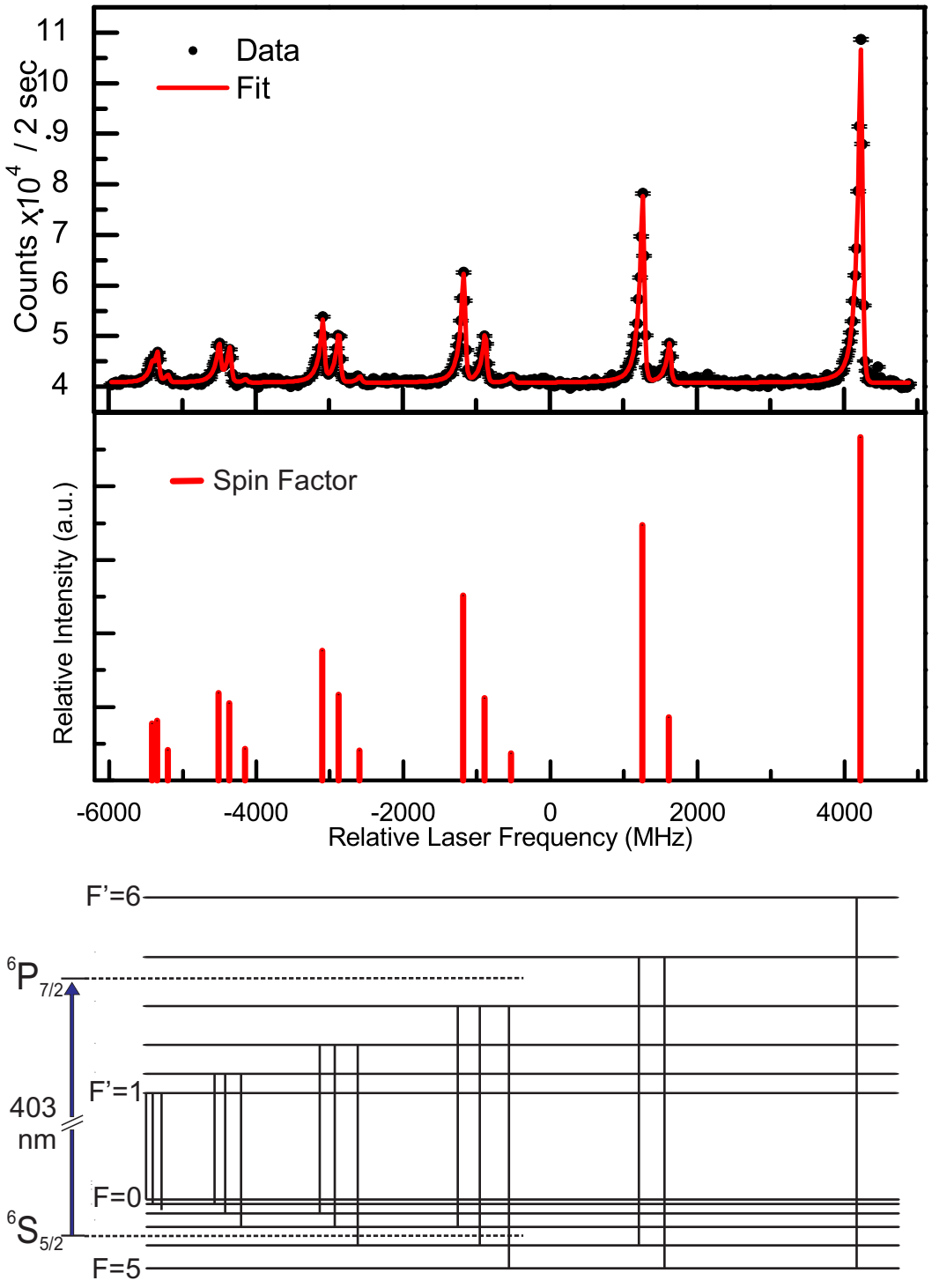

Figure 5.6: A representative laser-induced fluorescence spectrum of the $^6P_{7/2} \rightarrow ^6S_{5/2}$ transition in Mn I is presented in the top panel. The spin-factor intensities and a schematic of all allowed HFS transitions are shown in the middle and bottom panels, respectively.

The 15 peaks in the HFS were simultaneously fitted to the A and B hyperfine coupling constants for each level and the center-of-gravity frequency of the HFS transition. The asymmetric Voigt profile discussed in Section 2.3.5 was used as the resonance profile. The spectrum was fitted assuming all peaks had common widths and asymmetry parameters. The frequency, $\nu_{FF'}$, of each $F \rightarrow F'$ resonance was given as:

$$\begin{aligned}\nu_{FF'} =& \nu_{cg} + \frac{1}{2}\left[A_U C(F', I_N, J) - A_L C(F, I_N, J)\right] \\ &+ \frac{3}{4}\left[B_U D(F', I_N, J) - B_L D(F, I_N, J)\right],\end{aligned} \tag{5.3}$$

where

$$D(F, I_N, J) = \frac{C(F, I_N, J)(C(F, I_N, J) + 1) - I_N(I_N + 1)J(J + 1)}{2I_N(2I_N - 1)J(2J - 1)} \tag{5.4}$$

and

$$C(F, I_N, J) = F(F + 1) - I_N(I_N + 1) - J(J + 1). \tag{5.5}$$

The L and U subscripts denote the lower and upper levels of the laser excitation, respectively. The intensities of all peaks were free parameters in the fit, with initial values estimated from Eq 2.16 with $q = 0$. The center-of-gravity frequency, ν_{cg}, for the transition and the A and B factors deduced from the fit are listed in Tables 5.2 and 5.3, respectively. The uncertainties in the centroid values are the statistical error from the fit, the variation of the independent data sets, and the laser frequency uncertainty. Ten HFS data sets were analyzed from Mn^+ produced using the MIVOC + EI source and one data set was analyzed from Mn^+ produced using the plasma source. The presented uncertainties in the A and B hyperfine coupling constants include the statistical error from the fit routine, given as the first uncertainty. Systematic errors, mostly from the spread of A and B constants in all of the independent

Table 5.2: The center of gravity frequency of the $^6P_{7/2} \rightarrow ^6S_{5/2}$ transition in Mn I extracted from the measured HFS.

Ion Source	Center of Gravity (ν_{cg}) (MHz)	Literature ν_{cg} (MHz)	Ref
Plasma	743,552,987.9 $\pm(0.1) \pm (0) \pm (300)$	$743,552,700 \pm 300$	[76]
EI	743,553,038.2 $\pm(0.1) \pm (3.7) \pm (300)$		

Table 5.3: The A and B hyperfine coupling constants of the $^6P_{7/2}$ and $^6S_{5/2}$ levels in Mn I extracted from the measured HFS.

Level (cm^{-1})	Factor	Present (MHz)	Literature (MHz)	Ref
0.0	A	$-72.5 \pm (0.03) \pm (0.5)$	-72.420836 ± 0.000015	[78]
0.0	B	$0.2 \pm (0.3) \pm (1.8)$	-0.019031 ± 0.000017	[78]
24802.25	A	$428.2 \pm (0.02) \pm (0.5)$	429.16 ± 0.05	[79, 80]
24802.25	B	$61 \pm (0.3) \pm (2.5)$	66.6 ± 1.3	[79, 80]

data sets, are presented as the second uncertainty. The uncertainty introduced from the He-Ne laser reference uncertainty, namely the 300 MHz shift in the center-of-gravity frequency, did not not affect the deduced A and B values given the present resolution of the experimental apparatus. The A and B coupling constants deduced from the current CLS measurement agree with the literature values, which are also presented in Table 5.3.

The FWHM of the resonance line shape was (90±10) MHz and the asymmetry parameter was 0.021 ± 0.001 for typical runs when the charge-exchange neutralization efficiency was $\sim 40\%$. Approximately half of the line width broadening can be attributed to the 2.3-eV energy gain the charge-exchange process. The differential Doppler-shift of the ^{55}Mn beam at 15 keV was 18.98 MHz/V, corresponding to a 43 MHz line width broadening from the 2.3 eV change in energy.

The relative intensities of the hyperfine transitions were investigated as a function of the laser power used to excite the transitions to determine the effect of hyperfine pumping

(Section 2.3.6). The relative intensities of the Mn I ground state transitions are shown as a function of laser power in Figure 5.7. The peak intensities were normalized to the cyclic $F = 5 \rightarrow F' = 6$ transition (peak number 15 in Figure 5.7) and set to 1 for each data set.

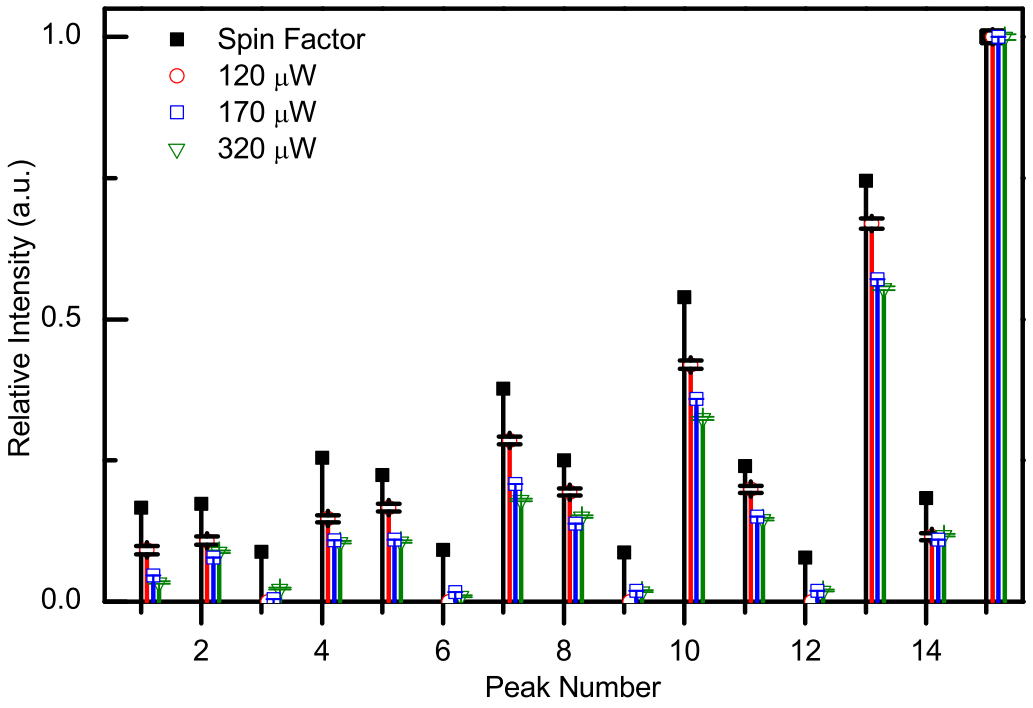

Figure 5.7: Relative intensities in the $^6P_{7/2} \rightarrow ^6S_{5/2}$ HFS as a function of the applied laser power. The peaks are numbered from low to high transition frequency.

5.2.3 HFS by exciting Mn I metastable state

A representative hyperfine spectrum of the $^8D_{11/2} \rightarrow ^8P^o_{9/2}$ transition is presented in the top panel of Figure 5.8. The data presented in Figure 5.8 were collected in two seperate frequency scans: the first from -6000 MHz to -3000 MHz, and the second from -3000 MHz to 1000 MHz relative to the deduced center of gravity frequency of the $^8D_{11/2} \rightarrow ^8P^o_{9/2}$ transition. The peak intensities calculated using Eq 2.16 are shown in the bottom panel.

Eleven of the sixteen allowed transitions were observed. The 5 lowest intensity peaks were not detected for the given sensitivity and stability of the CLS system.

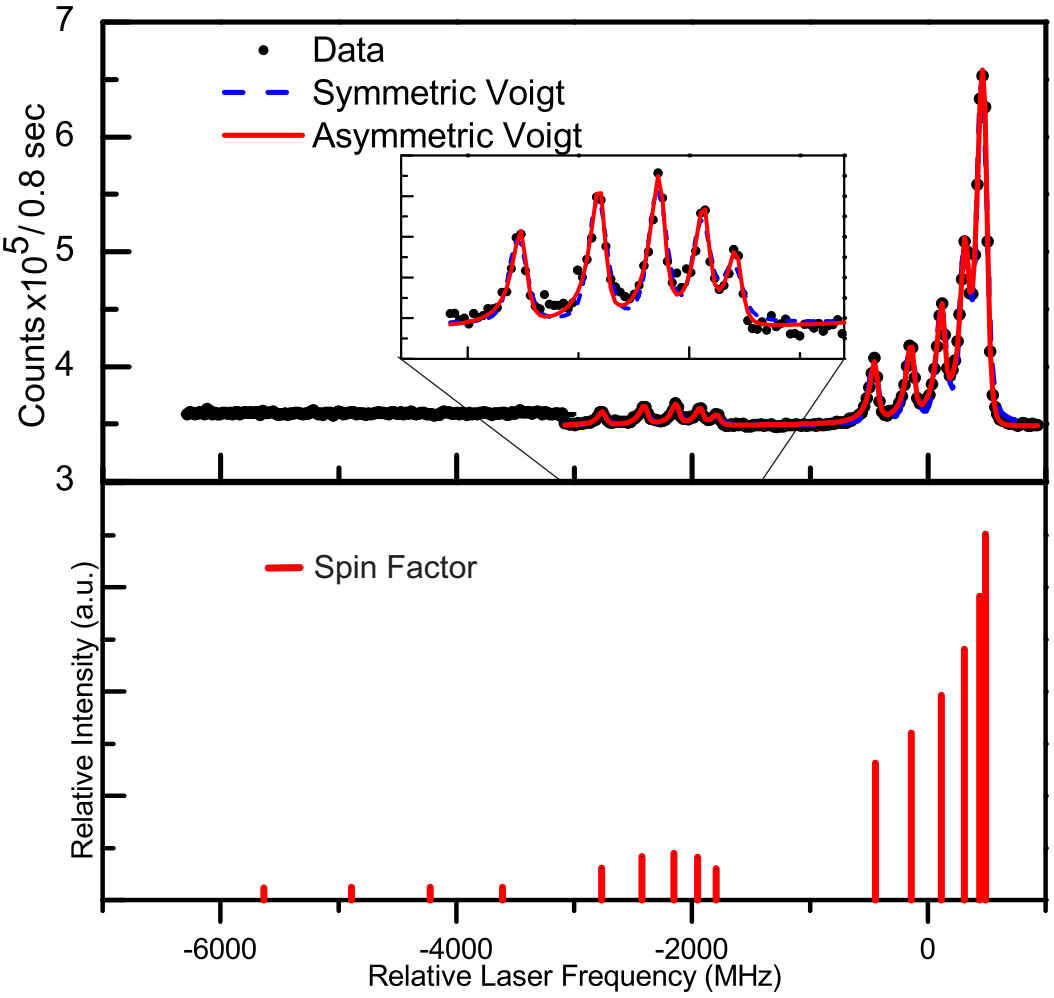

Figure 5.8: Representative laser-induced fluorescence spectrum of the $^8\mathrm{D}_{11/2} \rightarrow ^8\mathrm{P}^{\mathrm{o}}_{9/2}$ transition in Mn I. Symmetric and Asymmetric line shapes were fitted to the data, and the residuals are presented. Spin-factor intensities are included in the bottom panel.

The 11 observed peaks in the HFS of the Mn I metastable state were simultaneously fitted in terms of the A and B hyperfine coupling constants as described for Mn I in Section 5.2.2. Results of the fits using the symmetric Voigt function and asymmetric Voigt function are shown in the top panel of Figure 5.8. The χ^2/ν values from the fitting routine were found to

Table 5.4: The center of gravity frequency of the $^8D_{11/2}$ and $^8P^o_{9/2}$ levels in Mn I extracted from the measured HFS.

Ion Source	Center of Gravity (ν_{cg}) (MHz)	Literature ν_{cg} (MHz)	Ref
EI	839,635,425.2 $\pm(0.1) \pm (9.5) \pm (300)$	$839,635,000 \pm 300$	[76]

Table 5.5: The A and B hyperfine coupling constants of the $^8D_{11/2}$ and $^8P^o_{9/2}$ levels in Mn I extracted from the measured HFS.

Level (cm^{-1})	Factor	Present (MHz)	Literature (MHz)	Ref
18705.37	A	$455.19 \pm (0.09) \pm (0.4)$	456 ± 4	[80, 81]
18705.37	B	$73 \pm (2) \pm (5.5)$	48 ± 27	[81]
46712.58	A	$409.4 \pm (0.1) \pm (0.7)$	432 ± 11	[82, 83]
46712.58	B	$-52 \pm (2) \pm (5.5)$	–	–

decrease from $\chi^2/\nu = 69$ for the symmetric Voigt profile to $\chi^2/\nu = 5.9$ for the asymmetric profile.

The deduced center-of-gravity frequency and A and B coupling constants from the asymmetric fit function are listed in Tables 5.4 and 5.5, respectively. The uncertainty of the center of gravity and of the A and B coupling constants were treated in a manner similar to the Mn I ground state transition in Section 5.2.2. Six data sets were independently analyzed to determine the run-ro-run variation in the fit parameters. The deduced A and B coupling constant values agree with reported values, where available, and improve on the precision of previous measurements by $\sim$2 orders of magnitude.

The FWHM of the resonance line shape was (70$\pm$10) MHz and the asymmetry parameter was 0.017 ± 0.001 for typical runs when the charge-exchange neutralization efficiency was $\sim$ 40%. The narrower linewidth and smaller asymmetry parameter of the metastable transition compared to the ground state transition were consistent with expectations from the charge-

exchange processes. The metastable state is near-resonant charge transfer between the Na vapor with Mn compared to the non-resonant process of charge-transfer from Na to the ground state in Mn. The non-resonant process led to a broadened line shape as discussed above in Section 5.2.2. The narrow linewidth of the metastable state transition compared to the ground state transition is an advantage for low count-rate experiments; for a given number of collected photons, the resonance signal height will increase as the line width decreases.

5.2.4 Relative populations of the ground and metastable states in Mn I populated via charge-exchange with Na

The relative populations of the ground and metastable states in Mn I populated in atomic charge-exchange of Mn^+ + Na can be determined from the relative sensitivity, η, given in Eqn 5.2, for each transition. The peak height was defined as the height of the cyclic hyperfine transition in either the $^8D_{11/2} \rightarrow ^8P^o_{9/2}$ or $^6P_{7/2} \rightarrow ^6S_{5/2}$ transitions. The measured neutral beam current was divided by the Faraday cup conversion efficiency for the beam produced from the manganocene charge, 7.7 ± 1.2, to obtain the normalized neutral current.

There were multiple HFS transitions in the measured ^{55}Mn I ground and metastable spectra, and the height of the cyclic HFS transitions were compared for the ground and metastable state laser excitations. The percent of the total m_F states in the $^6S_{5/2}$ state that have $F = 5$ and the $^8P^o_{9/2}$ state that have $F = 7$ are 30.5% and 25% of the total m_F states of these levels, respectively. The initial distribution amongst m_F states was assumed to be equal, and thus number of atoms should be scaled to reflect the differing fraction of m_F states in the hyperfine level from which the cyclic HFS transition was probed. In

addition, the relative intensities of the two transitions were scaled by the spin factor, given in Eqn 2.16. The laser intensity used to excite each transition was much smaller than the saturation intensities for each transition, and the intensity of the peaks was normalized for laser power, assuming a linear relation between laser power and peak intensity. The neutral current was not solely due to Mn, as discussed in Section 4.3.2, thus η was a function of the MIVOC-chamber temperature. The normalized η value, called η', is plotted as a function of the temperature of the MIVOC chamber in Figure 5.9

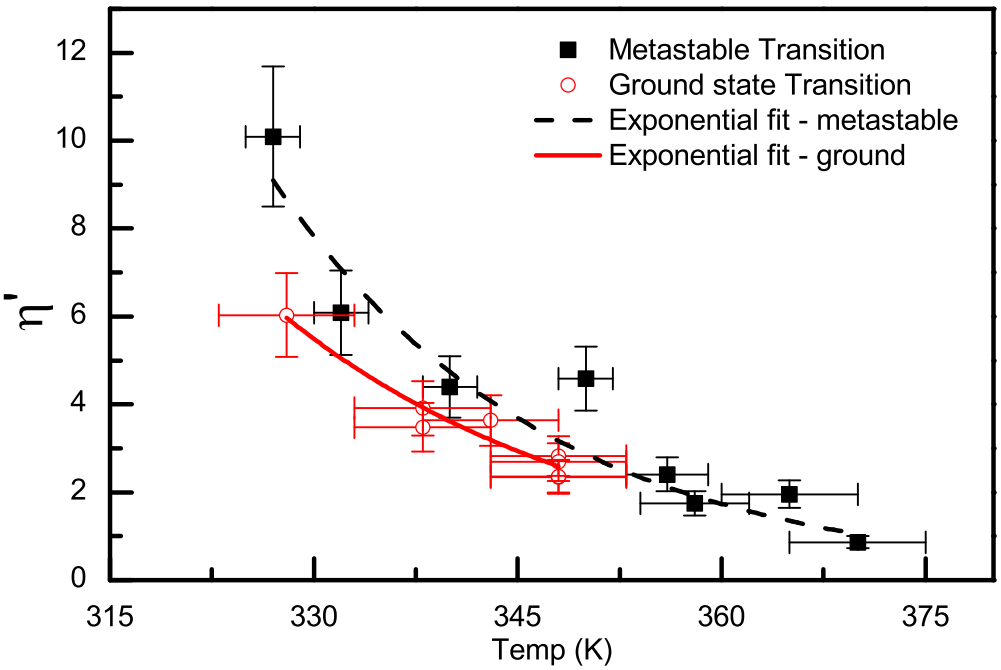

Figure 5.9: Normalized number of atoms per photon as a function of temperature for the Mn I ground and metastable state transitions.

An exponential relation, $\eta' = \alpha \exp[T/\beta]$ was fitted to each data set, where α and β were fit parameters. Using the extracted parameters from the fits to the data, the ratio of $\eta'_{\text{metastable}}/\eta'_{\text{ground}}$ was determined to be 0.7(3). Therefore, the population of the ground

state was $\sim 50\%$ larger compared to the population of the metastable state for the given experimental conditions.

Chapter 6

Discussion

The results of the present work to reliably produce ion beams of refractory elements as well as the collinear laser spectroscopy of neutral ^{56}Fe and ^{55}Mn atoms were presented in Chapters 4 and 5, respectively. A discussion of the results is provided in this chapter.

6.1 Plasma ion source

Singly-charged ion beams of K, Ca, and Mn were extracted from the commercial Colutron model 100 plasma ion source. The intensities of the ion beams extracted from the plasma source were mostly determined by the temperature of the source and vapor pressure of the charge material. The temperature of the charge was directly related to the filament input power as presented in Eqn 2.1, and thus the charge evaporated at a faster rate as the filament input power increased.

The saturated vapor pressures of the metallic charges [3] investigated here are shown as a function of temperature in Figure 6.1. Successful CLS measurements were obtained for those metallic elements which were produced from charges that had (relatively) high vapor pressures. The exception was In, for which a CLS signal was not obtained. Indium has a very low melting point (430 K) compared to the other metallic charges, which all have melting points above 1100 K [3]. The indium charge may have melted and vaporized from

the charge holder before a stable ion beam was extracted from the source. However, the exact reason was not clear.

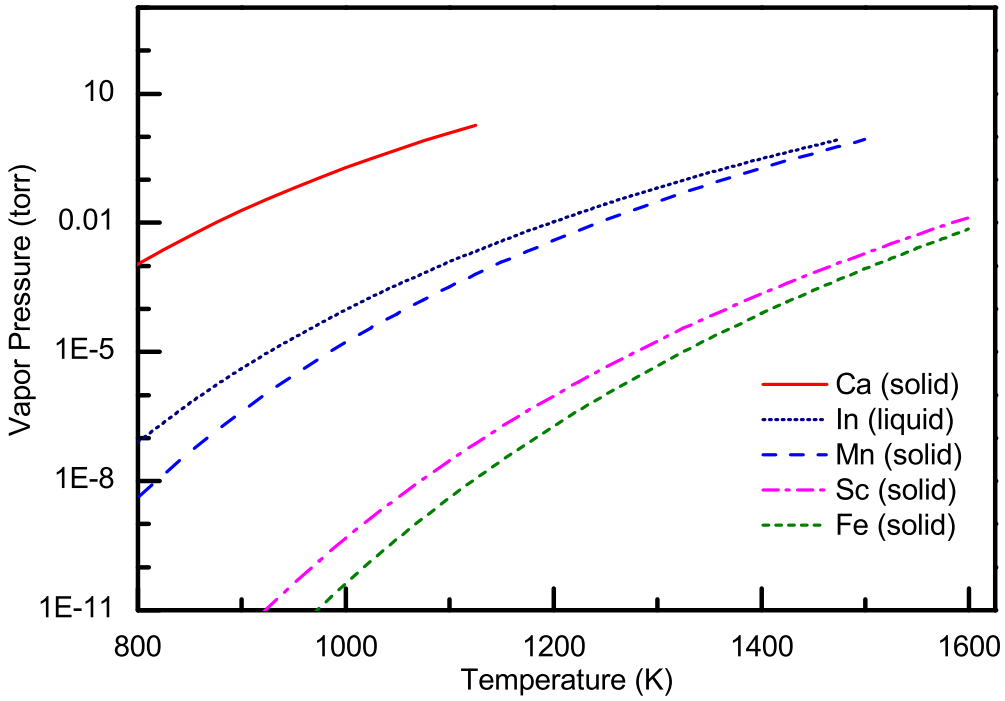

Figure 6.1: Saturated vapor pressures Colutron charges investigated as a function of temperature from Ref [3].

The advantage of the plasma source was the ability to produce ion beams from metallic or ionic salt charges, which had a relatively high vapor pressures. In addition, intense ion beam currents as high as a few μA were measured at the first BOB with the 5 mm aperture. Drawbacks of this source included a long start-up routine (approximately one hour) to generate a stable plasma. Geometrical constraints on the placement of a solid charge inside the chamber limited the amount of the charge that could be used and lead to a relatively short lifetime of the source, from 10 - 80 hours depending on the charge used. Service of the ion source and installation of a new charge was time-intensive as well; venting the source chamber, cleaning the chamber, installing a new charge, and off-gassing

the chamber under vacuum typically required 20 - 30 hours to complete. During an on-line CLS experiment, the time required to re-start the Colutron plasma source would introduce a risk that the necessary stable beam would not be available for reference measurements. In addition, the plasma source was not a viable option to produce transition metal ion beams in general.

6.2 EI source with MIVOC technique

The MIVOC chamber used in combination with the EI source successfully produced singly-charged ion beams of ^{56}Fe and ^{55}Mn. The production limits of the MIVOC + EI setup were dependent on the charge used.

6.2.1 EI source parameters

The EI source was found to be reliable and stable for 100's of hours of operation. Experimental optimization of the bias voltages applied to the filament, repeller cage, and extraction plate indicated that the speciation of the MIVOC charge did not change as a function of the bias voltages. Typical extracted beam currents measured at the first BOB with the 5 mm aperture were of order 1-10 nA. The intensity of the extracted beam was found to saturate at the 10's of nA level, regardless of the bias voltage settings or the input power to the filament. An extraction plate hole diameter of 4-6 mm was optimal for the extracted ion beam intensity.

Use of the EI source without the repeller cage was preferred as the source was considered to be more mechanically sound without the repeller. The factor of two drop in emission

current without the repeller could be compensated by increasing the input power applied to the filament.

Two filament materials were found to provide acceptable source performance. The thoria-coated iridium filament required lower input power to generate electrons, but this filament was significantly ($> 50\times$) more expensive than the thoriated tungsten filament. The thoria-doped tungsten could provide the necessary electron emission, and was also mechanically superior as the wire was relatively easy to manipulate. The thoria-coated iridium filament was found to be sensitive to mechanical stress and small portions of the thoria coating flaked off during installation and adjustment.

6.2.2 Production limits

The saturated vapor pressure of the MIVOC charge and the speciation of the charge in the EI source both need to be considered when discussing the limits of production of singly-charged metal ions using this source. A useful figure of merit, FoM, for the production limits of the MIVOC technique in combination with the EI source can be defined as the product of the saturated vapor pressure, VP (Torr), and the fraction, F, of the initial charge that is extracted as a singly-charged element of interest;

$$\text{MIVOC FoM} = \text{VP} \times \text{F}. \tag{6.1}$$

CLS studies were attempted using three iron-containing MIVOC charges: ferrocene, ferric chloride, and iron(III) acetylacetonate. The $^{56}Fe^{+}$ FoM for the three charges is shown as a function of temperature in Figure 6.2. Saturated vapor pressures of the three charges

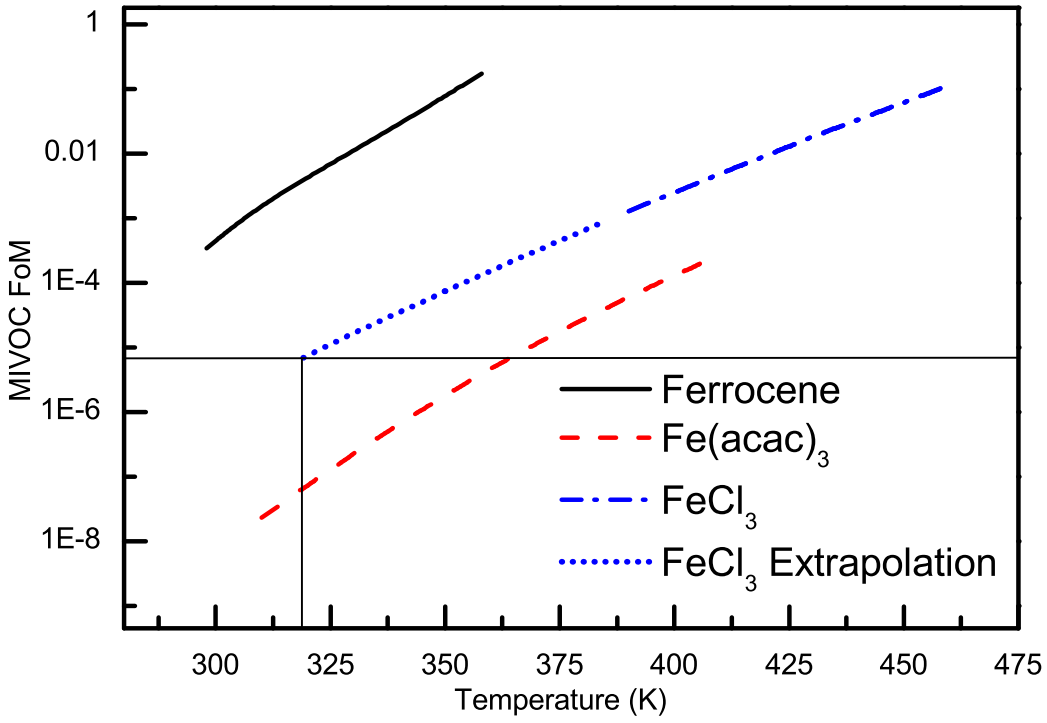

Figure 6.2: The MIVOC figure of merit of the three iron-containing charges investigated plotted as a function of temperature.

were obtained from Refs. [39, 84], [73], and [85, 86] for ferrocene, $FeCl_3$, and $Fe(acac)_3$, respectively.

The speciation of $FeCl_3$ was not measured using the RGA in the present study. A speciation of 20% $^{56}Fe^+$ of the $FeCl_3$ charge was assumed based on the simple structure of the compound. In addition, vapor pressure parameterization of $FeCl_3$ was only valid in the temperature range of 390-460 K. The $FeCl_3$ parameterization was extrapolated to 318 K and is shown as a dotted line in Figure 6.2. A resonance signal using the $FeCl_3$ charge was obtained at a temperature of 318 K, where the MIVOC FoM was $\sim 7 \times 10^{-6}$. Therefore, a MIVOC FoM of $> 7 \times 10^{-6}$ is taken to be necessary in order to achieve an ion beam of $^{56}Fe^+$ from which a fluorescence signal can be detected under the current experimental conditions.

The FoM shown for $Fe(acac)_3$ is something of an upper bound, as all of the $M/Q = 56$ line in the RGA spectrum was assumed to be $^{56}Fe^+$. The RGA spectrum obtained for the $Fe(acac)_3$ charge had several features in the $M/Q = 56$ region, and some fraction of the $M/Q = 56$ line may have been due to species other than singly-charged ^{56}Fe ions. In addition, only fragments with $M/Q < 300$ were collected. Fragments such as the molecular ion of $Fe(acac)_3$ could not be measured. The fraction of ^{56}Fe in the $M/Q = 56$ line of the RGA spectrum obtained in this work could be 1-2 orders of magnitude lower than the other components in the peak, based on the electron ionization speciation of $Fe(acac)_3$ reported in Ref [76] where the $M/Q = 56$ line was only 0.7% of the total $Fe(acac)_3$ spectrum intensity.

The Fe bond lengths of the charge materials investigated in this work are presented in Table 6.1. The bond length is generally inversely correlated to the bond energy, thus the Fe-O bond in $Fe(acac)_3$ is the strongest of the Fe-bonds in the materials investigated. The higher bond energy implies that the probability of breaking the Fe bond via collisions with energetic electrons is the lowest for $Fe(acac)_3$. In addition, the large number of atoms in

Table 6.1: Bond lengths of the Fe bonds in the MIVOC charges investigated.

Compound	Bond	Bond Length (Å)	Ref
ferrocene	Fe-C	2.04	[87]
$FeCl_3$	Fe-Cl	2.14	[88]
$Fe(acac)_3$	Fe-O	1.99	[89]

the $Fe(acac)_3$ molecule (43 atoms) compared to ferrocene (21 atoms) and $FeCl_3$ (4 atoms) should lower the probability of creating a bare $^{56}Fe^+$ fragment. Both the high Fe-O bond energy and molecular complexity of the $Fe(acac)_3$ are thus expected to hinder the creation of Fe^+ ions in the electron ionization process.

The vapor pressure of manganocene was not found in the literature, but can be estimated using the Watson method [90], which is an empirical relation that parameterizes the saturated vapor pressure of a solid in terms of the boiling point of the compound. The Watson method predicts similar vapor pressures for ferrocene and manganocene, although it underestimates the vapor pressure of ferrocene by an order of magnitude, which is the expected accuracy of the Watson method [90].

Comparison of the ability to perform CLS starting with manganocene and ferrocene requires further considerations as the FoM given in Eqn 6.1 does not account for the population of hyperfine levels. The population of the $^5S_{5/2}$ ground state in ^{55}Mn I was distributed among 36 m_F levels. Of these 36 m_F levels, 11, or $\sim$30%, were substates in the $F = 5$ hyperfine level, from which a CLS signal was detected at 319 K. Another factor to consider when comparing two neutral species is the relative cross section for populating the electronic state from which spectroscopy is performed. In particular, higher-lying electronic states that are populated in the charge-exchange process may promptly decay to the state under study. As discussed in Section 6.4.3, the relative cross section for populating the Fe I ground state

was a factor of 4 larger than that for populating the Mn I ground state. Scaling the FoM for the hyperfine level distribution, charge-exchange cross section, and assuming the vapor pressure of manganocene is within a factor of five of the vapor pressure of ferrocene, the FoM of manganocene at 319 K (the lowest temperature at which a CLS signal was realized) was $6 \times 10^{-5} - 1 \times 10^{-3}$, approximately one order of magnitude higher than the FoM deduced from the Fe analysis.

6.2.3 Lessons learned

The MIVOC + EI source proved to be a reliable source of singly-charged refractory element (Mn and Fe) beams from metallocene charges. The isolation of the MIVOC chamber from the EI chamber was also advantageous compared to the integral charge in to the plasma source chamber. The MIVOC chamber could be disassembled while leaving the EI chamber intact, allowing for easy maintenance of the MIVOC chamber. The relatively large amount (0.5 g) of charge installed in the MIVOC chamber provided a long lifetime compared to the 10-50 mg of charge that could be installed into the Colutron source charge holder. The startup, control, and stability of the extracted ion beam from the MIVOC + EI setup was acceptable for CLS studies; the source could be run for more than a few hours without adjustment of any source parameters after a startup procedure of around 10 minutes.

Nevertheless, there are some changes that could be implemented to improve the performance of the MIVOC + EI source. One example is the modification of the MIVOC chamber. The 70-mm Conflat six-way cross vacuum chamber had a large surface area in a difficult geometry to efficiently heat with heating tape. A smaller chamber, for example a 70-mm Conflat-T connector could be used instead. Reducing the surface area by about half

and simple geometry would allow better uniform heating of the chamber to avoid charge condensation.

Another component that could be improved is the leak valve that separates the MIVOC chamber from the EI chamber. The MKS 248 leak valve assembly included a permanent magnet and was limited to operating temperatures of less than 373 K. The maximum throughput of the MKS 248 leak valve was specified to 50 l/s with at inlet pressure of 760 Torr. The leak valve was typically operated fully open, and it would be favorable to use a manual valve with a large throughput that could operate at temperatures up to 450 K.

The optimum charges in this work were ferrocene and manganocene. The metallocene compounds are hazardous, and some of the compounds oxidize in the air. Thus loading of the metallocene charges into the MIVOC chamber was done in an inert atmosphere in a glove box. The use of alternative metal-containing charges could be investigated, but it is difficult to identify metal-containing compounds with high vapor pressures and large speciation of singly-charged metal ions in the electron ionization process. Here, ferric chloride was stuided, but it was not as favorable as the ferrocene charge.

6.3 ^{56}Fe collinear laser spectroscopy

The centroid frequency of the Fe I $^5D_4 \rightarrow ^5F_5$ transition was found to be in agreement with the literature value [76], indicating that the beam kinetic energy and laboratory-frame laser frequency were accurately known to the error level in the present work and the procedure for the calibration of the scanning high-voltage system was properly performed.

The line shape of the fluorescence signal was found to be asymmetric due to inelastic collisions in the atomic charge-exchange process of Fe^+ with a Na vapor. The line shape

was fitted with both symmetric and asymmetric Voigt profiles, and the extracted centroids of the two fitted line shapes were found to be shifted by 1.5 MHz. The systematic error of the centroid was more than 300 MHz, thus the impact of the asymmetric line shape on the extracted centroid was negligible in this case.

The ^{54}Fe isotope is stable, with a 5.8% relative abundance. However, a resonance peak was not observed when the appropriate frequency range was scanned. It is estimated that a fluorescence spectrum of the $^5F_5 \rightarrow ^5D_4$ transition similar in quality to the measured ^{56}Fe spectrum can be obtained for ^{54}Fe if the overall sensitivity of the measurement increased by a factor of 10.

6.4 ^{55}Mn collinear laser spectroscopy

6.4.1 ^{55}Mn I transition frequencies and hyperfine coupling constants

The center of gravity frequencies of the Mn I $^6P_{7/2} \rightarrow ^6S_{5/2}$ transition obtained with Mn^+ beams produced from the plasma and EI ion sources were within 1 σ and 2 σ of the literature value [76], respectively. In addition, the extracted A and B hyperfine coupling constants deduced from the HFS were consistent with literature values [78, 79, 80, 91].

The center of gravity frequency determined from the $^8D_{11/2} \rightarrow ^8P^o_{9/2}$ transition HFS was found to agree with the adopted value in the literature [76]. The A coupling constants for both the $^8D_{11/2}$ and $^8P^o_{9/2}$ states as well as the B coupling constant for the $^8P^o_{9/2}$ state deduced from the HFS were consistent with the literature values [80, 81, 82, 83], and the precision of the deduced values was 1-2 orders of magnitude better than that of the previously

reported values, where available. The value of the B coupling constant of the $^8D_{11/2}$ state was not found in the literature.

The nuclear magnetic dipole moments of stable isotopes are known to a high precision [18] in general, and the error in deduced dipole moments of rare nuclei from measured A hyperfine coupling constants is mostly due to propagated uncertainty of the A constants (Eqn 1.43). In the present work, the relative uncertainties in the deduced A hyperfine coupling constants were less than 0.1% which will dominate the error of the extracted magnetic moment. The relative uncertainty of nuclear electric quadrupole moments for stable isotopes is generally on the order of 10% [18] due partly to the small effects of the quadrupole moment and difficulties to determine the electric field gradient. Deduced quadrupole moments of rare isotopes from measured B hyperfine coupling constants (Eqn 1.44) may be limited by the precision of the reference quadrupole moment. The relative uncertainties of B constants deduced in this work were generally on the order of 5%. The current results demonstrate that useful nuclear properties can be determined with an uncertainty of several percent or better with the current resolution of the CLS system.

6.4.2 Hyperfine pumping effects in the Mn I $^6P_{7/2} \rightarrow ^6S_{5/2}$ transition

The relative intensities of the HFS resonance peaks were observed to decrease with increasing laser power, as displayed in Figure 5.7. The magnitude of hyperfine pumping should increase with laser intensity [46] since the absorption rate increases linearly with the radiation field well below the saturation intensity. Some of the highest-intensity peaks in the $^6P_{7/2} \rightarrow ^6S_{5/2}$ HFS transition are shown as a function of laser power in Figure 6.3. The intensities calculated

from the spin factor (Eqn 2.16) are shown at a laser power of 0 μW. The labels in the legend of Figure 6.3 refer to the numbering scheme used in Figure 5.7. The intensity of the peaks

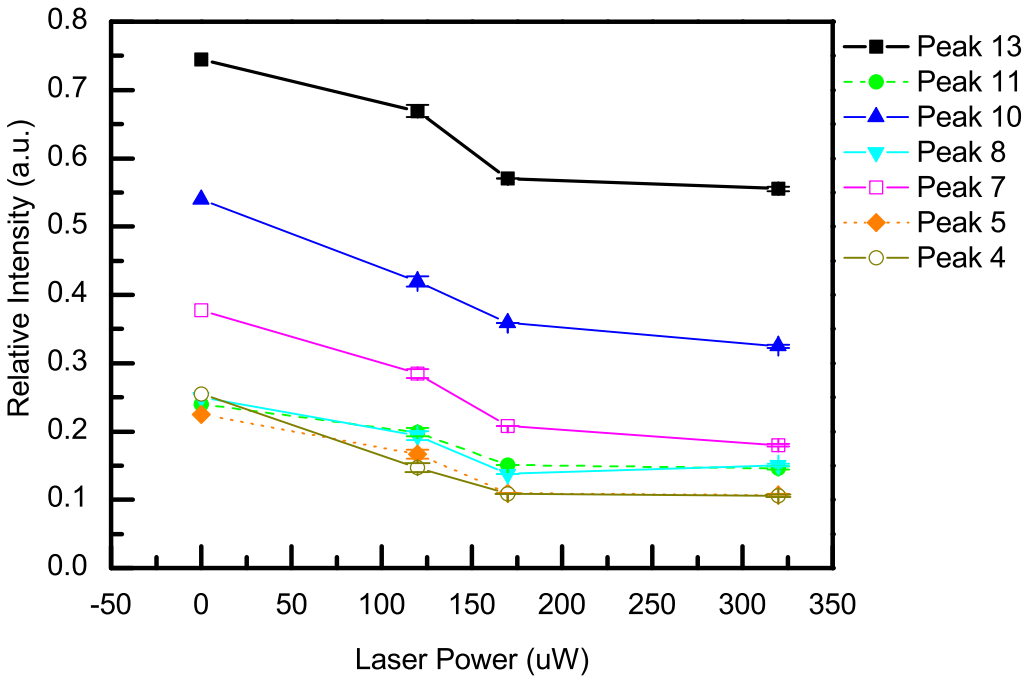

Figure 6.3: Relative intensities of the $^6P_{7/2} \rightarrow ^6S_{5/2}$ Mn I HFS as a function of laser power. The numbers used to identify the peaks are defined in the text.

was found to decrease with increasing laser power, consistent with the expectation of the hyperfine pumping effect discussed in Section 2.3.6.

6.4.3 Relative populations of atomic states in outgoing atom beams from charge-exchange

The cross sections for populating the two electronic states studied in Mn I from the Mn^+ + Na atomic charge-exchange reactions were calculated using the theory of Rapp and Francis [92] (including the corrections of Dewangan [93]). In the theory of Rapp and Francis, the

neutralization of Mn^+ by Na can be written as the elementary reaction:

$$Mn^+ + (Na^+ + e^-) \rightarrow (Mn^+ + e^-) + Na^+ + \Delta E, \tag{6.2}$$

with ΔE being the energy defect of the reaction. Semiempirical one-electron wave functions for $(Mn^+ + e^-)$ and $(Na^+ + e^-)$ are used, and are a function of the average ionization potential of Mn and Na atoms (6.28 eV). The molecular wave function for $MnNa^+$ is expressed in terms of a superposition of the atomic orbitals. The cross section is analytically calculated by integrating over the impact parameter for all collisiosn.

In the present formalism, the charge-exchange cross section, σ, is given by the expression

$$\sigma = 2\pi \int_0^{+\infty} P_\omega(b) \times b \times db, \tag{6.3}$$

where b is the impact parameter, and

$$P_\omega(b) = f \times P_0(b) \times \mathrm{sech}^2 \left[\frac{\omega}{v_z} \left(\frac{a_0 \pi b}{2\gamma} \right)^{1/2} \right] \tag{6.4}$$

is the probability of non-resonant charge transfer where $v_z = 2.23 \times 10^7$ cm/s is the velocity of the 15 keV Mn^+ beam. Here,

$$P_0(b) = \sin^2 \left[\frac{42 b^2}{a_0 \hbar v_z} \left(K_0(\gamma b/a_0) + \frac{K_1(\gamma b/a_0)}{\gamma b/a_0} \right) \right] \tag{6.5}$$

is the probability of resonant charge transfer, where f is a statistical factor dependent on the quantum numbers of the involved states, a_0 is the Bohr radius in cm, $\hbar$ is the Planck

Table 6.2: Atomic charge-exchange cross sections of states feeding the Mn ground state.

Level (cm^{-1})	Term Symbol	Branching Ratio	σ ($\times 10^{-15} cm^2$)	BR$\times\sigma$ ($\times 10^{-15} cm^2$)
0	$^6S_{5/2}$	–	2.02	2.02
24779	$^6P_{3/2}$	0.155	2.62	0.39
24788	$^6P_{5/2}$	0.269	2.62	0.71
24802	$^6P_{7/2}$	0.268	2.62	0.70
31001	$^4P_{5/2}$	0.080	0.00	0.00
31076	$^4P_{3/2}$	0.034	0.00	0.00
35690	$^6P_{3/2}$	0.152	2.10	0.32
35725	$^6P_{5/2}$	0.276	2.10	0.58
35770	$^6P_{7/2}$	0.275	2.10	0.58
44993	$^6P_{7/2}$	0.110	1.11	0.12
45156	$^6P_{5/2}$	0.126	1.53	0.19
45259	$^6P_{3/2}$	0.070	1.52	0.10
			Sum	5.71

constant divided by 2π in eV-s, $\gamma = I/13.6$, I is the average ionization potential, K_0 and K_1 are zero- and first- order Bessel functions of the second kind, respectively, and $\omega = \frac{\Delta E}{\hbar}$.

Results of the charge exchange cross sections calculated from Eqn 6.3 are presented in Tables 6.2 and 6.3. Direct charge-exchange cross sections to the ground state and $^8P^o_{9/2}$ metastable state were calculated along with charge-exchange reactions populating fine structure levels that had >1% branching to the ground or metastable state. The calculated cross sections were scaled by the branching ratio to the $F = 5$ or $F = 7$ levels of the ground or metastable states, respectively. Here it was assumed that all m_F states were equally populated for charge exchange to a given fine structure level.

Table 6.3: Atomic charge-exchange cross sections of states feeding the Mn $^8P^o_{9/2}$ metastable state.

Level (cm^{-1})	Term Symbol	Branching Ratio	σ ($\times 10^{-15} cm^2$)	BR$\times\sigma$ ($\times 10^{-15} cm^2$)
18705	$^8P_{9/2}$	1.0	3.62	3.62
39431	$^8S_{7/2}$	0.043	2.50	0.11
46708	$^8D_{7/2}$	0.010	1.92	0.02
46710	$^8D_{9/2}$	0.079	1.92	0.15
46712	$^8D_{11/2}$	0.375	1.92	0.72
			Sum	4.63

The relative population of the metastable state to the ground state including feeding from excited states was found to be

$$\frac{P_{\text{Metastable}}}{P_{\text{Ground}}} = \frac{4.63}{5.71} = 0.81, \tag{6.6}$$

in good agreement with the relative population of 0.7 ± 0.3 determined from the CLS measurements (Section 5.2.4).

The preferential population of the ground state compared to the metastable state is due to the high number of excited states which feed the ground state even though the cross section to directly populate the metastable state is 44% larger than that of the ground state. Even with the strong total population of the ground state, the population of the metastable state was large enough that a CLS signal was detected in this work.

Similar charge-exchange cross section calculations for all states that promptly decay to the ^{56}Fe I ground state were performed, and the population in the Fe I ground state is predicted to be a factor of 4 larger compared to the population of the $F = 5$ hyperfine level

of the Mn I ground state, mostly due to the distribution of electrons across all of the m_F states in ^{55}Mn.

6.5 Production of stable refractory element ion beams at BECOLA

The production of ion beams of refractory elements can be achieved with the MIVOC + EI setup using metallocene compounds which are commercially available for first row transition elements including V, Cr, Co, and Ni. The known vapor pressures of metallocene compounds indicate that the vapor pressures of these compounds are within a factor of three regardless of the metal atom in the complex [84, 94], thus extension of the existing setup to new compounds should be trivial. One near-term goal of the BECOLA project is on-line measurements of radioactive isotopes of first row transition elements; the MIVOC + EI setup will be able to provide valuable reference isotopes for these on-line measurements.

Chapter 7

Summary

7.1 Conclusions

Plasma and electron ionization ion sources were developed to generate singly-charged ion beams of stable Ca, K, Mn, and Fe isotopes. Various solid compounds were used as charge material for the ion sources including metal powders, ionic salts, and organometallic compounds. The MIVOC technique in combination with the EI source proved to be a reliable system to produce singly-charged ion beams of Fe and Mn from organometallic compounds. One major advantage of the MIVOC + EI setup was the separation of the generation of the charge vapor and the ionization process. The separate chambers allowed better system performance, reliability, and servicing than the charge/ionization chamber of the plasma source.

Collinear laser spectroscopy was performed on ^{56}Fe I and ^{55}Mn I. Fe^+ and Mn^+ were generated in one of the ion sources and extracted at an energy of 15 keV. The ion beam was neutralized via charge exchange with Na vapor, and the atomic beam was co-propagated with laser light. Atomic HFS were measured by detecting laser-induced fluorescence from the atomic beams. Spectroscopic measurements starting from the electronic ground state of the atomic beams was successfully performed. In addition, spectroscopy was performed using a long-lived metastable state in Mn I which was populated in the charge-exchange reactions.

The deduced center of gravity frequencies and hyperfine coupling constants for all transitions agreed with literature values and confirmed the successful operation of the BECOLA CLS system with off-line beams. Spectroscopic measurements starting from metastable states provides additional opportunities for identifying laser-excitation schemes.

7.2 Outlook

The MIVOC + EI source setup provided a reliable means for production of ion beams of Fe and Mn and can be extended to generate ion beams from the stable isotopes of V, Cr, Co, or Ni using commercial metallocene charges. It should be noted that the data for the nuclear ground state properties of rare isotopes of these elements are sparse [18]. On-line CLS measurements of first-row transition elements provides an opportunity to be exploited by the BECOLA facility, and the EI + MIVOC setup will be able to provide valuable reference isotopes for such measurements.

Improvements can be implemented to increase the sensitivity of the CLS system. A beam cooler and buncher [53, 54] is currently being installed in the BECOLA facility, upstream of the CLS beam line. The cooler and buncher will be used to cool the ion beam in both transverse and longitudinal directions via collisions with a He buffer gas. Additionally, the continuous ion beam will be spacially confined using an radio frequency quadrupole Paul trap and released in pulses. The pulsed structure of the ion beam will allow suppression of background during the CLS measurement by a factor of 10^3-10^4 compared to the use of a continuous beam simply due to data recording in a narrow time window.

Perhaps the most inefficient step in the delivery of the fragmentation products to the BECOLA facility is the beam thermalization process. At present, on the order of a few

percent of the fast rare isotope beam is extracted at thermal energies from gas cells [20, 95]. In addition, the extracted rare isotopes from the gas stopping system may be present in various molecular forms, which are not suitable for spectroscopy of elemental ions or atoms. An increase in efficiency in the beam thermalization process and/or an increase in the purity of the extracted rare isotope ions is important for laser spectroscopy studies.

The atomic charge-exchange process is another somewhat inefficient step in a CLS measurement of neutral species. In the case where the ground state of the singly-charged ion does not contain a suitable electronic transition for spectroscopy to be performed, the ion beam can be neutralized. Typically 40% to 60% of the incident ion beam is converted into an atomic beam as the density of the alkali vapor necessary to achieve neutralization efficiencies above 60% introduces undesirable asymmetry and broadening of the resonance line shape. On the other hand, the population of multiple electronic levels in the outgoing atomic beam was exploited in this work and near-resonant charge exchange was found to be advantageous to reduce the fluorescence line width. Nevertheless, the charge exchange process is inefficient and only can be avoided if spectroscopy can be performed on the ionic beam. One alternative to charge-exchange is to populate metastable states in the ion beam using a pulsed laser system while the rare isotopes are being cooled and bunched [96]. When laser light is made incident along the axis of the cooler and buncher the high-peak power of the pulsed laser system can induce weak transitions from the ionic ground state to long-lived metastable states from which spectroscopy may be performed.

Additional measurement techniques beside optical detection may be used for measurements of the ground state properties of rare isotopes produced at low rates. One example of such a technique is β-ray detection after NMR on rare isotopes that have been optically polarized [97]. The so-called β-NMR technique is 1-2 orders of magnitude more sensitive

compared to optical detection. The existing β-NMR system at NSCL [98, 99] is designed to be used within the BECOLA facility and will realize an increase increase in sensitivity in measurements of the nuclear magnetic dipole and electric quadrupole moments.

The future of laser spectroscopy studies at NSCL/FRIB using the BECOLA facility is exciting. Developments of the CLS beam line of BECOLA carried out as part of this work have laid a foundation and provides a path forward for on-line laser spectroscopy measurements of refractory elements at NSCL/FRIB.

BIBLIOGRAPHY

BIBLIOGRAPHY

[1] S.E. Stein. *Mass Spectra.* NIST Chemistry WebBook, NIST Standard Reference Database Number 69, 2013. http://webbook.nist.gov, (retrieved March 1,2013).

[2] Matisse user's guide, version 1.10. http://www.spectra-physics.com.

[3] D.R. Lide. *CRC Handbook of Chemistry and Physics.* CRC Press LLC, Boca Raton, Florida, 1999.

[4] David J. Griffiths. *Introduction to Quantum Mechanics.* Pearson Education, Inc., Upper Saddle River, New Jersey, 2005.

[5] H. Kopfermann. *Nuclear Moments.* Academic Press Inc. New York, 1958.

[6] Atam P. Arya. *Fundamentals of Atomic Physics.* Allyn and Bacon, Inc., Boston, 1971.

[7] C. Schwartz. Theory of hyperfine structure. *Phys. Rev.*, **97**:380, 1953.

[8] E. W. Otten. *Nuclear radii and moments of unstable isotopes, in: D.A. Bromley (Ed.), Treasie on Heavy Ion Science, Nuclei Far from Stability, vol. 8.* Plenum Publishing Corp.(Springer), New York, 1989.

[9] J. Billows and P. Campbell. High-resolution laser spectroscopy for the study of nuclear sizes and shapes. *J. Phys G: Nucl. Part. Phys.*, **21**:707, 1995.

[10] Wolfgang Demtroeder. *Laser Spectroscopy: Vol 1.* Springer-Verlag, Berlin, 2008.

[11] Spectra-physics. http://www.newport.com/cms/brands/spectra-physics.

[12] Toptica photonics. http://www.toptica.com/.

[13] Calpac lasers. http://www.calpaclasers.com/.

[14] E.B. Hensley. Thermionic emission constants and their interpretations. *J. Appl. Phys.*, **32**:301, 1961.

[15] A.A. Michelson. Visibility of interference-fringes in the focus of a telescope. *Phil. Mag.*, **31**:338, 1891.

[16] R. Neugart. Laser spectroscopy on mass-separated radioactive beams. *Nucl. Instru. Methods*, **186**:165, 1981.

[17] K. Blaum, J. Dilling, and W. Nörterschäuser. Precision atomic physics techniques for nuclear physics with radioactive beams. *Phys. Scr.*, **T152**:014017, 2013.

[18] N.J. Stone. Table of nuclear magnetic dipole and electric quadrupole moments. *Atomic Data and Nuclear Data Tables*, **90**:75, 2005.

[19] D.J. Morrissey, B.M. Sherrill, M. Steiner, A. Stolz, and I. Wiedenhoever. Commissioning the A1900 projectile fragment separator. *Nucl. Instrum. Methods B*, **204**:90, 2003.

[20] L. Weissman, D.J. Morrissey, G. Bollen, D.A. Davies, E. Kwan, P.A. Lofy, P. Schury, S. Schwarz, C. Sumithrarachchi, T. Sun, and R. Ringle. Converstion of ^{38}Ca/^{37}K projectile fragments into thermalized ion beams. *Nucl. Instrum. Methods A*, **540**:245, 2005.

[21] A. Bohr and V.F. Weisskopf. The influence of nuclear structure on the hyperfine structure of heavy elements. *Phys. Rev.*, **77**:94, 1950.

[22] S.L. Kaufman. High-resolution laser spectroscopy in fast beams. *Opt. Comm.*, **17**:309, 1976.

[23] K.-R. Anton, S.L. Kaufman, W. Klempt, G. Moruzzi, R. Neugart, E.W. Otten, and B. Schinzler. Collinear laser spectroscopy on fast atomic beams. *Phys. Rev. Lett.*, **40**:642, 1978.

[24] Ian G. Brown. *The Physics and Technology of Ion Sources*. Wiley-VCH Verlag GmbH & Co. KGaA, 2004.

[25] O.W. Richardson. Electron theory of matter. *Phil. Mag.*, **23**:594, 1912.

[26] S. Dushman. Electron emission from metals as a function of temperature. *Phys. Rev.*, **21**:623, 1923.

[27] C. Herrings and M.H. Nichols. Thermionic emission. *Rev. Mod. Phys.*, **21**:185, 1949.

[28] W. Kaiser and C.G.B. Garrett. Two-photon excitation in CaF_2: Eu^{2+}. *Phys. Rev. Lett.*, **7**:229, 1961.

[29] R.O. Jenkins. A review of thermionic cathodes. *Vacuum*, **19**:353, 1969.

[30] P.E. Gear. The choice of cathode material in a hot cathode ionization gauge. *Vacuum*, **26**:3, 1975.

[31] J.T Watson and O.D. Sparkman. *Introduction to Mass Spectrometry*. John Wiley & Sons, Inc., The Atrium, Southern Gate, Chichester, West Sussex, England, 2007.

[32] M. Gryziński. Two-particle collisions. I. general relations for collisions in the laboratory system. *Phys. Rev.*, **138**:305, 1965.

[33] M. Gryziński. Two-particle collisions. II. Coulomb collisions in the laboratory system of coordinates. *Phys. Rev.*, **138**:322, 1965.

[34] M. Gryziński. Classical theory of atomic collisions. I. theory of inelastic collisions. *Phys. Rev.*, **138**:336, 1965.

[35] F. Paschen. Ueber die zum funkenübergang in luft, wasserstoff und kohlensäure bei verschiedenen drucken erforderliche potentialdifferenz. *Annalen der Physik*, **273**:69, 1889.

[36] Francis F. Chen. *Introduction to Plasma Physics*. Plenum Press, New York, 1974.

[37] H. Koivisto, J. Ärje, and M. Nurmia. Metal ion beams from an ECR ion source using volatile compounds. *Nucl. Instrum. Methods in Phys. Res. B*, **94**:291, 1994.

[38] H. Koivisto, J. Ärje, and M. Nurmia. Metal ions from the volatile compounds method for the production of metal ion beams. *Rev. Sci. Instru.*, **69**:785, 1998.

[39] M.H. Jacobs, P.J. Van Ekeren, and C.G. De Kruif. The vapour pressure and enthalpy of sublimation of ferrocene. *J. Chem. Thermodynamics*, **15**:619, 1983.

[40] R. Neugart. Collinear laser spectroscopy on unstable isotopes - a tool of nuclear physics. *Hyperfine Interactions*, **24**:159, 1985.

[41] R. Neugart. Laser in nuclear physics - a review. *Eur. Phys. J. A.*, **15**:35, 2002.

[42] H.-Jürgen Kluge and W. Nörterschäuser. Lasers for nuclear physics. *Spectrochimica Acta Part B*, **58**:1031, 2003.

[43] B. Cheal and K.T. Flanagan. Progress in laser spectroscopy at radioactive ion beam facilities. *J. Phys. G: Nucl. Part. Phys.*, **37**:113101, 2010.

[44] N. Bendali, H.T. Duong, P. Juncar, J.M. Saint Jalm, and J.L. Vialle. Na^+ - Na charge exchange process studied by collinear laser spectroscopy. *J. Phys. B: At. Mol. Phys.*, **19**:233, 1986.

[45] A. Klose, K. Minamisono, Ch. Geppert, N. Frömmgen, M. Hammen, J. Krämer, A. Krieger, C.D.P. Levy, P.F. Mantica, W. Nörterschäuser, and S. Vinnikova. Tests of atomic charge-exchange cells for collinear laser spectroscopy. *Nucl. Instru. Methods A*, **678**:114, 2012.

[46] Harold J. Metcalf and Peter van der Straten. *Laser Cooling and Trapping*. Springer-Verlag New York, Inc., 1999.

[47] B.H. Armstrong. Spectrum line profiles: The Voigt function. *J. Quant. Spectrosc. Radiat. Transfer*, **7**:61, 1967.

[48] J. Humlicek. An efficient method for evaluation of the complex probability function: the Voigt function and its derivatives. *J. Quant. Spectrosc. Radiat. Transfer*, **21**:309, 1979.

[49] R.J. Wells. Rapid approximation to the Voigt/Faddeeva function and its derivatives. *J. Quant. Spectrosc. Radiat. Transfer*, **62**:29, 1999.

[50] A.L. Stancik and E.B. Brauns. A simple asymmetric lineshape for fitting infrared absorption spectra. *Vibrational Spectroscopy*, **47**:66, 2008.

[51] J.J. Olivero and R.L. Longbothum. Emperical fits to the Voigt line width: a brief review. *J. Quant. Spectrosc. Radiat. Transfer*, **17**:233, 1977.

[52] K. Minamisono, G. Bollen, P.F. Mantica, D.J. Morrissey, and S. Schwarz. Collinear laser spectroscopy and polarized exotic nuclei at NSCL. *Proc. Inst. Nucl. Theory*, **16**:180, 2009.

[53] K. Minamisono, P.F. Mantica, A. Klose, S. Vinnikova, A. Schneider, B. Johnson, and B.R. Barquest. Commissioning of the collinear laser spectroscopy system in the BECOLA facility at NSCL. *Nucl. Instru. Methods A*, **709**:85, 2013.

[54] A. Nieminen, P. Campbell, J. Billowes, D. H. Forest, J. A. R. Griffith, J. Huikari, A. Jokinen, I. D. Moore, R. Moore, G. Tungate, and J. Äystö. On-line ion cooling and bunching for collinear laser spectroscopy. *Phys. Rev. Lett.*, **88**:094801, 2002.

[55] FuG Elektronik GmbH. http://www.fug-elektronik.de/webdir/1/english.htm.

[56] Colutron research corporation. http://www.colutron.com/products/kit/kit.html.

[57] UltraVolt, Inc. http://www.ultravolt.com/.

[58] TDK-Lambda corportation. http://www.tdk-lambda.com/.

[59] MKS instruments, Inc. http://www.mksinst.com/.

[60] Stanford research systems, Inc. http://www.thinksrs.com/.

[61] ORTEC advanced measruement technology, Inc. http://www.ortec-online.com/.

[62] Mcmaster-carr supply company. http://www.mcmaster.com/.

[63] S. Vinnikova. Development and commissioning of a photon detection system for collinear laser spectroscopy at NSCL. Master's thesis, Michigan State University, 2011.

[64] Simion version 8.1. http://simion.com.

[65] M. Berz. Modern map methods for charge particle optics. *Nucl. Instru. Methods A*, **363**:100, 1995.

[66] J.G. Martel and N.T. Olson. Ion bombardment induced photon and seconday electron emission. *Nucl. Instrum. Methods*, **105**:269, 1972.

[67] J. B. Hasted. *Physics of Atomic Collisions*. Butterworths, London, England, UK, 1964.

[68] Control system studio. http://cs-studio.sourceforge.net/.

[69] G. Hernandez. *Fabry-Perot interferometers*. Cambridge University Press, New York, 1986.

[70] G.D. Boyd and D.A. Kleinman. Parametric interaction of focused gaussian light beams. *J. Appl. Phys.*, **39**:3597, 1968.

[71] M. Brieger, H.Büsener, A. Hese, F.v. Moers, and A. Renn. Enhancement of single frequency SGH in a passive ring resonator. *Opt. Comm.*, **38**:423, 1981.

[72] R.W.P. Drever, J.L. Hall, F.V. Kowalski, J. Hough, G.M. Ford, A.J. Munley, and H. Ward. Laser phase and frequency stabilization using and optical resonator. *Appl. Phys. B*, **31**:97, 1983.

[73] Carl L. Yaws, Prasad K. Narasimhan, and Chaitanya Gabbula. *Yaws' Handbook of Antoine Coefficients for Vapor Pressure (2nd Electronic Edition)*. Knovel, 2005.

[74] G. Pilcher and H.A. Skinner. *Thermochemistry of organometallic compounds*. John Wiley and Sons, Ltd. Chichester, UK, 1983.

[75] J.R. Fuhr and W.L. Wiese. A critical compilation of atomic transiion probabilities for neutral and singly ionized iron. *J. Phys. Ref. Data*, **35**:1669, 2006.

[76] A. Kramida, Yu. Ralchenko, J. Reader, and NIST ASD Team. *NIST Atomic Spectra Database (version 5.0)*. National Institute of Standards and Technology, Gaithersburg, MD., 2012. http://physics.nist.gov/asd, (retrieved April 1,2013).

[77] G.A. Martin, J.R. Fuhr, and W.L. Wiese. Atomic transition probabilities-scandium through manganese. *J. Phys. Chem. Ref. Data Suppl.*, **17**:512, 1988.

[78] S.J. Davis, J.J. Wright, and L.C. Balling. Hyperfine structure of the ground state of ^{55}Mn. *Phys. Rev. A*, **3**:1220, 1971.

[79] H. Walther. Das kernquadrupolmoment des ^{55}Mn. *Z. Phys.*, **170**:507, 1962.

[80] E. Handrich, A. Steudel, and H. Walther. The hyperfine splitting of the $3d^5 4s4p$ levels of Mn I and the quadrupole moment of ^{55}Mn. *Phys. Lett.*, **29A**:486, 1969.

[81] T. Brodzinski, H.D. Kronfeldt, J.R. Kropp, and R. Winkler. Hyperfinestructure-investigations in the manganese I configurations $3d^5 4s4p$ and $4s5s$. *Z. Phys. D: At. Mol. Clust.*, **7**:161, 1987.

[82] P.H. Lefèbvre, H.P. Garnir, and E. Biémont. Hyperfine structure for neutral manganese lines of astrophysical interest. *Astronomy and Astrophysics*, **404**:1153, 2003.

[83] R.J. Blackwell-Whitehead, J.C. Pickering, and O. Pearse. Hyperfine structure measurements of neutral manganese with fourier transform spectroscopy. *Astrophysical J. Sup. Ser.*, **157**:402, 2005.

[84] L.A. Torres-Gómez, G. Barriero-Rodríguez, and F. Méndez-Ruíz. Vapor pressures and enthalpies of sublimation of ferrocene, cobaltocene and nickelocene. *Thermochimica Acta*, **124**:179, 1988.

[85] M.A.V. Ribeiro da Silva and M.J.S. Monte. Vapour pressures and standard molar enthalpies of sublimation of two crystalline ironIII β-diketonates. the mean molar (Fe-O) bond-dissociation enthalpies. *J. Chem. Thermo.*, **28**:413, 1996.

[86] E.W. Berg and J.T. Truemper. Vapor pressure-temperture data for various metal β-diketone chelates. *Anal. Chim. Acta*, **32**:245, 1965.

[87] K. Pierloot, B.J. Persson, and B.O. Roos. Theoretical study of the chemical bonding in Ni(C_2H_4) and ferrocene. *J. Phys G: Nucl. Part. Phys.*, **21**:707, 1995.

[88] R.D. Bach, D.S. Shobe, H.B Schlegel, and C.J. Nagel. Thermochemistry of iron chlorides and their positive and negative ions. *J. Phys. Chem.*, **100**:8770, 1996.

[89] P. Sharpe and D.E. Richardson. Metal-ligand bond energies and solvation energies for gas-phase transition-metal tris(acetylacetonate) complexes and their negative ions. *J. Am. Chem. Soc.*, **113**:8339, 1991.

[90] W.J. Lyman. *Handbook of Chemical Property Estimation Methods*. McGraw-Hill Book Company, New York, 1982.

[91] E. Handrich, A. Steudel, R. Wallenstein, and H. Walther. Level crossing experiments in the Mn I spectrum. *Proc. Int. Conf. Physics of the one and two electron atoms*, page 380, 1968.

[92] D. Rapp and W. E. Francis. Charge exchange between gaseous ions and atoms. *J. Chem. Phys.*, 37:2631, 1962.

[93] D. P. Dewangan. Dependence of symmetrical charge transfer cross section of ionization potential. *J. Phys. B: At. Mol. Phys.*, 6:L20, 1973.

[94] M.T. Vieyra-Eusebio and A. Rojas. Vapor pressures and sublimation enthalpies of nickelocene and cobaltocene measured by thermogravimetry. *J. Chem. & Eng. Data*, **56**:5008, 2011.

[95] D.J. Morrissey. Extraction of thermalized projectile fragments from gas. *Eur. Phys. J. Special Topics*, **150**:365, 2007.

[96] B. Cheal, K. Baczynska, J. Billows, P. Campbell, F.C. Charlwood, R. Eronen, D.H. Forest, A. Jokinen, T. Kessler, I.D. Moore, M. Reponen, S. Rothe, M. Rüffer, A. Saastamoinen, G. Tungate, and J. Äystö. Laser spectroscopy of niobium fission fragments: first use of optical pumping in an ion beam cooler buncher. *Phys. Rev. Lett.*, **102**:222501, 2009.

[97] W. Geithner, U. Georg, S. Kappertz, M. Keim, A. Klein, P. Lievens, R. Neugart, M. Neuroth, L. Vermeeren, S. Wilbert, and the ISOLDE Collaboration. Measurement of nuclear moments and radii by collinear laser spectroscopy and by $\beta-$NMR spectroscopy. *Hyperfine Int.*, **129**:271, 2000.

[98] P.F. Mantica, R.W. Ibbotson, D.W. Anthony, M. Fauerbach, D.J. Morrissey, C.F. Powell, J. Rikovska, M. Steiner, N.J. Stone, and W.B. Walters. Sign dependence of spin polarization for seconday fragments produced following intermediate-energy projectile fragmentation. *Phys. Rev. C*, **55**:2501, 1997.

[99] K. Minamisono, R.R. Weerasiri, H.L. Crawford, P.F. Mantica, K. Matsuta, T. Minamisono, J.S. Pinter, and J.B. Stoker. Fast-switching NMR system for measurements of ground-state quadrupole moments of short-lived nuclei. *Nucl. Instru. Methods A*, **589**:185, 208.